Department of Chemistry
Physical Chemistry

Upconversion luminescence in Er-codoped $NaYF_4$ nanoparticles
—
Fundamental photophysics and optimization for life science applications

Doctoral thesis (cumulative)

in fulfillment of the requirements for the degree

"doctor rerum naturalium"
(Dr. rer. nat.)

in the scientific discipline "Physical Chemistry"

submitted to the
Faculty of Science
of the University of Potsdam

by
Dennis Tobias Klier

Potsdam, June 2016

Published online at the
Institutional Repository of the University of Potsdam:
URN urn:nbn:de:kobv:517-opus4-98486
http://nbn-resolving.de/urn:nbn:de:kobv:517-opus4-98486

Contents

Zusammenfassung der Arbeit mit dem Titel:

Upconversion luminescence in Er-codoped $NaYF_4$ nanoparticles – Fundamental photophysics and optimization for life science applications

eingereicht von Dennis Tobias Klier, Juni 2016
an der Universität Potsdam

Ziel der Arbeit war es ein erweitertes Verständnis des Mechanismus der Lichtaufkonversion, sowie dessen gezielte Manipulation in verschiedenen Nanomaterialien auf Natriumyttriumfluoridbasis zu erlangen. Die optischen Eigenschaften werden dabei durch eine gezielte Zusammenstellung verschiedener Lanthanoidionen hervorgerufen, welche während der Synthese in die Materialien eingebracht werden. Der Fokus lag hierbei in der Aufklärung des Zusammenspiels zwischen der Struktur der Materialien und deren Lichtaufkonversionsvermögen sowie dem Erlangen eines generellen Verständnisses der einzelnen Teilschritte des Lichtaufkonversionsmechanismus. Dabei wird das Licht, welches nach Anregung der Lanthanoidionen durch einen Laser von diesen emittiert wird, hinsichtlich der Farbzusammensetzung und des Abklingverhaltens der Lumineszenz untersucht. Diese Erkenntnisse geben sowohl einen Einblick in die verschiedenen Teilschritte des Lichtaufkonversionsmechanismus, als auch deren Korrelation zur Struktur der Nanomaterialien. Während der Arbeit wurde ein variabler Messplatz mit einer wellenlängendurchstimmbaren Anregungslichtquelle, einer Detektionseinheit mit hervorragender spektraler und zeitlicher Auflösung für die Messung des emittierten Lichtes sowie einer Temperiereinheit, mit der die Proben in einem Temperaturbereich von 4 Kelvin (-269,15 °C) bis 328 Kelvin (50 °C) temperiert werden können, aufgebaut.
Die Proben wurden mithilfe der modernen Kopräzipitations- und Hydrothermalsynthese in verschiedenen Zusammensetzungen und Oberflächenmodifizierungen hergestellt, um sowohl Partikel für fundamentale Untersuchungen der Lichtaufkonversion verfügbar zu haben, als auch den hohen Anforderungen für Anwendungen in den Lebenswissenschaften gerecht zu werden. Die Reaktion fand bei hohen Temperaturen (160 °C – 320 °C) unter Schutzgasatmosphäre statt und gewährleistete so die Bildung von hochkristallinen Partikeln, deren Größe stark mit der Synthesetemperatur korreliert. Mithilfe von zeitaufgelösten Lumineszenzuntersuchungen gelang ein sehr detaillierter Einblick in strukturelle Veränderungen der Nanopartikeln, welche durch klassische strukturanalytische Methoden, wie der Röntgenpulverdiffraktometrie, nicht in dem Maße möglich sind. Zudem konnte ein erheblicher Teil dazu beigetragen werden, das komplexe Zusammenspiel von Energietransportmechanismen, Gitterschwingungen und thermisch induzierten Prozessen zu verstehen.
Zuletzt wurden, basierend auf der Vielzahl an gewonnenen Erkenntnissen, speziell

designte Nanopartikel hergestellt. Die Farbe des Emissionslichts dieser Parikel wies dabei eine hohe Abhängigkeit von der Umgebungstemperatur auf. Auftretende Herausforderungen induziert durch das verwendete Anregungslicht im Nahinfrarotenbereich, wie das Aufheizen oder die zu hohe Absorption der Probe, wurden durch die Erweiterung des Aufkonversionssystems gelöst. Damit konnten beste Voraussetzungen für potentielle Anwendungen, wie zum Beispiel als Nanothermometer geschaffen werden.[1]

Abstract of the work titled:

Upconversion luminescence in Er-codoped $NaYF_4$ nanoparticles – Fundamental photophysics and optimization for life science applications

submitted by Dennis Tobias Klier, June 2016
at University of Potsdam

In the context of an increasing population of aging people and a shift of medical paradigm towards an individualized medicine in health care, nanostructured lanthanides doped sodium yttrium fluoride ($NaYF_4$) represents an exciting class of upconversion nanomaterials (UCNM) which are suitable to bring forward developments in biomedicine and -biodetection. Despite the fact that among various fluoride based upconversion (UC) phosphors lanthanide doped $NaYF_4$ is one of the most studied upconversion nanomaterial, many open questions are still remaining concerning the interplay of the population routes of sensitizer and activator electronic states involved in different luminescence upconversion photophysics as well as the role of phonon coupling. The collective work aims to explore a detailed understanding of the upconversion mechanism in nanoscaled $NaYF_4$ based materials co-doped with several lanthanides, e.g. Yb^{3+} and Er^{3+} as the "standard" type upconversion nanoparticles (UCNP) up to advanced UCNP with Gd^{3+} and Nd^{3+}. Especially the impact of the crystal lattice structure as well as the resulting lattice phonons on the upconversion luminescence was investigated in detail based on different mixtures of cubic and hexagonal $NaYF_4$ nanoscaled crystals.

Three synthesis methods, depending on the attempt of the respective central spectroscopic questions, could be accomplished in the following work. $NaYF_4$ based upconversion nanoparticles doped with several combination of lanthanides (Yb^{3+}, Er^{3+}, Gd^{3+} and Nd^{3+}) were synthesized successfully using a hydrothermal synthesis method under mild conditions as well as a co-precipitation and a high temperature co-precipitation technique.

Structural information were gathered by means of X-ray diffraction (XRD), electron microscopy (TEM), dynamic light scattering (DLS), Raman spectroscopy and inductively coupled plasma atomic emission spectrometry (ICP-OES). The results were discussed in detail with relation to the spectroscopic results. A variable spectroscopic setup was developed for multiparameter upconversion luminescence studies at various temperature 4 K to 328 K. Especially, the study of the thermal behavior of upconversion luminescence as well as time resolved area normalized emission spectra were a prerequisite for the detailed understanding of intramolecular deactivation processes, structural changes upon annealing or Gd^{3+} concentration, and the role of phonon coupling for the upconversion efficiency. Subsequently it became possible to synthesize UCNP with tailored upconversion luminescence properties.

In the end, the potential of UCNP for life science application should be enunciated in

context of current needs and improvements of a nanomaterial based optical sensors, whereas the "standard" UCNP design was attuned according to the special conditions in the biological matrix. In terms of a better biocompatibility due to a lower impact on biological tissue and higher penetrability for the excitation light. The first step into this direction was to use Nd^{3+} ions as a new sensitizer in tridoped $NaYF_4$ based UCNP, whereas the achieved absolute and relative temperature sensitivity is comparable to other types of local temperature sensors in the literature.[1]

List of publications

Original publications:

1. D. Bader, D.T. Klier, C. Hettrich, F.F. Bier and P. Wessig "Detecting carbohydrate–lectin interactions using a fluorescent probe based on DBD dyes" *Anal. Methods*, **2016**, *8*, 1235-1238.

2. D.T. Klier and M.U. Kumke "Analysing the effect of the crystal structure on upconversion luminescence in Yb^{3+}, Er^{3+} -co-doped $NaYF_4$ nanomaterials" *J. Mater. Chem. C*, **2015**, *3*, 11228-11238.

3. D.T. Klier and M.U. Kumke "Upconversion $NaYF_4$:Yb:Er nanoparticles co-doped with $Gd^{3+}$and Nd^{3+} for thermometry on the nanoscale" *RSC Adv.*, **2015**, *5*, 67149-67156.

4. D.T. Klier and M.U. Kumke "Upconversion luminescence properties of $NaYF_4$:Yb:Er nanoparticles codoped with Gd^{3+}" *J. Phys. Chem. C*, **2015**, *119*, 3363-3373.

5. U. Eisold, A. Kupstat, D.T. Klier, P.-A. Primus, M. Pschenitza, R. Niessner, D. Knopp, M.U. Kumke "Probing the physicochemical interactions of 3-hydroxybenzo[a]pyrene with different monoclonal and recombinant antibodies by use of fluorescence line-narrowing spectroscopy" *Anal. Bioanal. Chem.*, **2014**, *14*, 3387-3394.

Oral presentations:

1. D.T. Klier, S. Nacak, S. McGee, A. Lopez and M.U. Kumke "Upconversion nanoparticles (UCNP) as versatile probe in life science application" Workshop in field of action: *Biomaterials and photonics*, Potsdam, Germany, **2016**.

2. D.T. Klier, S. Nacak, S. McGee and M.U. Kumke; "Potential of Upconversion nanoparticles (UCNP) in life-science/bioanalytics" Workshop in field of action: *Biomedical optics and ophthalmic optics*, Potsdam, Germany, **2015**.

3. D.T. Klier, S. McGee, A. Menski and M.U. Kumke "Combining TRANES and XRD for in-depth analysis of crystal phase transformation in NaSc/YF_4-based UCNP for applications in thermometry on the nanoscale" *9. International conference on f-elements (ICFE)*, Oxford, Great Britain, **2015**.

4. D.T. Klier, S. Nacak and M.U. Kumke "Upconversion NaSc/YF_4:Yb:Er nanoparticles co-doped with $Gd^{3+}$and Nd^{3+} for thermometry on nanoscale" *Optics in the Life Sciences Congress*, Vancouver, Kanada, **2015**.

5. D.T. Klier, S.-H. Kung, E. Rühl and M.U. Kumke "Ultra-low temperature studies on the upconversion luminescence of co-doped $NaYF_4$-based nanoparticles" *113. Bunsentagung*, Hamburg, Germany, **2014**.

6. D.T. Klier, S.-H. Kung, E. Rühl and M.U. Kumke "Upconversion anti-stokes nanocrystals for life-science application – synthesis, characterization and application" *16. JCF Frühjahrssymposium*, Jena, Germany, **2014**.

Poster presentations:

1. D.T. Klier, S. McGee, A. Menski and M.U. Kumke "Combining TRANES and XRD for in-depth analysis of crystal phase transformation in NaSc/YF_4-based UCNP for applications in thermometry on the nanoscale" *9. International conference on f-elements (ICFE)*, Oxford, Great Britain, **2015**.

2. D.T. Klier, D. Steinbrück, S. Krusekopf, R. Niestroj-Pahl, S. Saß, M. Zoli, K. Lücke and H.-G. Löhmannsröben "Fiber Optical Cell Collector and Sensor (FOCCS)" *29. Treffpunkt Medizintechnik*, Berlin, Germany, **2015**.

3. D.T. Klier, S. Nacak, M.U. Kumke "Upconversion NaSc/YF_4 :Yb:Er nanoparticles co-doped with Gd^{3+} and Nd^{3+} for thermometry on nanoscales" *29. Tag der Chemie*, Berlin, Germany, **2015**.

4. D.T. Klier, S. Nacak, M.U. Kumke "Upconversion NaSc/YF_4 :Yb:Er nanoparticles co-doped with Gd^{3+} and Nd^{3+} for thermometry on nanoscales" *Anakon*, Graz, Austria, **2015**.

5. D.T. Klier, Pablo Wessig, Robert Wawrzinek, Denise Bader, Monique Mertens, Franz-Joseph Meyer-Almes, Christian Meyners, Andreas Krämer, Steffen Hinz "Applications of DBD dyes" *24. Lecture Conference on Photochemistry*, Köln, Germany, **2014**.

6. D.T. Klier, S.-H. Kung, E. Rühl, M.U. Kumke "Low-temperature luminescence study of novel $NaYF_4$-based upconversion nanoparticles (UCNP) co-doped with (Gd:Yb:Er)" *112. Bunsentagung*, Karlsruhe, Germany, **2013**.

7. D.T. Klier, S.-H. Kung, E. Rühl, M.U. Kumke "Low-temperature luminescence and Raman study of novel $NaYF_4$-based upconversion nanoparticles (UCNP) co-doped with (Gd:Yb:Er)" *25. Terrae Rarae*, Stuttgart, Germany, **2013**.

8. D.T. Klier, U. Eisold and M.U. Kumke "Fluorescence Line-Narrowing spectroscopy for investigation purposes in life-science: Interactions between 3-Hydroxybenzo[a]pyrene and monoclonal Antibodies" *23. Lecture conference on Photochemistry*, Potsdam, Germany, **2012**.

1 Introduction

1.1 Energy Upconversion Materials in Context

In the context of a fast increasing human population several new environmental, social and economic threats coming up and forcing us to explore new paths in central fields of activity like energy supply or health care. The renunciation energy systems based on fossil fuels and nuclear energy as well as the change towards individualized medicine are only two of the future challenges which have to be solved.[2,3] A new and exciting class of materials which are suitable of pushing forward developments in these related issues are energy upconversion materials (UCM), which have attracted extensive attention in the past several years. The special kind of energy conversion denotes as upconversion (UC) is a non-linear *anti-Stokes* process that converts at least two low-energy near-infrared (NIR) photons into one higher energy photon (*e.g.* ultra violet, visible or NIR spectral range) using lanthanide ions (Ln^{3+}) embedded in a suitable inorganic host matrix.[4] The unique electronic structure in form of real ladder like energy levels and their long luminescence decay times of up to several milliseconds make lanthanide ions a perfect choice for very efficient upconversion processes and moved lanthanide based UC nanomaterials in the forefront of material science.[5–7]
Nowadays UCM has been widely used in a vast number of applications, such as photovoltaic devices (solar cells) in form of macroscopic crystals to increase the relative low efficiency of the solar cell devices.[8,9] The dominant losses of a single band gap based solar cells are caused by incomplete usage of the solar spectrum.[10] Whereas 35 % of the incident solar energy is lost due to thermalization losses caused by photons carrying a higher energy than the band gap.[11] Further 20 % are lost by transmission losses of the semiconductor devices due to photons carrying less energy than the band gap. Whereas the heat of the thermalization losses is used in solar thermal systems, UCM are used to convert the transmitted photons into higher energy photons which can be used by the photovoltaic devices.[2] First developments in these fields show already today promising results, whereas the efficiency of the solar cell devices could be increased by nearly 25 % without any known drawbacks, which is a big step towards an extensive use of renewable energy sources.[12,13]
Due to the enormous development in nanotechnology also a completely new field of application for UCM was discovered, where UCM could be established in central issues of biological and biomedical applications. Driven by the focus in biomedicine and biodetection towards a customized personal medical care and the increasing number of targeted efforts on anticancer and other therapeutics to diseased sites with minimal collateral damage to normal tissues as well as the development of medicals tools that combines therapy and diagnostic (Theranostic), UC nanomaterials have gained im-

portance in diverse areas of life science.[3,14] The high potential for biomedical research as new class of optical probe is based on their unique optical features like long luminescence decay times, sharp emission band width, excitation in the NIR range, nearly vanished background auto-fluorescence or large *anti-Stokes* shift combined with a high photochemical stability and low toxicity.[6] Even though initial successes in multimodal imaging in vivo/ in vitro,[15–20] photodynamic therapy (PDT),[21–24] drug delivery,[5,25,26] photothermal therapy (PTT)[24,26] or disease theranostics are done, the potential is not yet exhausted[4,6,24,27,28]

A Brief Historical Review

The whole field of UCM can be tracked back to a short proposal of Bloembergen in 1959 about a solid state infrared quantum counter.[29] Bloembergen had the idea to conceive a detector for infrared photons based on a sequential absorption (ESA) within inorganic crystals, whereas rare earth ions or other transition group ions are embedded in a host lattice. The experimental evidence of Bloembergen's great idea was impossible with the technical possibilities at that time, as no chance was given to pump one single ion in sequence of two photons in its intrinsic decay time.[30] With the development of laser systems, which offers a high power density and fiber local confinement some of the first experiments have been succeeded by Esterowitz, Chicklis and Brown in the late 1960s.[31–33] Based on their results it could be demonstrated that energy diffusion in these kind of materials is based on energy transfer between identical ions. The further development to UCM using different lanthanides in one host was discovered by Auzel, Ovsyankin, Feofilov and Esterowitz *et al.*[33–35] As first sensitizers Yb^{3+} ions were used in combination with Er^{3+}, Tm^{3+} and Ho^{3+} as activator ions, which is still today the standard ingredients in UC technology. Furthermore the sequential energy transfer (ETU) between two rare earth ions suggested from Auzel was proven as one of the most efficient UC mechanisms and was a milestone in UC technology.[34] From that moment onwards it has been recognized that a number of different mechanisms are involved in upconversion either alone or in combination. Since laser sources for NIR/IR became commonly available, UC processes have been observed in several kinds of rare earth doped materials such as crystals, bulk glasses, fibers or waveguides. Furthermore, two additional UC mechanisms named cooperative sensitization and photon avalanche process have been widely investigated. Based on a lot of extensive investigations on UC processes in glasses and several inorganic crystals a deep understanding of the complex interplay between different upconversion mechanisms was generated, whereas Auzel and Suyver *et. al.* had an important contribution on this mechanistic development.[30,36–38] Whereas the fundamental UC mechanisms were revealed as far as possible, the synthesis of monodisperse UC nanocrystals was still a technologically insurmountable obstacle to be overcome. Based on the work of Park and Wang, large scale monodisperse nanoparticle synthesis[39,40] of oleate precursors became the most used standard procedure for uniform sized UC nanoparticles for fluoride host lattice.[41–43] Another synthesis approach developed in the same period of time consists of core-shell type nanoparticles which deliver a much higher upcon-

version efficiency. The high potential of non radiative deactivation processes at the surface will be fully exploited due to the high surface to volume ratio in nanoparticles, whereas a upconversion efficiency enhancement about a factor of 240 is possible.[42,44,45] In subsequent work the core shell design was further refined by a successive layer by layer strategy for multiple shell nanoparticles.[46–48] These works can be considered as the beginning of the extensive investigation of UC for a broad field of application in recent years.

1.2 Composition and Design of Upconversion Nanoparticles

The versatility of UCM is based on the large possible variety of lanthanides that entails a large and easily accessible spectral range from the ultra-violet (UV) up to the NIR as well as magnetic properties of, *e.g.* gadolinium.[49–51] The lanthanides fulfill only the sufficient condition for a versatile candidate, whereas the center piece for a maximum upconversion quantum efficiency is the host lattice in which the lanthanides are embedded.[41,52–57] The host lattice can be characterized by lattice symmetry, homogeneity, surface morphology and the type of the exposed surface facets and edges defined by the Miller indices. An ideal host lattice should exhibit the following properties: a) high tolerance of luminescence centers (dopants), b) high transparency for free migration of NIR photons in the lattice, c) low phonon energy to minimize detrimental non-radiative relaxation processes and d) high chemical and thermal stability to avoid variations in the crystal structure.[7] The host lattice in most UCM encompasses a variety of trivalent yttrium or scandium inorganic compounds in form of oxides, oxysulfides, oxysaltes and fluorides. Alkali earth ion and transition metal ion based compounds on the other hand have been investigated as host lattices.[58–61] For UC nanomaterials $NaRF_4$ (R = Sc, Y or Ln) has been proven to be one of the most efficient host lattice due to their relative low phonon energy, whereas from the two existing phase structures the hexagonal β-phase is much more efficient than the cubic α-phase. For bulk materials, on the other hand, fluoride and oxide based glasses are most frequently used to achieve high efficient upconversion substrates.
Apart from the fundamental demands including different lanthanides and host lattices further relevant parameters (see Scheme 1) also play an important role for the upconversion efficiency, whereas the contribution strongly depends on the type of UC material. The expected effects and correlations of single parameters on the upconversion processes in bulk and nanomaterials differ a lot, whereas nanomaterials are the most complex case.[62] Especially for UC nanomaterials there is a remarkable interest to clearly understand the complex interplay of all kinds of these parameters in order to provide a toolbox complying with requirements for several application in life science. Accordingly to this, other properties apart from the overarching objective of a maximum quantum efficiency become more important such as for example a well defined controlled upconversion luminescence emission, selective addressing of different lanthanides controlled by various excitation mechanism, getting access to certain

system parameters like temperature or to minimize non-radiative deactivation due to the surrounding media. A detailed mechanistically comprehension is necessary especially in multiparameter detection applications to avoid misdiagnosis and to increase the performance of the given method.

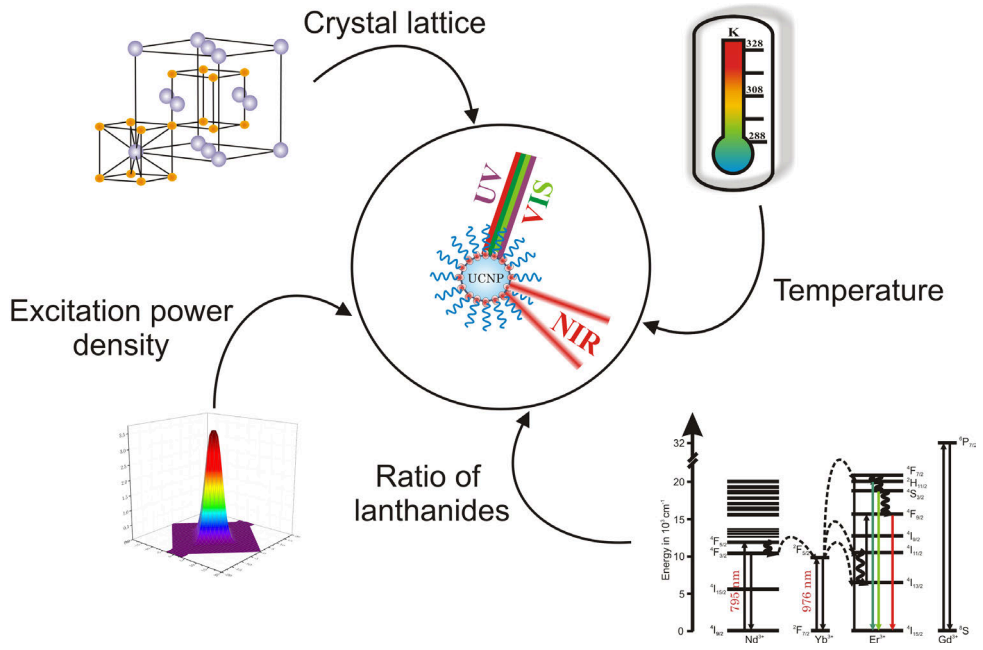

Scheme 1: Overview of the typical parameter for the manipulation of upconversion luminescence of lanthanide based upconversion material.

The optical properties can change dramatically with the synthesis strategy of the upconversion material. A lot of work has been dedicated to develop synthesis strategies for monodisperse highly crystalline $NaRF_4$ (R = Sc, Y or Ln) nanoparticles with a variety of surface surfactants, embedded lanthanides and passivisation shells. However, when comparing the two polymorphic structures of $NaRF_4$ (R = Y) particles synthesized using different routines, it becomes evident that the milder the synthesis conditions, the higher the possibility to produce the thermodynamically less stable α-phase nanoparticles.[63] The synthesis temperature T could therefore be used to control the crystal phase type structure in order to investigate possible influences of the different crystal structures on the optical properties of the nanomaterial. Based on a targeted selection of a suitable synthesis route or synthesis condition it is therefore possible to adjust several particle parameters in order to systematically investigate the influence of crystal phase type on the upconversion luminescence properties.

1.2.1 Insight View into the Crystal Structure of $NaYF_4$ Nanocrystals

Until now $NaYF_4$:Re (Re = rare earth, typically Re = Yb or Nd as sensitizers or Re = Er as activator) based materials belong to the most efficient host lattices for UCNP. The $NaYF_4$ based materials are known to exist in either isotropic cubic (α-phase) or anisotropic hexagonal (β-phase) crystal lattice, which offer a much higher upconversion efficiency relative to its cubic phase counterpart. To gain a deep insight into the highly complex photophysical properties of these UCMs, the structure has to be known in the same precise manner.
The cubic phase has a fluorite (CaF_2) type structure with the space group $Fm\bar{3}m$ (JCPDS No. 77-2042).[54,64] The Ca^{2+} site (4a) is randomly occupied by 1/2 Na^+ and 1/2 Y^{3+}; the nearest neighboring ions around Y^{3+} on site 4a are 8 F^- and the second nearest neighboring ions are 6 Na^+ and 6 Y^{3+}, see Figure 1.1.[54,65]

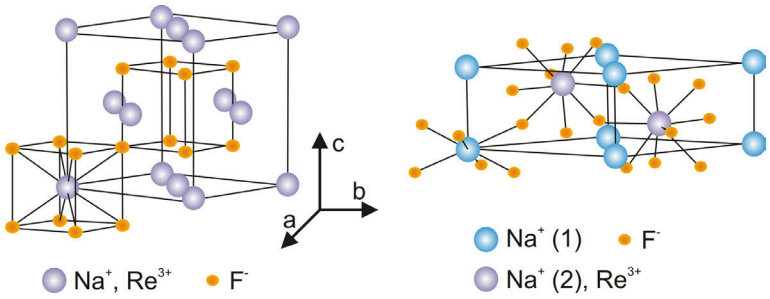

Figure 1.1: Schematic presentation of cubic- and hexagonal-phase of $NaYF_4$, respectively. In the cubic phase, equal numbers of F^- cubes contain cations and vacancies. In the hexagonal phase, an ordered array of F^- ions offers two types of cation sites: one occupied by Na^+ and the other randomly occupied by Na^+ and Re^{3+}.[54]

Depending on the synthesis conditions also a high-temperature α-phase modification exists. Both α-phase modifications are built of (Na/Y:Re)$F1_8$ cubes with a certain cation site symmetry C_{3v} or O_h for the high-temperature modification, due to a decreased Na/Y:RE ratio during the heating, where NaF could be evaporated. The result of the even higher Y:Re^{3+} dominance over Na^+ is a displacement of the cations in the lattice.[66]
In contrast a controversy has arisen about which space group best describes the β-phase either $P\bar{6}$[67,68] or $P6_3/m$,[54,66,69] which cannot be easily distinguished due to the small differences in the pattern of XRD investigations.[53,70] In $P\bar{6}$ there are three cation sites, whereas one site is statistically occupied by Na^+ and Y:Re^{3+} with 50 % occupation. The two other sites are ordered with Y:Re^{3+} for the one site, Na^+ for the other site and two F sites. In contrast $P6_3/m$ has only one F site and two types of relatively low-symmetry cation sites. One cation site is nine-fold coordinated occupying randomly Na^+ and Y:Re^{3+} (site 2c, symmetry of C_{3h}, which is coordinated by nine neighboring F^- ions in the shape of a tricapped trigonal prism and 2 Na^+ and

6 Y:Re^{3+} in the second nearest neighboring shell). Another six-fold coordinated site is occupied by Na^+ and vacancies (site 2b). The structure change from α- to β-phase result of a significant electron cloud distortion of the cations. Recently research studies using site selective luminescence excitation spectra and polarized absorption spectra are concluding that β-$NaYF_4$ could be described only by space group $P6_3/m$.[54,66,69] The crystal phase transformation from cubic to hexagonal phase is accompanied by a more dense packed unit cell (83 $Å^3$ to 72 $Å^3$) and shorter Re-Re distances. Furthermore the $NaYF_4$: Re composition is close to stoichiometric, whereas the two α-phases are enriched with Re and thus additional fluoride ions are needed to balance the charges. All in all, less lattice defects or fault locations are expected in the hexagonal lattice.[66]

1.2.2 Tuning Energy Levels and Transition Probabilities: Crystal Lattice Modification as a Tool for Upconversion Enhancement

Photon upconversion is shown by optical centers (Re^{3+} ions) with a series of metastable excited states that enable several steps of excitation into an upper excited state. For a subsequently electron transition from the upper excited states to a lower lying energy level, a photon with shorter wavelength is emitted. In order to achieve an efficient multi-photon upconversion an energy scheme with equally spaced intermediate states is required. In UCNP using Re ions the energy levels of the $4f^N$ ($N = 1$ to 13) states are defined by Russell-Saunders notation of $^{2S+1}L_J$ multiplets, with S, L and J being the total spin, orbital and angular momenta of the N 4f electrons. The electrostatic interaction leads to ^{2S+1}L splitting on the order of 10^4 cm^{-1}.[71,72] The spin-orbit interaction splits the levels further into $^{2S+1}L_J$ leading to a separation of the J states by 10^3 cm^{-1}.[71] Furthermore, the crystal field repeals the degeneracy complete or partly in J states leading to a separation in the order of 10^2 cm^{-1}.[71] The energy matching of a certain Re ion pair can be improved for a more efficient upconversion luminescence due to the choice of host lattice and/or alkali ion/lanthanide ion doping. The energy levels are thereby affected by the crystal field interaction, symmetry dependence and/or vibronic sidebands.[73]

Crystal-Field Splitting

In an ionic crystal the optically active dopand ions perceive the influence of the electrons of the host lattice as a repulsion and for the nuclei of the host lattice as an attraction. The accumulation of these influence can be considered as a net electric field, known as the crystalline field. The crystalline field is fully external to the optically active dopand ions, whereas the symmetry is determined by the chemical composition of the host lattice. Based on the Judd-Ofelt theory the spectra emitted of the individual lanthanide ions are determined by their nanoscopic environment electronically and structurally or more precise the crystal field strength and symmetry (electrical field of the host lattice ions) the different lanthanide ions are exposed to.[71,73–75] One of the resulting effects is the splitting of the degenerated energy lev-

els, the so called Stark-splitting, due to J-mixing. Furthermore, spin-orbital coupling mixes the Russel-Saunders multiplet of the same J. The mixing of L-S and J is more significant for upper lying excited energy levels than for lower in energy levels, due to the higher density of energy levels. Depending on the site symmetry and the crystal field strength of the host material, energies of the $4f^N$ levels can shift up to 10 %.[73] The degree of the sublevel spreading is induced by the Stark-splitting and is proportional to an increasing strength of the crystal field. For an efficient upconversion process not the maximum shift of the energy levels induced by the crystal-field splitting with respect to the overall $4f^N$ configuration is aimed. But rather by the reduction of the energy mismatches of energy levels relative to each other has a significant effect on the inter-and intra-lanthanide energy transfer dynamics.

Symmetry Dependency

In case of a free atom, a spherical symmetry can be assumed and each energy level is spread into $2J+1$ degeneracy. The spherical symmetry is disrupted when the ion is placed into a crystal environment and each level splits due to the strength of the crystal field as mentioned above. In fact the spherical symmetry is reduced to the point symmetry at the ion site. As a result, the extent to which the $2J+1$ degeneracy is removed, will depend on the point symmetry surrounding of the ion.[71,73–75] However, 32 crystallographic point groups are known, which can be divided into four general symmetry classes.

1. Cubic: O_h, O, T_d, T_h, T
2. Hexagonal: D_{6h}, D_6, C_{6v}, C_{6h}, C_6, D_{3h}, C_{3h}, D_{3d}, D_3, C_{3v}, S_6, C_3
3. Tetragonal: D_{4h}, D_4, C_{4h}, C_{4v}, C_4, D_{2d}, S_4
4. Lower symmetry: D_{2h}, D_2, C_{2v}, C_{2h}, C_2, C_s, S_2, C_1

By the knowledge of the symmetry class at the ionic site, the number of energetically different levels a given J state splits into can deduced. Otherwise the Re ions can be used to predict the crystal symmetry if the number of levels of the ion can be determined.[71] Certainly, a difference in the crystal field symmetry leads to different energy level splitting of the ${}^{2S+1}L_J$ multiplet. Whereas, the inter-lanthanide transition probability, depending on the energy mismatch, is more influenced by the crystal field symmetry than the splitting of the multiplet. It is generally known that transitions between levels inside the 4f electronic shell are forbidden by the Laporte selection rule. The basic statement of the Laporte selection rule is that states with even parity can be connected by electric dipole transitions only with states of odd parity and odd states only with even ones. The original parity forbidden intra $4f^N$-$4f^N$ electronic transitions can be loosened by crystal field induced coupling with unoccupied electronic configurations of the Re ion in higher energies such as $4f^{N-1}5d$ or for magnetic dipole or electric quadrupole transitions within the 4f shell.[73,75] Therefore, if the initial state and the final state have the same parity, then k^1 must be even. If these states have an

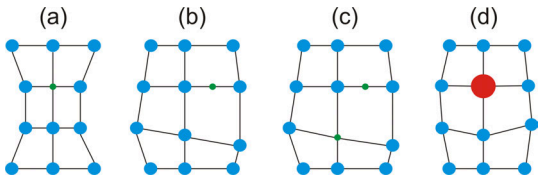

Scheme 2: (a) Small atom substitution, (b) interstitial occupation by small atom, (c) combination of substitution and interstitial occupation and (d) big atom substitution.

opposite parity k[1] must be odd. For 4f electrons k must be even in case of transitions within the f^Nconfiguration, whereas for transition in higher energies such as $4f^{N-1}5d$ k is odd. The odd-order terms play a key role in the Judd-Ofelt theory for forced electric dipole transition of Re ions in solids, that mitigates the Laporte selection rule.[71] In comparison to that of the f^N states, $4f^{N-1}5d$ energy levels strongly depend on the host lattice, because of the values of k are limited by the point symmetry of the ion. The odd terms exist mainly in crystals of three-fold rotational axes with a removed inversion symmetry. Correspondingly, Re ions are located on a hexagonal, trigonal or lower symmetry site. At a low site symmetry the transition probability is increased, due to an increase of the overall crystal field strength and a reduction of the degeneracy of the free ion state.[71,73,75]

Doping of Re ions into a crystal lattice leads to a lattice distortion, thus may breakdown the intrinsic site symmetry in a certain manner. For low doping concentration and similar ionic radii of dopand ion and lattice ions, the original crystallographic site symmetries are locally distorted, whereas the crystalline structure of the doped crystal is not influenced significantly.[73] The effect was used selectively to control the spectroscopic properties (e.g. peak ratio) of UCNP or to predict the optimal structure/host lattice for more efficient UCNP, whereas doping with alkali or Re ions with slightly higher or lower ionic radii than Na^+ ions makes a replacement of Na^+ ions with these ions possible.[69,73] On one hand the purpose of doping is to slightly change the size of the unit cell in the crystal (see Scheme 2) and changing the Yb-Er distance and on the other hand to achieve a crystal phase transformation at high doping concentration e.g. using Gd^{3+} ions.[54,55]

[1]For an ion in a crystal the perturbed free ion Hamiltonian can be written as,

$$H = H_F + V_{CF}$$

, where H_F is the free Hamiltonian and V_{CF}, the perturbation Hamiltonian, is due to the potential in a spherical harmonic series, provided by the crystal environment around the ion.

$$V_F = \sum_{kq} A_{kq} \sum_i r_{ik} V_{kq}(\theta_i, \varphi_i),$$

where r_i is the radial coordinate of the ith electron. $V_{kq}(\theta_i, \varphi_i)$ is the qth component of the spherical harmonic of the order k, and θ_i, φ_i are the angular coordinates of the ith electron. A_{kq} are parameters which depend on the specific crystal-symmetry group.[71,73,74]

Vibronic Side Bands

Ion-phonon interactions play a central role in upconversion mechanisms in rare earth based UCM. One result of ion-phonon interactions is the broadening of the line width of electronic states. In case of Re ions in crystals with weak ion-phonon interactions the homogeneous line broadening is imposed by temperature dependent coupling, whereas inhomogeneous broadening is induced by lattice defects and strains that shift inconsistently the position of electronic energy levels.[73] Along with weak ion-phonon interactions, the vibronic side bands or phonon side bands are usually much weaker than the zero phonon lines, which is particularly applicable for intra $4f^N$ electronic transitions.
For 4f-5d transitions in most upconversion phosphors, strong vibronic side bands appear along with the zero phonon lines due to selective vibronic coupling to electronic transitions. The vibronic coupling to electronic transitions is much stronger for higher excited states ($4f^N$), resulting from an increase of configuration interactions. The characteristics of vibronic transitions of ions in crystals based on the Franck-Condon principle and Huang-Rhys model of vibronic interactions are well understood. Also complex systems with vibronic coupling that involve multiple electronic energy levels and multiple vibrational modes are accessible. The spectral profile of vibronic sidebands in absorption spectra with frequency mixing and multi-phonon progression can be calculated applying these models. It could be demonstrated that phonon side bands can stretch above 1000 cm^{-1} or that more than 30 vibronic side bands spread over 400 cm^{-1} with intensities comparable to zero phonon lines or stronger are possible.[76,77]
Especially in nanocrystals the vibrational frequencies in the surface layer can differ from that near the core, depending on the overall size of the nanoparticles. The vibronic coupling strength to electronic transitions is also expected to be affected, which leads to more complex upconversion processes.
In the context of UCNP, the vibronic transitions have a significant influence on the upconversion efficiency. The efficiency can be raised by an increasing absorption cross section and an expansion of the band width. The latter is necessary to overcome the potential energy mismatches of the corresponding energy levels. Nevertheless, non-radiative relaxations could also be supported as undesirable side effects of the vibronic coupling, leading to a decrease of the intrinsic decay time of the excited states.[30,73]

Excitation Energy Migration

Another important parameter for an in depth discussion of upconversion processes is the energy preservation within the lattice domains and how the energy loss due to lattice defects, self quenching or cross relaxation processes could be minimized. Therefore it is worth to take a closer look into the possible energy migration pathways. In the context of UCNP a detailed knowing of the energy migration is necessary for implementations – like core-shell – to separate regions where excitation and emission

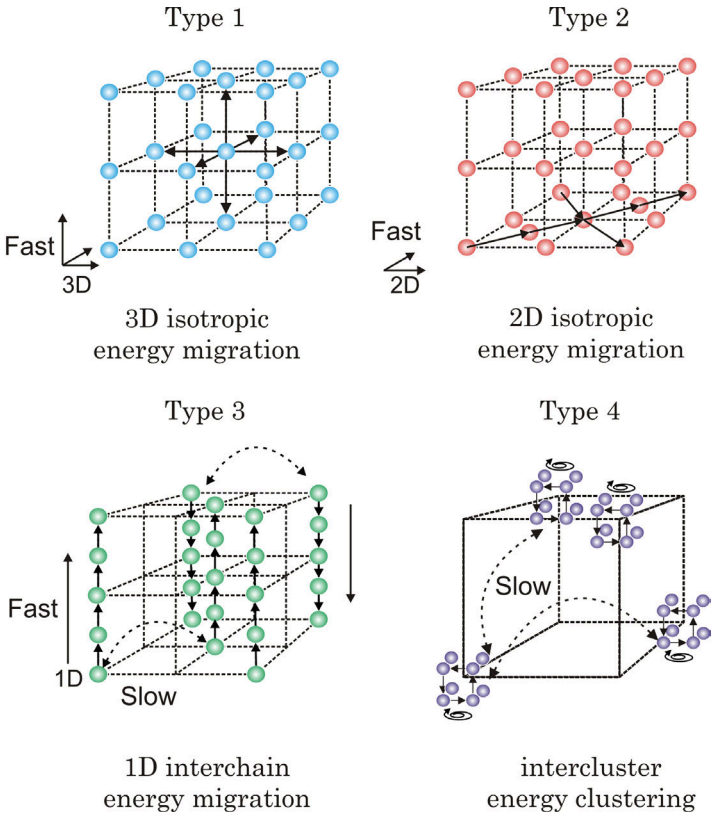

Scheme 3: Schematic representation of the topological energy migration pathways in different types of crystal sublattices. A random energy migration from one atom to its neighboring atoms in 3D, 2D and 1D (space dimension) is represented by the Type I,II and III, respectively. Type IV represents an energy transfer within sublattice clusters.

take place and/or different luminescence centers from each other. It is as well useful for understanding fundamental aspects like the energy migration between the same or different types of sensitizer ions for example Yb^{3+} or Nd^{3+}, in order to enhance upconversion luminescence properties. General points of interest are migration distances, efficiency of energy migration or mutual dependence between dopand concentration and migration distance.

The topological energy migration pathways in different types of crystal sublattices is shown exemplary in Scheme 3. In nanocrystals featuring a high symmetry unit cell for example an α-phase $NaYF_4$ (or CaF_2) a fast random energy migration between neighboring atoms will occur (see Scheme 3 type 1). The energy is isotropically distributed in a 3D structured crystal and the probability of long distance energy migration is increased.[78] In two-dimensional layered structures or one-dimensional chain crystal lattices fast energy migration can appear based on in-plane or chain lattice substituted dopand ions in close proximity. In this type 2 (for example between

Eu^{3+} ions in $NaEuTiO_4$) and type 3 (for example between Eu^{3+} ions in $EuMgB_5O_{10}$) crystal sublattices a preferential direction of energy migration exists.[78] Therefore in orthorhombic KYb_2F_7 crystals for instance (see Scheme 3 type 4) long distance energy migration is unfavored. In this crystal lattice arrays of isolated discrete atomic clusters are formed, where the distance between two different clusters is much longer than the distance of the ions within one cluster. The excitation energy is trapped in the discrete sublattice, which promotes localized energy exchange within one cluster.

1.3 Development of a Variable Setup for Multiparameter Upconversion Luminescence Studies

To get a comprehensive expertness of a certain UCM, several luminescence spectroscopy techniques like steady-state, time-resolved or excitation-emission matrix spectroscopy have to be applied. Related to the close connection of crystal structure/phonon coupling and upconversion emission properties, spectroscopic investigations at different temperatures (4 K to 328 K) and different excitation power densities will be of great interest.

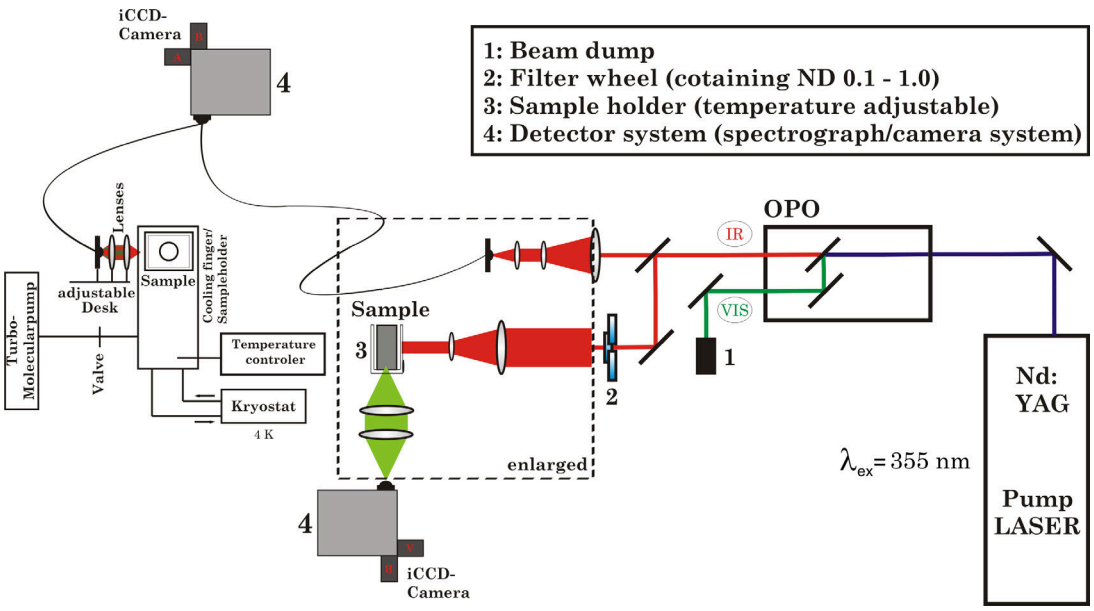

Figure 1.2: Schematic design of the established laser spectroscopic measurement system.

By using a wavelength tunable pulsed Nd:YAG/OPO laser system various excitation wavelengths 410 nm $< \lambda_{ex} <$ 2500 nm are accessible for upconversion and downconversion investigations. In combination with a filter wheel loaded with neutral

density filters (optical density (OD) 0.1 – 1.0) the intensity of upconversion emission as a function of excitation power at 976 nm (typically for Yb^{3+}) or 795 nm (typically for Nd^{3+}) is easy to access. In order to study the upconversion luminescence properties at various temperatures between 288 K < T < 328 K the experimental setup mentioned above was extended by a water-cooled Peltier element-based temperature adjustable sample holder. For low-temperature studies (4 K < T < 273 K), the sample has to be placed inside a liquid helium cryostat under high vacuum, whereas the excitation light has to be guided from the OPO laser to the sample and upconversion emission light has to be collected from inside the cooling chamber. A special sample holder for two samples per cooling cycle was constructed for very small quantities of solid as well as liquid samples. The excitation light was coupled into an Y-shaped optical fiber bundle using a lens system to maximize the light delivered to the sample. A second lens system was designed to collimate and focus the excitation light onto the sample and subsequently to collect the upconversion emission light and couple it back into the single fiber of the bundle for detection. An optimal aperture illumination of the spectrograph/camera system can be guaranteed by using a suitable collimator which is placed in front of the input slit of a spectrograph. The spectrograph is equipped with different gratings to achieve different spectral resolutions as well as an optimal illumination of the camera chip at various UC emission wavelengths. The light can be measured using either an iCCD camera (for time-gated detection) or a diode array (for NIR to MIR). A schematic view of the established setup is shown in Figure1.2.

1.4 Summary of the Scientific Attempt

The collective objective of the cumulative publications aims to explore a detailed understanding of the upconversion mechanism in nano-scaled $NaYF_4$ based materials co-doped with several lanthanides, e.g. Yb^{3+} and Er^{3+} as the "standard" type UCNP up to advanced UCNP with Gd^{3+} and Nd^{3+}. At first steady-state and time-resolved luminescence emission spectroscopy in combination with established techniques such as XRD and Raman spectroscopy was applied. In addition, high-resolution spectroscopy techniques at ultra-low temperature tailored to the demand to shed more light on the different energy transfer mechanisms involved for the "anti-Stokes" processes were performed. The overall results of the different luminescence spectroscopy techniques were correlated with the findings of structure (e.g., lanthanide composition or crystal structure), temperature and excitation power density investigations, to achieve a defined control and enhancement of the upconversion luminescence properties. Structural analysis was performed by established techniques such as XRD, DLS, TEM/REM and Raman spectroscopy. Finally, determining factors for a first potential application was enunciated in context of current needs and improvements of nanomaterial based optical sensors. Results gained by exploring these field of research were published and are included in chapter 2:

1. Phase Transitions in $NaYF_4$ Nanomaterial as Key Element to Efficient UC-luminescence
   Chapter 2.1: *J. Mater. Chem. C*, **2015**, *3*, 11228-11238.

2. Upconversion Luminescence: Unveiling the Single Intermediate Steps of the Cascade like Mechanism Behind
   Chapter 2.1: *J. Mater. Chem. C*, **2015**, *3*, 11228-11238.
   Chapter 2.2: *J. Phys. Chem. C*, **2015**, *119*, 3363-3373.

3. Fundamental Research and Challenges of an UC-based Nanothermometer
   Chapter 2.3: *RSC Adv.*, **2015**, *5*, 67149-67156.

2 Manuscripts

2.1 Phase Transitions in $NaYF_4$ Nanomaterial as Key Element to Efficient UC-luminescence

"Analysing the effect of the crystal structure on upconversion luminescence in Yb^{3+}, Er^{3+}-co-doped $NaYF_4$ nanomaterials"

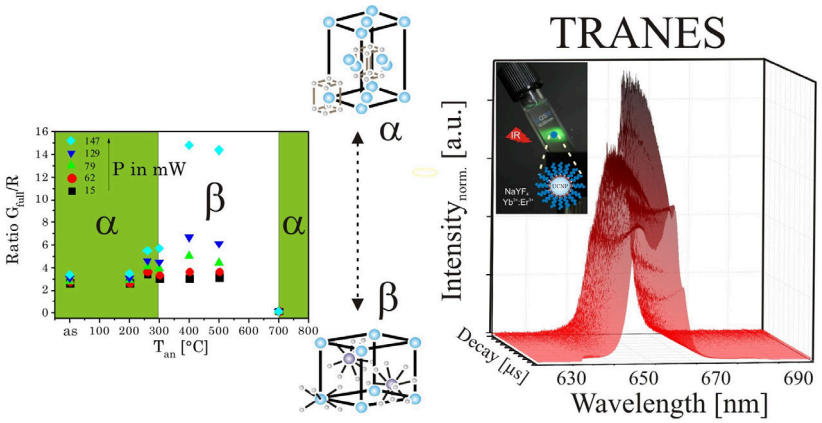

J. Mater. Chem. C, **2015**, *3*, 11228-11238.

Thesis pages: 17 – 27

Author Contribution to the manuscript:

I performed the complete synthesis of all nanoparticles as well as parts of the structural characterization (Raman investigations). I performed the steady-state, time-resolved and laser power dependent measurements. I completely analyzed and interpreted the photophysical-/ structural analytical data and prepared the spectra published. I performed the crystal phase fraction calculations by myself and wrote the manuscript, in close corporation with Michael Kumke.

Journal of Materials Chemistry C

PAPER

View Article Online
View Journal | View Issue

Cite this: *J. Mater. Chem. C*, 2015, 3, 11228

Analysing the effect of the crystal structure on upconversion luminescence in Yb^{3+},Er^{3+}-co-doped $NaYF_4$ nanomaterials†

D. T. Klier‡ and M. U. Kumke*‡

$NaYF_4$:Yb:Er nanoparticles (UCNP) were synthesized under mild experimental conditions to obtain a pure cubic lattice. Upon annealing at different temperatures up to T_{an} = 700 °C phase transitions to the hexagonal phase and back to the cubic phase were induced. The UCNP materials obtained for different T_{an} were characterized with respect to the lattice phase using standard XRD and Raman spectroscopy as well as steady state and time resolved upconversion luminescence. The standard techniques showed that for the annealing temperature range 300 °C < T_{an} < 600 °C the hexagonal lattice phase was dominant. For T_{an} < 300 °C hardly any change in the lattice phase could be deduced, whereas for T_{an} > 600 °C a back transfer to the α-phase was observed. Complementarily, the luminescence upconversion properties of the annealed UCNP materials were characterized in steady state and time resolved luminescence measurements. Distinct differences in the upconversion luminescence intensity, the spectral intensity distribution and the luminescence decay kinetics were found for the cubic and hexagonal lattice phases, respectively, corroborating the results of the standard analytical techniques used. In laser power dependent measurements of the upconversion luminescence intensity it was found that the green (G1, G2) and red (R) emission of Er^{3+} showed different effects of T_{an} on the number of required photons reflecting the differences in the population routes of different energy levels involved. Furthermore, the intensity ratio of G_{full}/R is highly effected by the laser power only when the β-phase is present, whereas the G1/G2 intensity ratio is only slightly effected regardless of the crystal phase. Moreover, based on different upconversion luminescence kinetics characteristics of the cubic and hexagonal phase time-resolved area normalized emission spectra (TRANES) proved to be a very sensitive tool to monitor the phase transition between cubic and hexagonal phases. Based on the TRANES analysis it was possible to resolve the lattice phase transition in more detail for 200 °C < T_{an} < 300 °C, which was not possible with the standard techniques.

Received 21st July 2015,
Accepted 24th September 2015

DOI: 10.1039/c5tc02218e

www.rsc.org/MaterialsC

1. Introduction

Nanomaterials labeled with fluorescent dyes have been widely used in life-science applications and biological studies.[1–6] Typically, these labeling compounds are organic dyes, such as Alexa Fluor, fluorescein isothiocyanate (FITC), cyanine dyes (Cy3, Cy5 or Cy7) and rhodamin derivates.[7–9] Recently, semiconductor quantum dots have emerged as great potential candidates for life-science applications.[10–16] These conventional down conversion luminescence probes require light in the ultra violet or visible spectral range for excitation. Their main disadvantages are the background-related auto-fluorescence of biological samples due to the UV/VIS excitation wavelengths typically used, photobleaching of the probes, low light penetration depth in tissues like skin and possible damages to the biological matrix under investigation.[1,7,17]

Upconversion (UC) luminescent materials have attracted great interest in recent years due to their outstanding photophysical properties and the resulting application potentials in various fields such as solid-state lasers, solar cells, color displays or life sciences.[18–27] Upconversion materials based on lanthanide-doped fluorides received a lot of attention owing to their high UC efficiency and photostability. Highly efficient UC materials among various fluoride based UC phosphors are β-phase $NaYF_4$ doped with Yb^{3+} and Er^{3+} or Yb^{3+} and Tm^{3+} as a sensitizer–activator pair, respectively.[28–33] The luminescence properties of upconversion nanoparticles (UCNP) are dependent on a complex interplay between different dopant ions on the one hand and the host lattice on the other hand.[8,9,34] Thus, the

University of Potsdam, Department of Chemistry (Physical Chemistry), Karl-Liebknecht-Str. 24-25, 14476 Potsdam, Germany. E-mail: kumke@uni-potsdam.de

† Electronic supplementary information (ESI) available: TEM image of $UCNP_{400}$ as well as further detailed XRD diffractograms of $UCNP_x$ and crystallite size out of the Debye–Scherrer calculation are shown. See DOI: 10.1039/c5tc02218e

‡ These authors equally contributed to this study.

View Article Online
Paper Journal of Materials Chemistry C

luminescence of these particles can be tuned by the crystal structure of the host lattice, the particle size, the ratio of different lanthanides used as dopants, and the power density of the excitation light.[35] For example, for $NaYF_4$ the host lattice geometry can be switched by annealing between the cubic (α) and the hexagonal (β) phases subsequently also tuning the UC properties of the materials.[20,36–39]

In the present study, the UCNPs were synthesized under mild reaction conditions ($T_{synthesis}$ = 160 °C) in order to obtain a pure cubic (α) phase host lattice. Subsequently, in order to investigate the influence of the crystal phase on the upconversion luminescence properties different annealing temperatures (T_{an}) were applied to induce a phase transition in the material. The alterations in the photophysical properties of the UCNP materials obtained for different T_{an} were monitored using steady state and time-resolved luminescence techniques. Time-resolved area normalized emission spectra (TRANES) can often be a useful method to illustrate the overall dynamics, especially to identify at least two emissive states.[40–45] Based on the luminescence data the interplay of the population routes of sensitizer and activator electronic states involved in different luminescence upconversion processes was analyzed in order to increase the understanding of the UCNP photophysics. The detailed knowledge of it at a molecular level provides the basis for UCNP material synthesis tailored for the specific needs of applications they are going to be used such as multiplexing applications like temperature sensing or *in vivo* imaging. The upconversion luminescence data are complemented by Raman, SEM and XRD measurements to determine the size and the crystal phase of the UCNP investigated and to underline the power of luminescence techniques in the structural characterization of such materials.

2. Experimental

2.1 Materials

All rare earth oxides RE_2O_3 (RE: Y, Yb and Er) were purchased from Chem Pur Feinchemikalien and Forschungsbedarf GmbH. Sodium fluoride (NH_4F, 99%) was purchased from Sigma Aldrich. Nitric acid solution (HNO_3, 65%), sodium chloride, polyvinylpyrrolidone (PVP 40) and ethanol (99.5%) were purchased from Carl Roth. In the experiments double distilled water was used. In the synthesis all chemical reagents were used as received.

2.2 Synthesis of $NaYF_4$:Yb^{3+}:Er^{3+} UCNPs

The UCNPs were synthesized according to a previously reported procedure in which a well-known hydrothermal method with PVP 40 as a capping agent was applied.[1,29,46] The rare earth nitrates ($RE(NO_3)_3$) were prepared from the corresponding oxides in stoichiometric amounts of Y_2O_3 (3.9 mmol), Yb_2O_3 (1.0 mmol) and Er_2O_3 (0.1 mmol) dissolved in nitric acid (200 mL, 10%) according to the literature method.[47] Typically, the obtained $RE(NO_3)_3$, was dissolved in 200 mL ethylene glycol and was treated with a mixture of NaCl (20 mmol) and 8.9 g PVP 40 (solution A). NH_4F (80 mmol) was dissolved in 200 mL ethylene glycol and heated to 80 °C in a second reaction vessel until a clear solution was obtained (solution B). Subsequently, solution A was heated to 80 °C and solution B was released into the hot solution within a few seconds. The combined solutions were heated to 160 °C. After 2 h the solution was cooled down to room temperature (RT) and the product was separated *via* centrifugation (4000 rpm for 20 min). The particles were further purified alternately with water and absolute ethanol. Finally, the precipitate was dried at 85 °C for 5 h and a white powder was obtained. Taking into account the amount of volatile organic material present in the material (approximately 11% mass loss according to thermo gravimetric studies) a yield of 75–90% was calculated. The composition of the UCNP is shown in Table 1. The chosen Er^{3+} concentration was small in order to eliminate possible cross relaxation between two excited Er^{3+} ions (see Scheme 1). To calculate the yields of the synthesis for different as-synthesized UCNPs a thermo-balance (L81 and STA PT-1600 Fa. Linseis) with simultaneously different thermal analysis (TG/DTA) was used.

Table 1 Nomenclature and basic parameters of the $UCNP_{AS}$ investigated. Particle size of $UCNP_{AS}$ nanoparticles was extracted from SEM images as well as calculated based on the Debye–Scherrer equation from XRD patterns

Parameter	$UCNP_{AS}$
Yb^{3+} : Er^{3+}	10 : 1
Mean diameter (SEM)/nm	41 ± 4
Mean diameter of nanocrystaline domain size (XRD)/nm	31 ± 7
T_{an}/°C	200–700 (for 5 h)
Steps of annealing/°C	ΔT = 20 (for 200–300 °C) ΔT = 100 (for 300–700 °C)

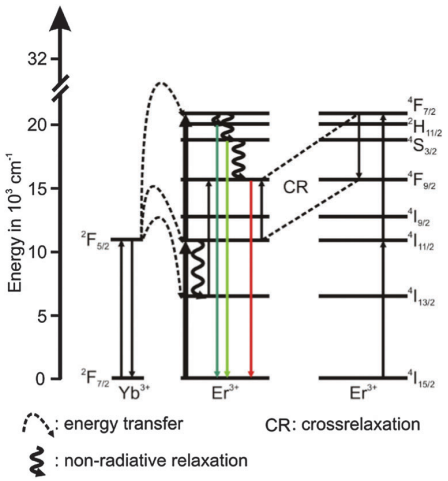

Scheme 1 Schematic energy level diagram for the upconversion related processes of the Yb^{3+} (sensitizer) Er^{3+} (activator) system following an excitation at λ_{ex} = 976 nm. The full lines pointing upwards represent absorption, the dotted lines represent energy transfer, the waved lines represent non-radiative relaxation processes and the colored full lines pointing downwards represent emission. The cross-relaxation between two excited Er^{3+} ions is represented by "CR".

View Article Online
Journal of Materials Chemistry C Paper

2.3 Annealing procedures

The as-synthesized $UCNP_{AS}$ were subjected to annealing at different temperatures T_{an} in a range of 200 °C < T_{an} < 700 °C for 5 h using a muffle furnace (LM 212.11, VEB Elektro) to induce phase transitions in the $NaYF_4$ host lattice (see Table 1). The UCNP materials are denoted as $UCNP_x$ with x = AS for as-synthesized and x = T_{an} (T_{an} = 200–700 °C).

2.4 Structural characterization

The size and morphology of the as-synthesized UCNP were obtained using a SEM S-4800 scanning electron microscope (Hitachi High-Technologies Canada, Inc., Toronto, Canada) operated with a cold field emission gun (FEG) as a cathode and an accelerating voltage of 2 kV. The samples were sputtered with platinum in order to reduce the tendency of electrostatic charging.

X-ray powder diffraction (XRD) patterns were collected using a D5005 instrument (Siemens AG, Munich, Germany) in a range of 3–70°/2θ with divergence aperture, scattering ray aperture and graphite monochromatized Cu K_α radiation (λ = 0.15406 nm). The scanning step was 0.02°/2θ with a counting time of 4 s per step. From the XRD spectra the nanocrystalline domain sizes were calculated using the Debye–Scherrer equation (see eqn (1)):

$$D = \frac{0.89\lambda}{B\cos(\theta)} \quad (1)$$

D is the domain size to be determined, λ is the wavelength of the X-ray, B is the FWHM of the diffraction peak of interest and θ is the angle of the corresponding diffraction peak.

Raman measurements were carried out using a confocal Raman microscope 300α (WITec Wissenschaftliche Instrumente und Technologie GmbH, Ulm, Germany) equipped with an upright optical microscope. For Raman excitation, laser light at λ = 532 nm was used, which was coupled into a single-mode optical fiber and focused through a 100× objective (Olympus MPlanFL N, NA = 0.9) to a diffraction-limited spot of about 1.3 μm^2. The laser power was set between 0.4 and 1 mW and the integration time was 5 s for all samples under investigation. For the detection the UHTS 300 spectrograph (WITec, Wissenschaftliche Instrumente und Technologie GmbH, Ulm, Germany) was equipped with a grating (600 lines per mm) and a cooled CCD camera (DU40LA-BR-DD-532, WITec, Wissenschaftliche Instrumente und Technologie GmbH, Ulm, Germany).

2.5 Luminescence characterization

2.5.1 Steady state and time resolved upconversion luminescence. Room temperature steady state and time resolved upconversion emission spectra of the solid samples were obtained using a wavelength tunable pulsed Nd:YAG/OPO laser system (pump laser: Quantaray, Spectra–Physics, Mountain View, CA, USA; OPO: GWU, GWU-Lasertechnik Vertriebsges. mbH, Erftstadt, Germany) operating at 20 Hz as an excitation light source and an intensified CCD-camera (iStar DH720-18H-13, Andor Technology, Belfast, Great Britain) coupled to a spectrograph (MS257 Modell 77700A, Oriel Instruments) equipped with a 300 l mm^{-1} grating as the detector. In order to record the time-resolved luminescence spectra (and subsequently extract the luminescence decay kinetics) the "box car" technique was applied. The initial gate delay t_I was set to 500 ns, the gate width was adjusted between 10–100 μs and 350 spectra were recorded. For the measurements of the luminescence decay kinetics the time delay between the laser excitation pulse and the detection window was step-wise increased by the variable gate-step size t_v (see eqn (2)). This way more data points at shorter times after the laser excitation pulse were acquired in order to ensure a reliable analysis of components with fast luminescence decay kinetics.

$$t(n) = t_I + t_v(n) = t_I + \sum_{i=1}^{n} (i-1)\cdot t_k \quad (2)$$

$t(n)$ consists of t_I, which is a constant of the chosen laser system and the constant step size t_k, which is a luminescence decay dependent system specific parameter. t_v is a variable step size and n (here n = 350) the number of spectra acquired to record the luminescence decay kinetics, which was evaluated by eqn (3):

$$I(t) = A + B_1\exp(-k_1 t) + B_2\exp(-k_2 t) \quad (3)$$

From coefficients B_1 and B_2 the relative fractions α_1 and α_2 were calculated according to eqn (4):

$$\alpha_1 = \frac{B_1\tau_1}{(B_1\tau_1 + B_2\tau_2)} \quad (4)$$

The solid samples were measured at room temperature using a specifically designed sample holder for powder samples. The sample holder consists of a cylindrical brass base body with two different thread units. A quartz disc is attached with anodized aluminium cover on one thread. The sample was filled in the base body and sealed with an anodized aluminium stamp. The upconversion luminescence was excited at λ_{ex} = 976 nm.

2.5.2 Time-resolved area normalized emission spectra (TRANES). Measurements for TRANES analysis were carried out using a wavelength tunable pulsed Nd:YAG/OPO laser system (laser: Quanta Ray, Spectra–Physics, Mountain View, CA, USA; OPO: GWU-Lasertechnik Vertriebsges. mbH, Erftstadt, Germany) operating at 10 Hz as an excitation light source (at 26 mJ/130 mW) and recorded using an intensified CCD-camera (iStar DH 720 18V 73, Andor Technology, Belfast, Great Britain) coupled to a spectrograph (Shamrock SR-303i, Andor Technology, Belfast, Great Britain) equipped with a 600 l mm^{-1} grating. The "box car" technique was applied for this set of measurements as well (*vide supra*). The initial gate delay was set to t_I = 500 ns and the gate width was adjusted between δt = 1–30 μs and 300 spectra were recorded. For the measurements the time delay between the laser excitation pulse and the detection window was step-wise increased by a constant gate-step size t_k (see eqn (5)).

$$t(n) = t_I + t_n(n) = t_I + (n-1)\cdot t_k \quad (5)$$

For the TRANES based component analysis it was considered that a mixed spectra m(λ) consists of a combination of the alpha and beta phase spectra $\alpha(\lambda)$ and $\beta(\lambda)$ with the relative fractions C and D, respectively (see eqn (6)).

View Article Online
Paper Journal of Materials Chemistry C

$$m(\lambda) = C\alpha(\lambda) + D\beta(\lambda) \quad (6)$$

The fractions (C and D) of α- and β-phases were calculated based on the least squares method.

3. Results and discussion

3.1 As-synthesized (cubic) $UCNP_{AS}$

3.1.1 Basic characterization. The as-synthesized sample was first examined by XRD for its phase composition. For the $NaYF_4$ host lattice two different thermodynamically stable phases, the cubic (isotropic) α-phase and the hexagonal (anisotropic) β-phase, are known.[20,48,49]

The XRD diffractogram of $UCNP_{AS}$ with the corresponding *Millerschen indices*[48] of the lattice planes is shown in Fig. 1 (left). A comparison of the XRD diffractogram with the database of the International center of diffraction data (ICCD, No. 77-2042) showed that $UCNP_{AS}$ is composed of the cubic α-phase found for $NaYF_4$. The very sharp reflexes of different lattice planes seen in the diffractograms indicate that even though the synthesis was carried out under mild conditions a defined crystal lattice was formed.

The particle size and morphology of $UCNP_{AS}$ were further studied using SEM. The SEM image of $UCNP_{AS}$ shows a cubic shape (Fig. 1, right).[50–53] In order to determine an average particle size from SEM images approximately 500 particles were evaluated. The results of the statistical analysis of the SEM images are shown in Table 1. In addition, the particle size was calculated using the Debye–Scherrer equation. Here, the XRD data were fitted with Lorentz functions and the average particle diameter was obtained. In comparison to the SEM-based size the average diameter is determined approximately 25% smaller. Based on the Debye–Scherrer equation only the crystallite size of the particle is considered in the calculation, which accounts for the observed difference in size found by the two methods. Because of the mild synthesis conditions, the $UCNP_{AS}$ may not be fully crystallized and some amorphous domains may still be present in the particles.

3.1.2 Upconversion luminescence. In Fig. 2 (left) the luminescence spectrum of $UCNP_{AS}$ at λ_{ex} = 976 nm is shown. The three typical emission bands can be observed in the green spectral region centered at λ_{em} = 525 nm ($^2H_{11/2} \rightarrow {}^4I_{15/2}$ transition, G1), λ_{em} = 545 nm ($^4S_{3/2} \rightarrow {}^4I_{15/2}$ transition, G2)

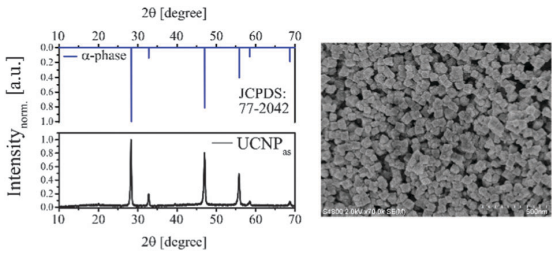

Fig. 1 (left) The XRD diffractogram of as-synthesized $UCNP_{AS}$ (and the corresponding reference data from JCPDS) indicates that the sample is composed of the pure cubic α-phase. (right) SEM image (500 nm scale) of $UCNP_{AS}$.

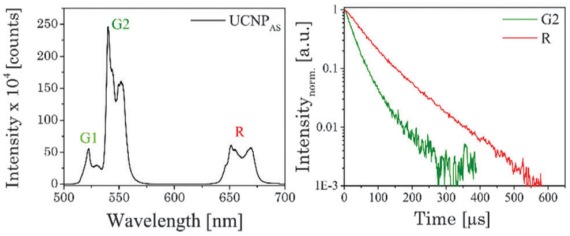

Fig. 2 (left) Upconversion luminescence spectrum of the as-synthesized $UCNP_{AS}$. The spectrum was recorded from a powdered sample with λ_{ex} = 976 nm (power density of 191 mW cm^{-2}). (right) Normalized upconversion luminescence decay kinetics of the Er^{3+} emission bands G2 and R of $UCNP_{AS}$.

Table 2 Luminescence decay times τ with different time components and relative fractions of the as-synthesized $UCNP_{AS}$ for the emission bands G2 and R, respectively

Decay time [µs]	$UCNP_{AS}$	Relative fraction [%]
$\tau_{G2,1}$	23 ± 1	71
$\tau_{G2,2}$	65 ± 5	29
$\tau_{R,1}$	51 ± 1	64
$\tau_{R,2}$	118 ± 6	36

and in the red spectral region centered at λ_{em} = 660 nm ($^4F_{9/2} \rightarrow {}^4I_{15/2}$ transition, R) (see also Scheme 1).[9,54–57] The observed fine structures (Stark splitting) within the major emission peaks is induced by the crystal field of the ligands positioned around the Er^{3+} ions in the host lattice.[55,56,58,59]

Fig. 2 (right) shows the luminescence decay kinetics (λ_{ex} = 976 nm) of $UCNP_{AS}$ G and R, respectively. For the emission bands G2 and R a distinctly different time dependence of the luminescence was observed (see Fig. 2, right), whereas no difference between G1 and G2 was observed (see ESI,† Fig. S1). In the data analysis a bi-exponential decay law was applied.[55,60,61] As a trend, the calculated luminescence decay times (τ_1 and τ_2) were longer for the red emission band (R) compared to the green emission bands (G1, G2) (Table 2).

3.2 Annealed $UCNP_x$

The $NaYF_4$ lattice shows a phase transition from cubic to hexagonal and as a consequence the upconversion properties of UCNPs are distinctly influenced due to structure-related parameters like lattice vibrations. To study the phase transfer from the cubic (α) to the hexagonal (β) phase in more detail the $UCNP_{AS}$ were annealed at different temperatures T_{an}.

At T_{an} > 400 °C the nanoparticles tend to build up micro-domains (see ESI,† Fig. S2); therefore the samples are further denoted as $UCNP_x$ materials.[7]

3.2.1 XRD. In Fig. 3 selected XRD diffraction patterns of $UCNP_x$ after annealing in the temperature range of 200 °C < T_{an} < 700 °C for 5 h are shown. The overall intensity of the diffraction patterns was increased with increasing temperature T_{an} (see ESI,† Fig. S3), whereas the FWHM of the different peaks stayed unaltered (see ESI,† Fig. S3). The increase in intensity is a good indication for an improved crystallinity of the $UCNP_x$ upon annealing. The crystallite size was calculated using the

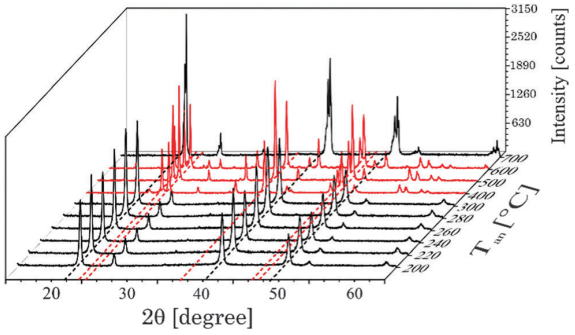

Fig. 3 Suited selection of X-ray diffraction patterns of $UCNP_x$ after annealing between 200 °C < T_{an} < 700 °C for 5 h. The black dotted lines correspond to the position of reflexes of the cubic phase whereas red dotted lines correspond to the position of reflexes of the hexagonal phase, respectively.

Debye–Scherrer equation (see ESI,† Table S1). It is obvious that there is a slight increase of the crystallite size for UCNPs annealed at T_{an} < 300 °C, whereas for 300 °C < T_{an} < 600 °C a significant increase of the crystallite size was found due to the change of the crystal phase of the host lattice and the formation of micro-domains. In Fig. 3 for annealing temperatures below 300 °C only the cubic phase is observed in the XRD diffractogram, while for an annealing temperature of T_{an} = 400 °C the hexagonal phase is clearly seen as the major crystal phase. The relative fraction of this phase gradually increased with increasing T_{an} up to 500 °C. Based on the XRD data (for 400 °C < T_{an} < 500 °C) only a minor amount of cubic phase seems to be present in the material (see Fig. 4). A further increase of T_{an} > 500 °C leads however to a decrease of the hexagonal phase and at T_{an} = 700 °C again mainly the cubic phase was found in the XRD diffractograms. From Fig. 3 it can be seen that the $UCNP_{700}$ material is slightly different in the observed XRD peak pattern indicating that the phase back transfer may not be fully completed. This has been observed before for bulk materials by Hebert *et al.*[62–64]

3.2.2 Raman spectroscopy. In the Raman spectra of $UCNP_{AS}$ (cubic phase) two dominant broad bands around ν = 275 cm^{-1} and 745 cm^{-1} were observed, which were also found for $UCNP_x$ annealed up to T_{an} < 300 °C. Moreover, the comparison of the samples annealed at T_{an} < 300 °C and the sample annealed at T_{an} = 700 °C showed only small differences with respect to the peak position and spectral distribution (see Fig. 5, left top). These results are complementary to the corresponding XRD data (*vide supra*) pointing to a cubic phase for the respective materials. The Raman spectra of the hexagonal phase materials display five main peaks at ν = 251 cm^{-1}, 303 cm^{-1}, 359 cm^{-1}, 492 cm^{-1} and 625 cm^{-1}, whereas the high phonon vibrational bands ν > 700 cm^{-1}, which have been found for the cubic phase materials, are only weakly present (see Fig. 5).[65,66] The observed alterations in the Raman spectra are well correlated with the phase transition of the host lattice seen in the XRD diffractograms. Moreover, also the small differences between the sample annealed at T_{an} = 700 °C and samples for T_{an} < 300 °C are confirmed by the Raman spectra (see Fig. 5).

3.2.3 Upconversion luminescence. The upconversion luminescence of the UCNP materials is investigated in detail using (quasi) steady state and time-resolved luminescence techniques. In the (quasi) steady state luminescence measurements a detection window of 500 μs was used collecting more than 95% of the overall luminescence intensity. In the upconversion luminescence spectra the intensity as well as the spectral intensity distribution were altered due to annealing (see Fig. 6). For T_{an} < 300 °C a small increase in the upconversion luminescence intensity was found, but no alteration in the spectral intensity distribution was observed (see ESI,† Fig. S4). For annealing temperatures in the range of 300 °C < T_{an} < 600 °C a distinct increase in the overall upconversion luminescence intensity was found with a maximum at T_{an} = 500 °C.[18,68–70] In addition, for this set of samples the spectral intensity distribution was changed as well. Within different emission bands (G1, G2, and R) Stark level-related substructures became apparent, but also the relative contribution of the G- and R-bands was altered (see Fig. 6).

While the ratio of G1/G2 was found to be nearly independent of the annealing temperature the ratio G2/R showed a distinct change for T_{an} > 300 °C (see Fig. 6). The sample obtained at

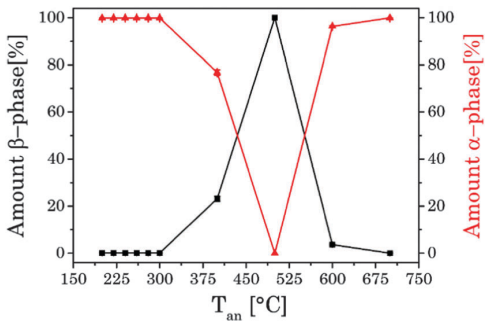

Fig. 4 Amount of α- and β-phase in correlation with temperature of the thermal treatment, calculated on the intensity of different XRD reflexes of α- and β-phases.

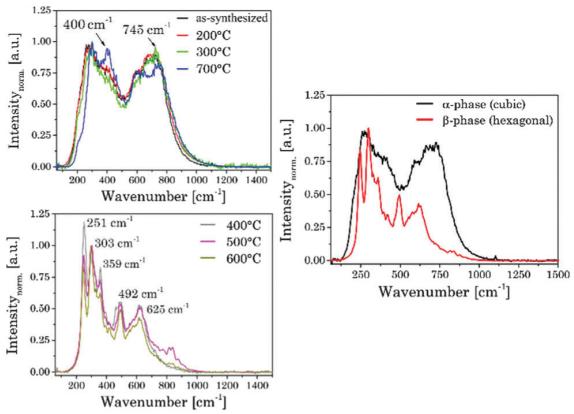

Fig. 5 (left) Normalized Raman spectra of the as-synthesized $UCNP_{AS}$ and annealed $UCNP_x$. (right) Representative Raman spectra of α- and β-phases.

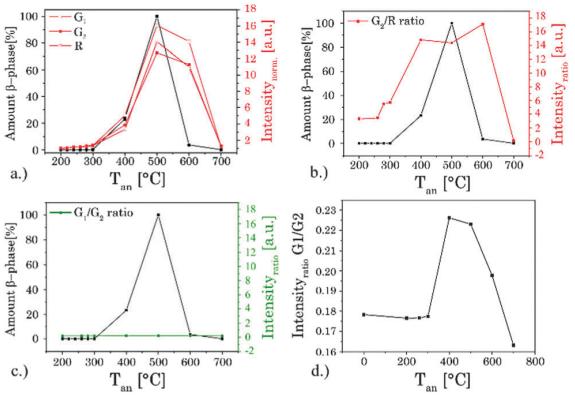

Fig. 6 (a) Alteration in the (quasi) steady state intensity of different luminescence bands with annealing temperature T_{an}. The ratio G2/R (b) and G1/G2 (c) based on the integrated steady state luminescence intensity of these emission bands and the amount of hexagonal β-phase, both as a function of temperature T_{an}. The amount of β-phase was calculated based on XRD measurements. (d) Enlargement of the G1/G2 ratio over T_{an}.

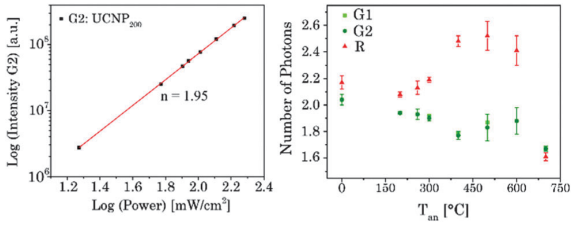

Fig. 7 (left) Dependence of upconversion luminescence intensity on laser power for G2 related emission of $UCNP_{200}$. (right) *n*-Values determined for the emission bands G1, G2, and R for $UCNP_x$ annealed at different T_{an}.

T_{an} = 700 °C showed a reversed effect, here the overall intensity as well as the spectral intensity distribution were changed back according to materials obtained for T_{an} < 300 °C. In Fig. 6 the overall intensity, the ratio G2/R (as well as the G1/G2 ratio), and the amount of β-phase in different samples are compared.[71] The spectral changes are well correlated with the phase transition from the cubic (α) phase to the hexagonal (β) phase corroborating the results of the XRD and Raman measurements.[34,41,44] In addition, for high T_{an} a reduction in lattice defects due to the annealing process and a subsequent decrease of radiationless deactivation improving the energy migration between Yb^{3+} ions within the crystal may also have a positive effect on the overall upconversion luminescence intensity.

3.2.4 Laser power dependent luminescence measurements. The UC luminescence intensity (I_{UC}) is proportional to the "*n*th" of excitation power (I_{IR}) (see eqn (7)).

$$I_{UC} \sim I_{IR}^{n} \quad (7)$$

n is the number of absorbed NIR photons per visible photon emitted and can be obtained from the slope of log(I_{UC}) *versus* log(I_{IR}) analysis (see Fig. 7).[61,72–76]

For G1 and G2 luminescence two NIR photons need to be transferred (*n* = 2, see Fig. 7) from two Yb^{3+} ions (sensitizer) to one Er^{3+} ion (activator).[61,72,73]

First, the $^4I_{11/2}$ energy level and then the $^4F_{7/2}$ energy level of Er^{3+} are populated. Followed by a non-radiative deactivation from the $^4F_{7/2}$ to the $^2H_{11/2}$ energy level (G1) or further to the $^4S_{3/2}$ energy level (G2). Alternatively the $^4S_{3/2}$ energy level can also be deactivated non-radiatively through multiphonon interaction with the host lattice to the $^4F_{9/2}$ energy level yielding the emission band R (also *via* two energy transfer steps, *n* = 2). In addition, the $^4F_{9/2}$ energy level can be populated *via* the two different three photon energy transfer process (*n* = 3).[20,55,56,67,77]

The $^4S_{3/2}$ energy level of one Er^{3+} ion is populated by two energy transfer steps from excited Yb^{3+} ions whereas a second Er^{3+} ion is in the $^4I_{11/2}$ energy level *via* one energy transfer step from Yb^{3+}. Following a cross relaxation between the two excited Er^{3+} ions both Er^{3+} ions reached the $^4F_{9/2}$ energy level from which the red emission (R) can occur (three photon process A). The three photon process A is only possible at high Er^{3+} concentration and can be neglected in our materials due to the low Er^{3+} concentration.[57,67,78–80] In a second three photon process B the $^4S_{3/2}$ energy level of the Er^{3+} ion is populated by two energy transfer steps from excited Yb^{3+} ions. Then, the $^4I_{13/2}$ level of Er^{3+} can be populated *via* an energy back transfer (BET) from the $^4S_{3/2}$ level of Er^{3+} to neighbouring Yb^{3+} ions.[81] A subsequent energy transfer from excited Yb^{3+} ions to the $^4I_{13/2}$ level of Er^{3+} leads to the population of the $^4F_{9/2}$ energy level and the red emission band R.[82] The *n*-value for G1 and G2 is slightly, but steadily decreased with increasing annealing temperature from *n* − 2 ($UCNP_{AS}$) to *n* − 1.7 (for T_{an} = 700 °C) (see Fig. 7, right). In contrast the *n*-value for the R band increased from *n* − 2.1 ($UCNP_{AS}$) to *n* − 2.5 (T_{an} = 600 °C). A distinct difference in the *n*-values is found for the cubic phase ($UCNP_{AS}$) and the hexagonal phase ($UCNP_{400}$), but already at T_{an} < 400 °C a slight but steady change in the *n*-values was observed (see Fig. 7 (right)). Opposing effects originating from the differences in phonon coupling in the cubic and hexagonal lattices as well as from the interplay between radiationless deactivation and saturation effects at higher laser power may be the reason for the observed trends in *n* for the G and R band(s), respectively. While for the green emission bands G1 and G2 theoretically *n* = 2 is expected and the observed decrease of *n* with increasing T_{an} points toward a saturation effect, for the R band the change in the matrix-related phonon coupling is the major factor responsible for the overall increase of *n*.[61,83] To further elucidate different factors the power dependence of the spectral intensity distribution was analyzed in more detail. In Fig. 8 the ratio of the green luminescence bands G1/G2 (left) as well as the ratio of the overall green and red luminescence G_{full}/R (right) are shown for different laser power (λ_{ex} = 976 nm). For the G1/G2 ratio almost no influence of the laser power is found for the $UCNP_x$ annealed at T_{an} < 300 °C. For T_{an} > 300 °C a slight jump in the G1/G2 ratio was found but no significant influence of the laser power. The observed "jump" falls well within the range of T_{an} for which the hexagonal phase is dominant.[72,74] At T_{an} = 700 °C a decrease and a slight power dependence were observed for the G1/G2 ratio. It is known that G1 is mainly populated *via* thermal excitation from the $^4S_{3/2}$ level (G2). The energy gap between the

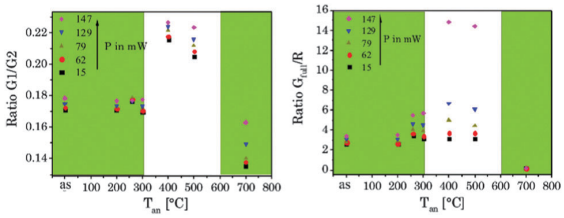

Fig. 8 Peak ratio G1/G2 (left) and G_{full}/R (right) *versus* annealing temperature at different laser power *P*. The green inlet represents the alpha phase and the white inlet the beta phase of the host lattice (λ_{ex} = 976 nm).

$^4S_{3/2}$ – and $^2H_{11/2}$ level is decreased due to thermal treatment (associated therewith phase transfer from the α- to β-phase) and leads to a more efficient thermal population of the $^2H_{11/2}$ level, subsequently increasing the G1/G2 ratio (see Fig. 8, left). In contrast, for the G_{full}/R ratio a distinct laser power dependence was found. Especially in the range of 300 °C < T_{an} ≤ 600 °C representative for the hexagonal phase a large increase by a factor of about 7 was measured (see Fig. 8, right). As for the G1/G2 ratio at T_{an} = 700 °C the G_{full}/R ratio dropped back (even below) to the value found for T_{an} < 300 °C and the laser power influence disappeared. The energy mismatch of the $^2F_{5/2}$ level of Yb^{3+} and the $^4I_{11/2}$ level of Er^{3+} is smaller in the hexagonal phase than in the cubic phase and a better phonon matched energy transfer process between Yb^{3+}- and Er^{3+}-ions is possible which accounts for the observed lattice phase influence (especially for the G1/G2 ratio). The possibility of saturation effects (*e.g.*, BET, cross relaxation) might also be increased due to the improved phonon matching. In the case of the G_{full}/R ratio the alteration of the R is the dominant factor. In the case of a high concentration of excited Yb^{3+} ions (sensitizers) the activation into the $^4F_{7/2}$ state becomes faster and can successfully compete with the radiationless deactivation from the $^4I_{11/2}$ into the $^4I_{13/2}$ state, which is a necessary prior step to the activation into the $^4F_{9/2}$ state. From the $^4F_{9/2}$ state R emission occurs subsequently (see Scheme 2).

3.2.5 Time-resolved luminescence. The luminescence decay kinetics of the $UCNP_x$ materials showed a complex time dependence. In Fig. 9 the luminescence decay kinetics (λ_{ex} = 976 nm) of $UCNP_{300}$ is shown for the two emission bands G2 and R. It can be seen that the kinetics of the two bands shows a distinctly different time dependence.

For R an initial rise in the luminescence intensity is observed (for t < 500 μs, see Fig. 9). The complexity of the observed decay kinetics could be a result of the contributions from Er^{3+} ions located in different chemical environments (*e.g.*, surface *vs.* volume effects, amorphous domains, which are reduced due to annealing). The experimental data of G1, G2 and R were analyzed by a bi-exponential decay kinetics.

Luminescence decay times τ_1 and τ_2 were calculated for different bands G1, G2 and R of the $UCNP_x$ materials. An increase in both luminescence decay times with increasing T_{an} was observed. Moreover, at T_{an} > 300 °C for both luminescence decay times an accelerated increase with increasing T_{an} was calculated (see Fig. 10). This trend in the decay time is accompanied by the crystal phase transfer from cubic to hexagonal (*vide supra*).

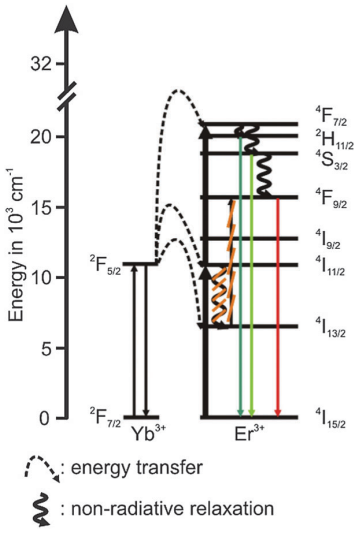

Scheme 2 Energy scheme of the upconversion processes in the hexagonal phase with suppressed population route of the $^4F_{9/2}$ level (underlined by the orange lines).

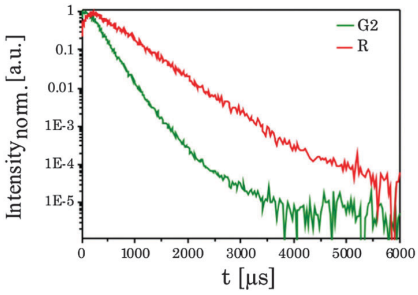

Fig. 9 Normalized upconversion luminescence decays of the G2 and R bands of Er^{3+} in $UCNP_{300}$ (λ_{ex} = 976 nm).

The drop observed for τ_1 and τ_2 at T_{an} = 700 °C (here, the material switched back to a cubic phase) supports the correlation of the luminescence decay kinetics and the lattice phase. The results of the luminescence kinetics measurements are in very good agreement with the other spectroscopic data presented for the G1/G2 and G_{full}/R ratios.

3.2.6 Time-resolved area normalized emission spectra (TRANES). In order to pinpoint the influence of the lattice on the luminescence upconversion the time-resolved emission spectra were evaluated by TRANES analysis. TRANES can be used to reveal small time-dependent variations in the spectral intensity distribution of a luminescence spectrum. They were calculated from the time-resolved emission spectra recorded for the determination of the luminescence decay kinetics by normalizing the area of the emission spectrum recorded at different delay times after the laser pulse (*e.g.*, area of spectrum is normalized to one). In Fig. 11 (top) the TRANES of $UCNP_{200}$ are shown. No change in the spectral intensity distribution neither for the G1 and G2 luminescence nor for the R

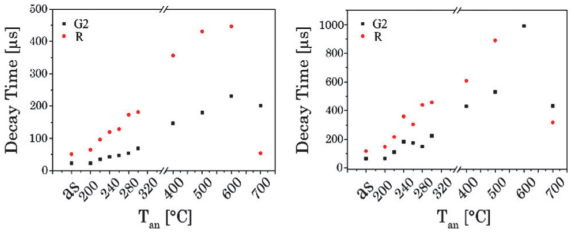

Fig. 10 Luminescence decay times of UCNPs annealed at different T_{an} for the emission bands G2 and R, (left) the short decay component, (right) and the long decay component (λ_{ex} = 976 nm).

luminescence is detected. For $UCNP_{300}$ a significant change in the intensity distribution of the luminescence is found for G1 and G2 as well as for R (see Fig. 12). In the TRANES isoemissive points are found. For example, for G1 isoemissive points can be seen at λ_{em} = 516.8 nm, 521.8 nm and 523.2 nm and the luminescence peak at λ_{em} = 529 nm becomes more pronounced (see Fig. S4, ESI†). Also in the case of G2 the intensity distribution is altered with increasing delay relative to the excitation pulse. For the R luminescence two isoemissive points are identified at λ_{em} = 651 nm and 665.8 nm. Furthermore, the shoulder at λ_{em} = 668 nm is decreased whereas a completely new peak appears at λ_{em} = 661 nm. In Fig. 11 the upconversion emission spectra of $UCNP_{400}$ and $UCNP_{600}$ are shown as well. The variations in the spectral intensity distribution of G1 and G2 as of R are small for both materials (the luminescence intensity

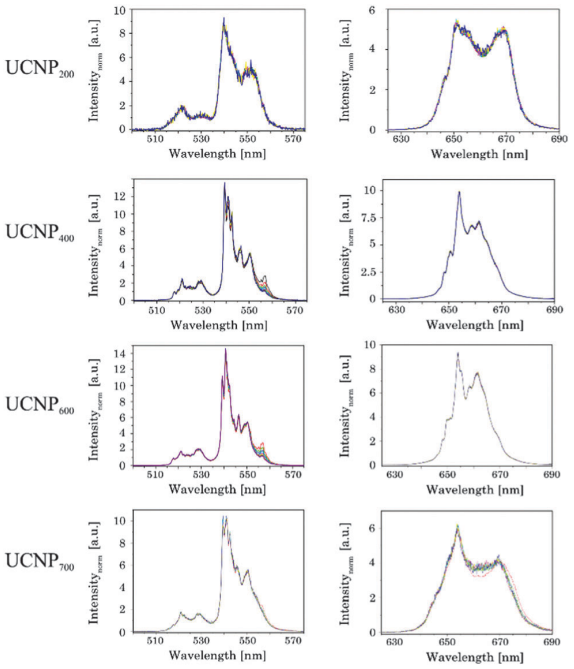

Fig. 11 TRANES of annealed $UCNP_x$ (200 °C < x < 700 °C) for (left) G1 and G2 luminescence as well as (right) of R luminescence are shown (λ_{ex} = 976 nm). The delay after the laser pulse was varied between 0 µs and 2000 µs.

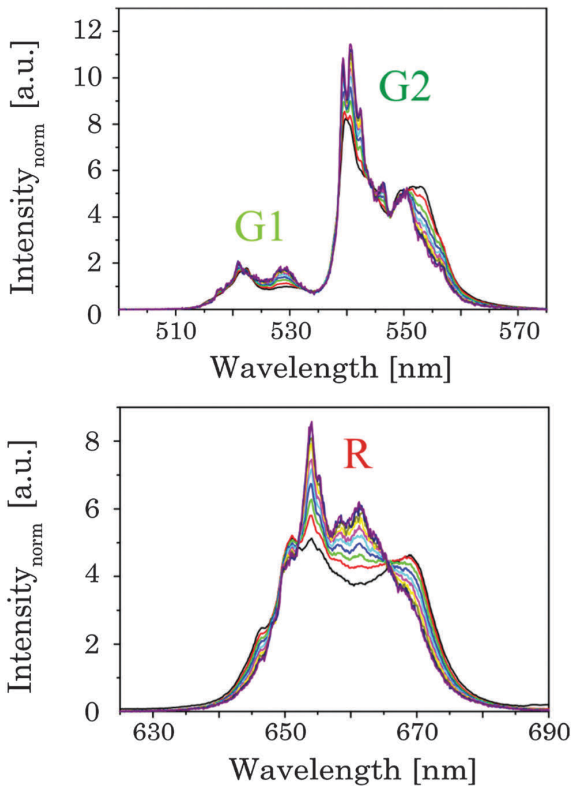

Fig. 12 TRANES of annealed $UCNP_{300}$ for (up) G1 and G2 luminescence as well as (below) of R luminescence are shown (λ_{ex} = 976 nm). The delay after the laser pulse was varied between 0 µs and 2000 µs (displayed by the colors in 120 µs steps).

distribution is only slightly changed for the emission band G2). For the TRANES analysis of $UCNP_{700}$ it can be seen that the spectral intensity distribution remains unchanged with increasing delay time. Moreover, a comparison with the spectra of $UCNP_{200}$–$UCNP_{600}$ materials shows that for the $UCNP_{700}$ material a close resemblance to the $UCNP_{200}$ material is found (especially for the R luminescence). The results of the TRANES analysis nicely complement the data of the other experimental techniques reflecting the phase transition from cubic to hexagonal (and back to cubic) upon annealing in the temperature range 200 °C < T_{an} < 700 °C. However, while the other analytical techniques and data evaluation approaches gave only a rough picture of the phase transfer and its initial temperature T_{an}, in the TRANES analysis of the G1, G2 and R emission bands already small fractions of the hexagonal phase could be detected. The fact that the shape of the emission bands is changed with increasing delay time after the laser pulse in favor of the hexagonal phase related luminescence is a consequence of the significant differences in the decay times of Er^{3+} luminescence in the two lattice phases involved due to difference in the symmetry of the chemical environment (*vide supra*). Consequently the relative luminescence intensity contribution of Er^{3+} ions located in the cubic and hexagonal phases changes with time after the laser pulse and different lattice environments, if present, can be identified in

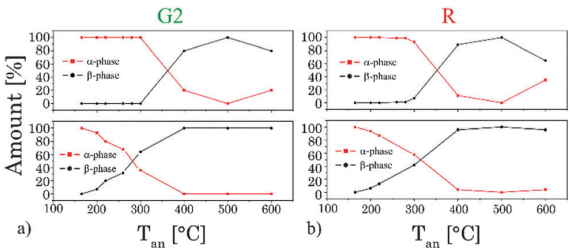

Fig. 13 Variation of the amount of different crystal phases (α- and β-phases) calculated out of the TRANES analysis at delay times after the laser pulse (top: 0 μs and bottom: 500 μs) for emission bands G2 (a) and R (b).

the sample from the alteration in the spectral intensity distribution. The TRANES analysis is very sensitive and allows the analysis of even a small difference in the material composition. The small differences in the intensity distribution of G1 and G2 of the $UCNP_{700}$ material compared to $UCNP_{200}$ indicate a small fraction of the hexagonal phase to be still present in this material. For a complete back transfer to the cubic phase higher temperatures or/and longer annealing times seem to be necessary. Based on the diffractogram and the corresponding Debye–Scherrer calculations an increase in the crystallite size as well as an asymmetric growth of the UCNP was found, which could also have an impact on the intensity distribution of G1 and G2 of the $UCNP_{700}$ material. Based on the approximation that in the $UCNP_{AS}$ and the $UCNP_{500}$ only cubic and hexagonal phases, respectively, are present, a spectral decomposition of the emission spectra recorded at a delay time of 0 μs and 500 μs was performed in order to calculate the relative amount of cubic and hexagonal phases for different $UCNP_x$ materials (see Fig. 13). It can be seen that in the temperature range of 200 °C $< T_{an} <$ 400 °C a gradual transformation of the cubic into the hexagonal phase is already present.

4. Conclusion

$NaYF_4$ nanoparticles co-doped with Er^{3+} and Yb^{3+} were synthesized under mild conditions using PVP 40 as a capping agent and as a stabilizer, respectively. The $UCNP_{AS}$ were uniform in size and shape with a cubic crystal lattice. After annealing between 200 °C $< T_{an} <$ 700 °C for 5 h changes in the crystal lattice phase and subsequently in the upconversion luminescence properties of the UCNP materials were induced. The lattice phase and the structure of the UCNP materials obtained at different T_{an} were analyzed using XRD, Raman spectroscopy as well as SEM. The upconversion luminescence properties of the annealed UCNP materials were studied by steady state and time resolved luminescence. Upconversion luminescence proved to be a sensitive tool to monitor the phase transition of the host lattice. While based on XRD and Raman spectroscopy no clear indication for a change in the lattice phase was found for $T_{an} <$ 300 °C, the upconversion luminescence proved to be more sensitively capable of resolving even small contributions of cubic and hexagonal phases, respectively, in the materials. Based on the upconversion fluorescence studies of the $UCNP_x$ materials the complex interplay of the host lattice crystal phases and the population routes of the Er^{3+} energy levels involved in the upconversion processes was evaluated. The laser power dependence of the green (G1, G2) and red (R) luminescence was found to be dependent on the annealing temperature. In addition, green and red luminescence was found to respond differently in the host lattice phase. A major population route of the R luminescence is attenuated at higher laser power, which is more efficient for the hexagonal lattice phase; the relative contributions expressed as the ratio between G_{full} and R are altered (see Scheme 2). Although already regular upconversion data, like spectral intensity distribution from steady state luminescence measurements or luminescence decay kinetics, show a clear lattice phase dependent behavior, TRANES analysis proved to be superior. The basis for the full exploitation of the power of TRANES is the different luminescence decay kinetics of the upconversion in cubic and hexagonal lattice phases. Because the analysis of the luminescence kinetics with respect to physical meaningful luminescence decay times is difficult due to the complex time dependence and the related challenges in the data analysis, TRANES employ a model-free combination of time and spectral information. Based on TRANES even minor amounts of cubic or hexagonal phase could be identified in different UCNP materials. TRANES could also be a great tool for monitoring the phase composition of UCNP *in situ* during synthesis.[84,85]

Acknowledgements

We are thankful to Dr C. Günter and Dr C. Prietzel (work group of Prof. J. Kötz) for XRD and SEM measurements of the samples, respectively.

References

1 Z. Li and Y. Zhang, *Angew. Chem., Int. Ed.*, 2006, **45**, 7732–7735.
2 J. Yin, Y. Hu and J. Yoon, *Chem. Soc. Rev.*, 2015, **44**, 4619–4644.
3 N. Kaur, W. Hyland and J. F. Callan, *Chem. Soc. Rev.*, 2015, **44**, 4415–4432.
4 T. D. Ashton, K. a. Jolliffe and F. M. Pfeffer, *Chem. Soc. Rev.*, 2015, **44**, 4547–4595.
5 Y. Tang, D. Lee, J. Wang, G. Li, J. Yu, W. Lin and J. Yoon, *Chem. Soc. Rev.*, 2015, **44**, 5003–5015.
6 L. Niu, Y. Chen, H. Zheng, L. Wu, C. Tung and Y. Chen, *Chem. Soc. Rev.*, 2015, **44**, 6143–6160.
7 G. Yi, H. Lu, S. Zhao, Y. Ge and W. Yang, *Nano Lett.*, 2004, **4**, 2191–2196.
8 J. Shan, W. Kong, R. Wei, N. Yao and Y. Ju, *J. Appl. Phys.*, 2010, **107**, 054901.
9 K. Wu, J. Cui, X. Kong and Y. Wang, *J. Appl. Phys.*, 2011, **110**, 053510.
10 J. Shen, Y. Zhu, X. Yang and C. Li, *Chem. Commun.*, 2012, **48**, 3686.

11 S. Zhu, J. Zhang, C. Qiao, S. Tang, Y. Li, W. Yuan, B. Li, L. Tian, F. Liu, R. Hu, H. Gao, H. Wei, H. Zhang, H. Sun and B. Yang, *Chem. Commun.*, 2011, **47**, 6858–6860.
12 M. Montalti, A. Cantelli and G. Battistelli, *Chem. Soc. Rev.*, 2015, **44**, 4853–4921.
13 S. Silvi and A. Credi, *Chem. Soc. Rev.*, 2015, **44**, 4275–4289.
14 K. D. Wegner, N. Hildebrandt and N. Hildebrandt, *Chem. Soc. Rev.*, 2015, **44**, 4792–4834.
15 O. S. Wolfbeis, *Chem. Soc. Rev.*, 2015, **44**, 4743–4768.
16 H. Peng and D. T. Chiu, *Chem. Soc. Rev.*, 2015, **44**, 4699–4722.
17 J. Thomas, *Chem. Soc. Rev.*, 2015, **44**, 4494–4500.
18 J. Zhou, Z. Liu and F. Li, *Chem. Soc. Rev.*, 2012, **41**, 1323.
19 Q. Liu, Y. Sun, T. Yang, W. Feng, C. Li and F. Li, *J. Am. Chem. Soc.*, 2011, **133**, 17122–17125.
20 F. Wang, Y. Han, C. S. Lim, Y. Lu, J. Wang, J. Xu, H. Chen, C. Zhang, M. Hong and X. Liu, *Nature*, 2010, **463**, 1061–1065.
21 E. M. Chan, *Chem. Soc. Rev.*, 2015, **44**, 1653–1679.
22 N. M. Idris, M. K. G. Jayakumar, A. Bansal and Y. Zhang, *Chem. Soc. Rev.*, 2014, **44**, 1449–1478.
23 A. Sedlmeier and H. H. Gorris, *Chem. Soc. Rev.*, 2014, **44**, 1526–1560.
24 M.-K. Tsang, G. Bai and J. Hao, *Chem. Soc. Rev.*, 2015, **44**, 1585–1607.
25 D. Yang, P. Ma, Z. Hou, Z. Cheng, C. Li and J. Lin, *Chem. Soc. Rev.*, 2014, **44**, 1416–1448.
26 W. Zheng, P. Huang, D. Tu, E. Ma, H. Zhu and X. Chen, *Chem. Soc. Rev.*, 2014, **44**, 1379–1415.
27 L. Prodi, E. Rampazzo, F. Rastrelli, A. Speghini and N. Zaccheroni, *Chem. Soc. Rev.*, 2015, **44**, 4922–4952.
28 H. Guo, Z. Li, H. Qian, Y. Hu and I. N. Muhammad, *Nanotechnology*, 2010, **21**, 125602.
29 J. Jin, Y.-J. Gu, C. W.-Y. Man, J. Cheng, Z. Xu, Y. Zhang, H. Wang, V. H.-Y. Lee, S. H. Cheng and W.-T. Wong, *ACS Nano*, 2011, **5**, 7838–7847.
30 G. Chen, T. Y. Ohulchanskyy, R. Kumar, H. Ågren and P. N. Prasad, *ACS Nano*, 2010, **4**, 3163–3168.
31 Q. Cheng, J. Sui and W. Cai, *Nanoscale*, 2012, **4**, 779.
32 F. Auzel, *Chem. Rev.*, 2004, **104**, 139–173.
33 F. Auzel, *J. Lumin.*, 1990, **45**, 341–345.
34 H. H. Gorris and O. S. Wolfbeis, *Angew. Chem.*, 2013, **125**, 3668–3686.
35 F. Wang and X. Liu, *Chem. Soc. Rev.*, 2009, **38**, 976–989.
36 X. Chen, D. Peng, Q. Ju and F. Wang, *Chem. Soc. Rev.*, 2014, **44**, 1318–1330.
37 L. Tu, X. Liu, F. Wu and H. Zhang, *Chem. Soc. Rev.*, 2015, **44**, 1331–1345.
38 G. Liu, *Chem. Soc. Rev.*, 2014, **44**, 1635–1652.
39 M. He, P. Huang, C. Zhang, H. Hu, C. Bao, G. Gao, R. He and D. Cui, *Adv. Funct. Mater.*, 2011, **21**, 4470–4477.
40 K. Gavvala, R. K. Koninti, A. Sengupta and P. Hazra, *Phys. Chem. Chem. Phys.*, 2014, **16**, 14953.
41 S. N. Lee, J. Park, M. Lim and T. Joo, *Phys. Chem. Chem. Phys.*, 2014, **16**, 9394.
42 A. Chatterjee and D. Seth, *Photochem. Photobiol. Sci.*, 2013, 369–383.
43 T. Shanmugapriya, R. Vinayakan, K. G. Thomas and P. Ramamurthy, *CrystEngComm*, 2011, **13**, 2340.
44 B. Carlotti, E. Benassi, A. Cesaretti, C. G. Fortuna, A. Spalletti, V. Barone and F. Elisei, *Phys. Chem. Chem. Phys.*, 2015, **17**, 20981–20989.
45 B. Carlotti, A. Cesaretti, C. G. Fortuna, A. Spalletti and F. Elisei, *Phys. Chem. Chem. Phys.*, 2015, **17**, 1877–1882.
46 F. Meng, S. Liu, Y. Wang, C. Tao, P. Xu, W. Guo, L. Shen, X. Zhang and S. Ruan, *J. Mater. Chem.*, 2012, **22**, 22382.
47 L. Wang, R. Yan, Z. Huo, L. Wang, J. Zeng, J. Bao, X. Wang, Q. Peng and Y. Li, *Angew. Chem., Int. Ed.*, 2005, **44**, 6054–6057.
48 L. Wang, X. Xue, H. Chen, D. Zhao and W. Qin, *Chem. Phys. Lett.*, 2010, **485**, 183–186.
49 H. Li and L. Y. Wang, *Chin. Sci. Bull.*, 2013, **58**, 4051–4056.
50 B. Voß, J. Nordmann, A. Uhl, R. Komban and M. Haase, *Nanoscale*, 2013, **5**, 806–812.
51 R. Komban, J. P. Klare, B. Voss, J. J. Nordmann, H.-J. Steinhoff and M. Haase, *Angew. Chem., Int. Ed.*, 2012, **51**, 6506–6510.
52 Q. Tian, K. Tao, W. Li and K. Sun, *J. Phys. Chem. C*, 2011, **115**, 22886–22892.
53 J. Shan and Y. Ju, *Nanotechnology*, 2009, **20**, 275603.
54 J. Shan, M. Uddi, N. Yao and Y. Ju, *Adv. Funct. Mater.*, 2010, **20**, 3530–3537.
55 J. F. Suyver, J. Grimm, K. W. Krämer and H. U. Güdel, *J. Lumin.*, 2005, **114**, 53–59.
56 H. U. G. A. Shalav, B. S. Richards and K. W. Krämer, *Conf. Rec. IEEE Photovoltaic Spec. Conf.*, 2005, **31**, 114–117.
57 F. Vetrone, J. C. Boyer, J. A. Capobianco, A. Speghini and M. Bettinelli, *J. Phys. Chem. B*, 2003, **107**, 1107–1112.
58 S. V. Eliseeva and J.-C. G. Bünzli, *Chem. Soc. Rev.*, 2010, **39**, 189–227.
59 J. M. F. van Dijk, *J. Chem. Phys.*, 1983, **78**, 5317.
60 J. Zhao, Z. Lu, Y. Yin, C. McRae, J. A. Piper, J. M. Dawes, D. Jin and E. M. Goldys, *Nanoscale*, 2013, **5**, 944–952.
61 W. Yu, W. Xu, H. Song and S. Zhang, *Dalton Trans.*, 2014, **43**, 6139–6147.
62 R. Thoma, H. Insley and G. Hebert, *Inorg. Chem.*, 1966, **1005**, 1222–1229.
63 R. E. Thoma, C. F. Weaver, H. A. Friedman, H. Insley, L. A. Harris and H. A. Yakel, *J. Phys. Chem.*, 1961, **65**, 1096–1099.
64 K. W. Krämer, D. Biner, G. Frei, H. U. Güdel, M. P. Hehlen and S. R. Lüthi, *Chem. Mater.*, 2004, **16**, 1244–1251.
65 Y. Song, Q. Tian, R. Zou, Z. Chen, J. Yang and J. Hu, *J. Alloys Compd.*, 2011, **509**, 6539–6544.
66 S. Wilhelm, T. Hirsch, W. M. Patterson, E. Scheucher, T. Mayr and O. S. Wolfbeis, *Theranostics*, 2013, **3**, 239–248.
67 J. F. F. Suyver, J. Grimm, M. K. K. van Veen, D. Biner, K. W. W. Krämer and H. U. U. Güdel, *J. Lumin.*, 2006, **117**, 1–12.
68 S. Schietinger, L. D. S. Menezes and O. Benson, *Nano Lett.*, 2009, **9**, 2477–2481.
69 S. Mishra, G. Ledoux, E. Jeanneau, S. Daniele and M.-F. Joubert, *Dalton Trans.*, 2012, **41**, 1490.

70 M. Wang, G. Abbineni, A. Clevenger, C. Mao and S. Xu, *Nanomed. Nanotechnol. Biol. Med.*, 2011, **7**, 710–729.

71 Y. Chen, W. He, H. Wang, X. Hao, Y. Jiao, J. Lu and S. Yang, *J. Lumin.*, 2012, **132**, 2404–2408.

72 J. Shan, M. Uddi, R. Wei, N. Yao and Y. Ju, *J. Phys. Chem. C*, 2009, **114**, 2452–2461.

73 D. Lu, S. K. Cho, S. Ahn, L. Brun, C. J. Summers and W. Park, *ACS Nano*, 2014, 7780–7792.

74 J. F. Suyver, A. Aebischer, S. García-Revilla, P. Gerner and H. U. Güdel, *Phys. Rev. B: Condens. Matter Mater. Phys.*, 2005, **71**, 1–9.

75 J. D. Kingsley, *Appl. Phys. Lett.*, 1969, **15**, 115.

76 J. L. Sommerdijk, *J. Lumin.*, 1971, **4**, 441–449.

77 A. Pandey, V. K. Rai, R. Dey and K. Kumar, *Mater. Chem. Phys.*, 2013, **139**, 483–488.

78 H. W. Song, H. P. Xia, B. J. Sun, S. Z. Lu, Z. X. Liu and L. X. Yu, *Chin. Phys. Lett.*, 2006, **23**, 474–477.

79 Y. Wang, L. Tu, J. Zhao and Y. Sun, *J. Phys. Chem. C*, 2009, **113**, 7164–7169.

80 F. Liu, E. Ma, D. Chen, Y. Yu and Y. Wang, *J. Phys. Chem. B*, 2006, **110**, 20843–20846.

81 J. Liao, L. Nie, S. Liu, B. Liu and H. Wen, *J. Mater. Sci.*, 2014, **49**, 6081–6086.

82 L. Lei, D. Chen, W. Zhu, J. Xu and Y. Wang, *Chem. – Asian J.*, 2014, **9**, 2765–2770.

83 X. Bai, H. Song, G. Pan, Y. Lei, T. Wang, X. Ren, S. Lu, B. Dong, Q. Dai and L. Fan, *J. Phys. Chem. C*, 2007, **111**, 13611–13617.

84 J. D. Suter, N. Pekas, M. T. Berry and P. S. May, *J. Phys. Chem. C*, 2014, **118**, 13238–13247.

85 S. Wilhelm, M. Kaiser, C. Würth, J. Heiland, C. Carrillo-Carrion, V. Muhr, O. S. Wolfbeis, W. J. Parak, U. Resch-Genger and T. Hirsch, *Nanoscale*, 2015, **7**, 1403–1410.

2.2 Upconversion Luminescence: Unveiling the Single Intermediate Steps of the Cascade like Mechanism Behind

"Upconversion Luminescence Properties of $NaYF_4$:Yb:Er Nanoparticles Codoped with Gd^{3+}"

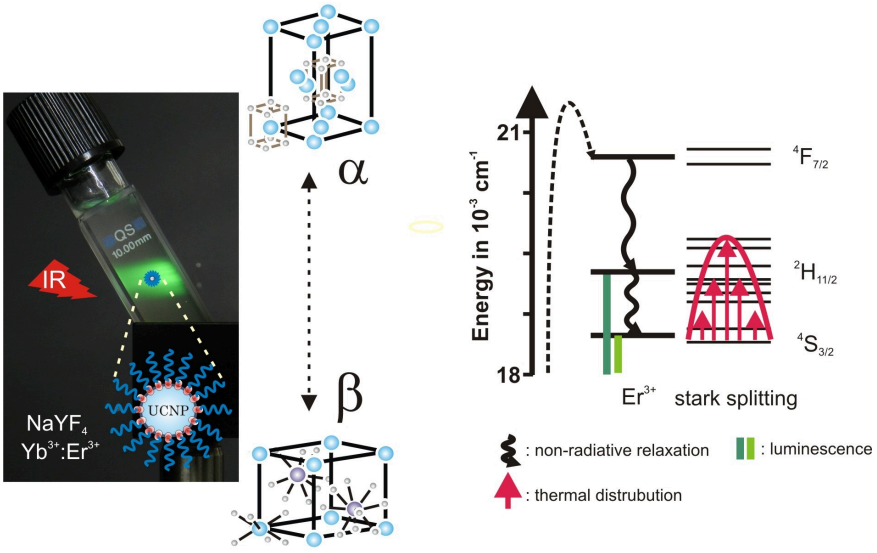

J. Phys. Chem. C, **2015**, *119*, 3363-3373.

Thesis pages: 30 – 40

Author Contribution to the manuscript:

I performed the complete synthesis of all nanoparticles as well as parts of the structural characterization (DLS and Raman measurements). I performed the steady-state (in the range of 4 K and 328 K) and room temperature time-resolved measurements. I completely analyzed and interpreted the photophysical-/structural analytical data and prepared the spectra published. I wrote the manuscript, in close corporation with Michael Kumke.

THE JOURNAL OF PHYSICAL CHEMISTRY C

Article

pubs.acs.org/JPCC

Upconversion Luminescence Properties of $NaYF_4$:Yb:Er Nanoparticles Codoped with Gd^{3+}

Dennis T. Klier and Michael U. Kumke*

Department of Chemistry (Physical Chemistry), University of Potsdam, Karl-Liebknecht-Str. 24-25, 14476 Potsdam, Germany

Supporting Information

ABSTRACT: The temperature-dependent upconversion luminescence of $NaYF_4$:Yb:Er nanoparticles (UCNP) containing different contents of Gd^{3+} as additional dopant was characterized. The UCNP were synthesized in a hydrothermal synthesis and stabilized with citrate in order to transfer them to the water phase. Basic characterization was carried out using TEM and DLS to determine the average size of the UCNP. The XRD technique was used to investigate the crystal lattice of the UCNP. It was found that due to the presence of Gd^{3+}, an alteration of the lattice phase from α to β was induced which was also reflected in the observed upconversion luminescence properties of the UCNP. A detailed analysis of the upconversion luminescence spectra—especially at ultralow temperatures—revealed the different effects of phonon coupling between the host lattice and the sensitizer (Yb^{3+}) as well as the activator (Er^{3+}). Furthermore, the upconversion luminescence intensity reached a maximum between 15 and 250 K depending on Gd^{3+} content. In comparison to the very complex temperature behavior of the upconversion luminescence in the temperature range <273 K, the luminescence intensity ratio of $^2H_{11/2}\rightarrow{}^4I_{15/2}$ to $^4S_{3/2}\rightarrow{}^4I_{15/2}$ (R = G1/G2) in a higher temperature range can be described by an Arrhenius-type equation.

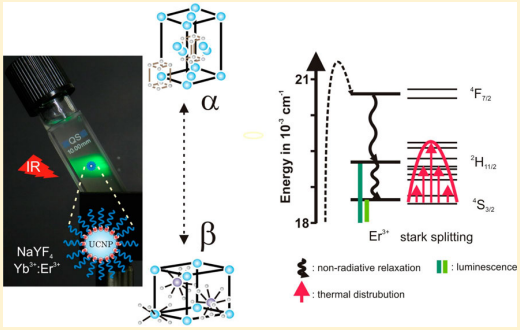

INTRODUCTION

Upconversion (UC) luminescent materials have attracted great interest in recent decades due to their outstanding photophysical properties and the resulting application potentials in various fields such as solid-state laser, solar cells, color displays, or life science applications.[1−9] Upconversion materials based on lanthanide-doped fluorides received a lot of attention owing to their high UC efficiency and photostability. The most efficient UC materials among various fluoride-based UC phosphors are β-phase $NaYF_4$ doped with Yb^{3+} and Er^{3+} or Yb^{3+} and Tm^{3+}.[6,7,10,11] It is well-known that the upconversion luminescence efficiency is highly dependent on dopant concentration, particle size, excitation power density, crystallite phase, and temperature.[8,12,13] The study of their thermal behavior is a prerequisite for the detailed understanding of intramolecular deactivation processes in order to tailor the upconversion luminescence properties and to pave the road for application of multiplexing such as an optical and magnetic imaging using UC materials.[8,14−16]

Currently studies on thermal effects have been focused on diverse glass materials or oxide based materials[13] such as ZnO or Y_2O_3.[17−22] As an example for codoped (Er^{3+}, Yb^{3+}) Y_2O_3 nanocrystals it was reported that the luminescence intensity decreases with increasing temperature from 10 to 300 K.[13,21,23] This effect was explained by the enhancement of nonradiative multiphonon relaxation rates, which reduce the radiative transition probabilities at higher temperatures. Van der Ziel et al. reported that the luminescence intensity of YF_3 nanocrystals first increased and then decreased as temperature was raised up to room temperature. The depopulation of the higher Stark levels of the $^4I_{11/2}$ of Er^{3+} at lower temperatures and multiphonon deexcitation at higher temperatures were proposed as dominant factors that governed the temperature-dependent behavior.[13,21,23]

In the present work, the upconversion luminescence of citrate acid-capped $NaYF_4$:Gd^{3+}:Yb^{3+}:Er^{3+} upconversion nanoparticles (UCNP) with different crystal phases and Y^{3+} to Gd^{3+} ratio was studied at various temperatures from 330 to 4 K. Both the luminescence intensity and ratio of luminescence bands were found to depend on temperature. The crystal phase and thus phonon coupling process play a key role for the upconversion luminescence as well as thermal population rates of the emitting energy levels. The results of this study will show that there is a more complex interplay of different mechanism and effect than one dominant effect that governed the special temperature behavior of the UCNP.

EXPERIMENTAL AND THEORETICAL METHODS

Materials. All rare earth oxides RE_2O_3 (RE: Y, Yb, and Er) were purchased from Chem Pur Feinchemikalien and

Received: October 14, 2014
Revised: January 19, 2015
Published: January 21, 2015

DOI: 10.1021/jp5103548
J. Phys. Chem. C 2015, 119, 3363−3373

The Journal of Physical Chemistry C Article

Table 1. Different $NaY_{1-x}F_4:Yb^{3+}:Er^{3+}:Gd_x^{3+}$ Upconversion Nanoparticle ($UCNP_x$) Used in the Study (in nm)

sample	$UCNP_0$	$UCNP_{15}$	$UCNP_{30}$	$UCNP_{45}$	$UCNP_{60}$	$UCNP_{80}$
Gd^{3+} (x = mol %)	0	15	30	45	60	80
particle size (TEM)	274 ± 13	149 ± 7	110 ± 11	80 ± 10	66 ± 9	46 ± 7
particle size (DLS)	262 ± 36	156 ± 28	128 ± 23	102 ± 21	87 ± 24	68 ± 19
crystallite size (Debye−Scherer)	58 ± 8	42 ± 4	31 ± 7	10 ± 4	9 ± 3	7 ± 2

Forschungsbedarf GmbH. Sodium fluoride (NaF, 99%), gadolinium(III) chloride hexahydrate ($GdCl_3·6H_2O$, 99.9%), sodium nitrate ($NaNO_3$, 99%), and trisodium citrate dehydrate ($Na_3C_6H_5O_5·2H_2O$, 99%) were purchased from Sigma-Aldrich. Nitric acid solution (HNO_3, 65%) was purchased from Carl Roth and suprapure nitric acid from Merck. All chemical reagents used in experiments were directly used without any further purification. For the experiments double distilled water was used.

Synthesis of $NaY_{1-x}F_4:Yb^{3+}:Gd^{3+}:Er^{3+}$ ($UCNP_x$). The UCNP were synthesized according to a previously reported procedure[24−26] in which a hydrothermal method with trisodium citrate as a capping agent was used. The synthesis was designed to keep an overall constant amount of lattice ions (Y^{3+}, Yb^{3+}, Er^{3+}, and Gd^{3+}) in different samples to study the effect of gadolinium concentration. The concentration of the lanthanides (Ln) Er^{3+} and Yb^{3+} was constant for all samples whereas the Y^{3+} was replaced by Gd^{3+} ions (see Table 1). The RE(III) nitrates were prepared from the corresponding oxides in stoichiometric amounts of Y_2O_3 (1.6 mmol), Yb_2O_3 (0.36 mmol), and Er_2O_3 (0.04 mmol) dissolved in nitric acid (5 mL, 10%) according to the literature method.[44] Typically, trisodium citrate (5.8 g) was dissolved into nitric acid (12.4 mL), and then a mixture of $RE(NO_3)_3$, $GdCl_3$ (0 mmol), and sodium nitrate (6.0 g) was added under stirring with an additional 5 mL of water. After 20 min, 10 mL of an aqueous solution of sodium fluoride (0.5 g) was added carefully under stirring. The colloidal solution was heated to 180 °C for 12 h. The UCNPs were separated via centrifugation (6000 rpm for 25 min). For further purification, the UCNPs were washed using a diluted trisodium citrate solution (6.4 g/L) and again separated via centrifugation (6000 rpm for 25 min). The procedure was repeated three times. The as-synthesized UCNPs disperse readily in polar solvents such as in aqueous trisodium citrate solution, forming a clear colloidal solution.

Structural Characterization. X-ray powder diffraction patterns were obtained using a D5005 (Siemens AG, Munich, Germany) in a range of 3°−70°/2θ with divergence aperture, scattering ray aperture, and graphite monochromatized Cu K_α radiation (λ = 0.154 06 nm). The scanning step was 0.02°/2θ with a counting time of 4 s per step. The nanocrystalline domain sizes were calculated using the Debye−Scherrer equation (eq 1):

$$D = \frac{0.89\lambda}{B\cos(\theta)} \tag{1}$$

D is the domain size to be determined, λ is the wavelength of the X-ray, B is the fwhm of the diffraction peak of interest, and θ is the angle of the corresponding diffraction peak.

The size and morphology of as-prepared UCNPs were observed on a JEM 1011 transmission electron microscope (Jeol Ltd., Tokio, Japan) (TEM) using a Wolfram hairpin cathode, an accelerating voltage of 80 kV, and a molybdenum panel. The measurements were recorded using a side-mounted Olympus Mega View G2 (Olympus Germany GmbH, Hamburg, Germany). Particle size characterizations were also carried out with dynamic light scattering (DLS) by using a ZETASIZER Nano ZS (Malvern Instruments Ltd., Herrenberg, Germany) as well. As light source, a He−Ne laser at λ = 633 nm was used.

The samples were prepared as a thin droplet on the substrate and were further investigated by Raman spectroscopy. Here, a Raman microscope (ALPHA 300 RA, WITec, Ulm, Germany) coupled with an intensified CCD camera (DU401A-BR-DD-352, WITec, Ulm, Germany) was used.

The elemental composition of the as-prepared UCNP was confirmed by ICP-OES (for more details see Supporting Information Table 1).

Room Temperature Steady-State and Time-Resolved Upconversion Luminescence. Room temperature steady-state and time-resolved upconversion emission spectra were obtained using a wavelength tunable pulsed Nd:YAG/OPO laser system (laser: Quanta Ray, Spectra-Physics, Mountain View, CA; OPO: GWU-Lasertechnik Vertriebsges. mbH, Erftstadt, Germany) operating at 20 Hz as excitation light source (at 26 mJ/130 mW) and recorded using an intensified CCD-camera (iStar DH720-18H-13, Andor Technology, Belfast, Great Britain) coupled to a spectrograph (MS257 Model 77700A, Oriel Instruments) equipped with a 300 lines/mm grating. The "boxcar" technique was applied for these sets of measurements. The initial gate delay was set to Δt = 500 ns, and the gate width was adjusted between δt = 10 and 100 μs. The luminescence decay kinetics were evaluated by eq 2:

$$I(t) = A + B_1\exp(-k_1 t) + B_2\exp(-k_2 t) \tag{2}$$

From the coefficients B_1 and B_2 the relative fractions α_1 and α_2 were calculated according to eq 3:

$$\alpha_1 = \frac{B_1\tau_1}{B_1\tau_1 + B_2\tau_2} \tag{3}$$

For the temperature range of 303 K < T < 328 K the samples were measured as colloidal solutions in PMMA (poly(methyl methacrylate)) cuvettes sealed with Parafilm. Prior to measurement, the samples were heated in a water bath to the chosen temperature and measured in a temperature-controlled sample holder.

Low-Temperature Upconversion Measurements. The temperature-dependent steady-state upconversion luminescence measurements were recorded using a continuous wave, fiber coupled laser diode working at 1000 mW (SHE-SP-975-160-FS-SMA, Laser 2000 GmbH, Wessling, Germany), coupled to a shutter in order to avoid heating up the sample. In order to perform low-temperature luminescence measurements in a range of 4 K to room temperature, the UCNP colloidal solutions or powders were sealed inside glass tubes and placed on a copper sample holder in a vacuum chamber attached to the cold plate of a closed cycle liquid helium cryostat. The cryostat system consist of a helium compressor unit (Sumitomo Heavy Industries Ltd., Markt Indersdorf, Germany), a vacuum pump (Leybold vacuum Turbolab 80, Oerlikon, Köln,

DOI: 10.1021/jp5103548
J. Phys. Chem. C 2015, 119, 3363−3373

Germany) for the sample chamber, and a temperature controller (331 temperature controller, Lake Shore, Westerville, OH). The excitation light was focused on the samples at an angle of 90°. The upconversion luminescence emission was recorded using a lens system mounted in front of a fiber connected spectrograph (Shamrock SR-303i, Andor Technology, Belfast, Great Britain) equipped with an intensified CCD camera (iStar DH 720 18 V 73, Andor Technology, Belfast, Great Britain).

RESULTS AND DISCUSSION

Structural Investigations. $UCNP_x$ based on the $NaYF_4$ host lattice were synthesized with varying content of Gd^{3+} (x = 0−80 mol %, see Table 1 and Supporting Information Table 1 for elemental analysis). The samples were first examined by X-ray powder diffraction. For the $NaYF_4$ host lattice two different thermodynamically stable phases, the cubic (isotropic) α-phase and the hexagonal (anisotropic) β-phase, are known.[27] In Figure 1 diffraction patterns of $UCNP_x$ with x = 0, 30, and 80

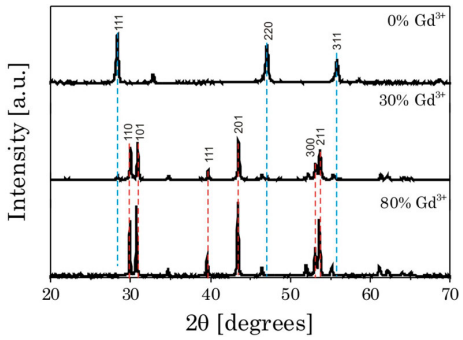

Figure 1. X-ray diffraction patterns of $UCNP_x$ (x = 0, 30, and 80) with the Millerschen Indices of the corresponding lattice plane are shown.

are compared. In the absence of Gd^{3+} ions the X-ray diffractions pattern can be assigned to a pure cubic α-phase, as expected for this type of UCNP synthesized under mild conditions.[24−26] The gradually decrease of the diffraction peak intensities of the cubic α-phase is correlated with an increasing Gd^{3+} dopand concentration and the rise of the diffraction peak intensity of the hexagonal phase, whereby a gradual phase transition from the cubic to the hexagonal phase is obvious. The pure β-phase was obtained at Gd^{3+} concentration of 80 mol %, which is consistent with the studies of Song et al. (see Figure 1).[28] Remarkably, the cubic to hexagonal β-phase transition is complete after heating at 160−200 °C for 12 h, whereas a complete phase transition without any Gd^{3+} is typically achieved at distinctly higher temperatures (T > 300 °C) or longer reactions times of 16 h or more.[24−26]

The lattices of $NaGdF_4$ and $NaYF_4$ belong to the same space group ($P6_3/m$) and show nearly similar unit cell parameters.[10,27] Therefore, the observed transition between cubic and hexagonal phase for the $UCNP_x$ materials could be a consequence of the good similarity of the hexagonal phases of $NaGdF_4$ and $NaYF_4$ which is also indicated by the diffraction patterns of both ($NaGdF_4$ (ICDD no: 28-0699) and $NaYF_4$ (ICDD no: 28-1192)).[10,27] The crystallite size of the as-prepared UCNPs was calculated using the Debye−Scherrer equation (eq 1). It is obvious (see also Table 1) that the crystallite size decreases with increasing amount of Gd^{3+} ion dopand concentration and is nearly constant at Gd^{3+} concentrations of at least 45 mol %. Based on XRD measurements only the crystallite size is determined, which can be significantly different from the particle size determined from other techniques such as TEM and DLS (vide infra and see Table 1). The XRD data for the size dependence on the Gd^{3+} content are in good agreement with the general trend observed with DLS and TEM (see Table 1). The large difference is also an indication that the particles are containing more than one crystalline domain (or some amorphous parts, which is not supported by the good luminescence upconversion properties of the particles; vide supra).

The particle size and morphology of $UCNP_x$ at different Gd^{3+} dopand concentrations were further studied using TEM and DLS. The TEM images of the different $UCNP_x$ showed that the particles were irregular spherical in shape (Supporting Information Figure 1).[28] In order to determine the average particle size from TEM images approximately 200 particles were included in the statistical analysis which showed that with increasing Gd^{3+} dopand concentration the diameter of the nanoparticles gradually decreased (see Table 1). In comparison to the shown results (similar to Liu et al.), Song et al. observed no effect of Gd^{3+} ion doping concentration on particle size evolution, which is related to different solvent mixtures.[10,28]

In addition, DLS was used as a complementary method for particle size determination. The results of the DLS measurements are also shown in Table 1. Corroborating the results of the TEM images, DLS showed as well a decreasing particle size evolution with increasing Gd^{3+} concentration. In comparison to the TEM investigations the particle size obtained from the DLS measurements are slightly larger. In DLS the hydrodynamic radius is determined which includes also contribution of a solvent shell. The latter is not observed in the TEM images, which subsequently yield slightly smaller particle sizes when compared to DLS.

In the synthesis of the $UCNP_x$ the particle size control is defined by the combination of the capping agent (here sodium citrate) and by the Gd^{3+} concentration. The significant particle size reduction (according to the TEM image analysis about factor of 6 between 0 and 80 mol % Gd^{3+}) can be attributed to effects of the Gd^{3+} ions on the effective surface charge, which is a key factor for the crystal growth rate. This explanation is supported by DFT calculations which showed that the electron charge density of the crystal surface increases when small Ln^{3+} ions (e.g., Nd^{3+}, Gd^{3+}, and Sm^{3+} ions) substitute the Y^{3+} ions in the crystal lattice.[10]

Raman spectra (see Figure 2) show the vibrational modes of $UCNP_x$ nanoparticles displaying five obvious Raman peaks at ν = 249.6, 422.1, 536.8, 739.5, and 1062 cm^{-1}. The most intense vibrational bands are found at low phonon energies between 200 and 500 cm^{-1}, which is consistent with reported low phonon energies for this kind of material.[10,29−31] The gradually decrease of the first Raman peak (249.6 cm^{-1}) intensity and increase of the second Raman peak (422.1 cm^{-1}) are correlated with an increasing amount of Gd^{3+} dopand.

All vibrational bands at wavenumbers larger than 500 cm^{-1} are attributed to the vibrations from the organic capping agent citrate except for the band located at 1062 cm^{-1}. The presence of citrate on the surface of the UCNP is indicated by strong COOH out-of-plane deformation modes in the 786−908 cm^{-1} region and the C−O stretching modes in the 998−1112 cm^{-1} region.

DOI: 10.1021/jp5103548
J. Phys. Chem. C 2015, 119, 3363−3373

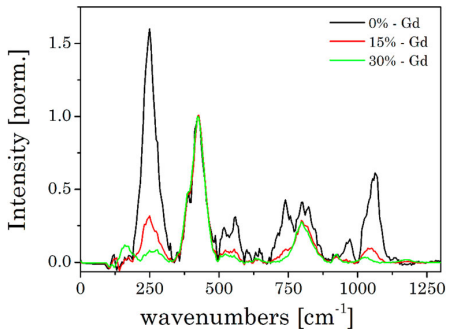

Figure 2. Raman spectra of different $UCNP_x$ (x = 0, 15, and 30 mol %, λ_{ex} = 532 nm).

Upconversion Luminescence Spectroscopy Studies. In Figure 3 the luminescence spectra of the $UCNP_x$ containing different mol % Gd^{3+} are shown.

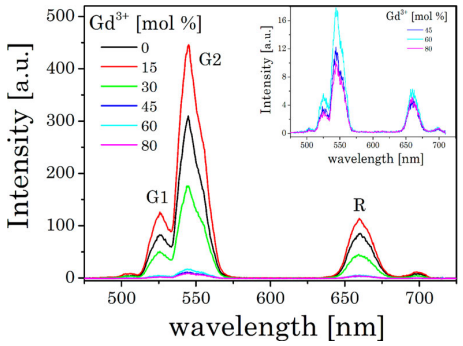

Figure 3. Upconversion emission spectra of $UCNP_x$ showing the Er^{3+} luminescence bands G1, G2, and R for increasing Gd^{3+} content (λ_{ex} = 976 nm).

The spectra were recorded in water with λ_{ex} = 976 nm and are the result of energy upconversion processes (see Scheme 1).[32] The three most intense emission bands can be observed in the green spectral region centered at λ_{em} = 525 nm ($^2H_{11/2} \rightarrow {}^4I_{15/2}$ transition, G1), 545 nm ($^4S_{3/2} \rightarrow {}^4I_{15/2}$ transition, G2), and the red spectral region centered at 660 nm ($^4F_{9/2} \rightarrow {}^4I_{15/2}$ transition, R) accompanied by the albeit very weak blue band centered at 505 nm ($^4F_{7/2} \rightarrow {}^4I_{15/2}$ transition) and a second weak red band at 700 nm as a result of the $^4F_{7/2} \rightarrow {}^4I_{13/2}$ transition.[11,13,33−35] The observed fine structure (Stark splitting) is induced by changes of the crystal field splitting due to small differences in the coordination environment.[33,36,37]

The upconversion emission spectra shown in Figure 3 reveal significant differences between the $UCNP_x$ investigated. For the absolute intensities of the upconversion emission, a strong dependence on the Gd^{3+} concentration was found.[38] The emission intensity of the $UCNP_x$ increased with an increase in the Gd^{3+} concentration up to 15 mol % and then showed a gradual decrease upon further increase of the Gd^{3+} content.[28] Since the $^6P_{7/2}$ level, which represents the next electronic state above the ground state of Gd^{3+}, is spectroscopically found in the ultraviolet region and is therefore much higher in energy than the excited state levels of Er^{3+} and Yb^{3+}, any luminescence quenching by energy transfer between these ions can be ruled out. The effect is more probably related to alterations of the

Scheme 1. Schematic Energy Level Diagram of the Upconversion Mechanism of a Er^{3+} and Yb^{3+} Dopand Ion System Following an Excitation with 976 nm[a]

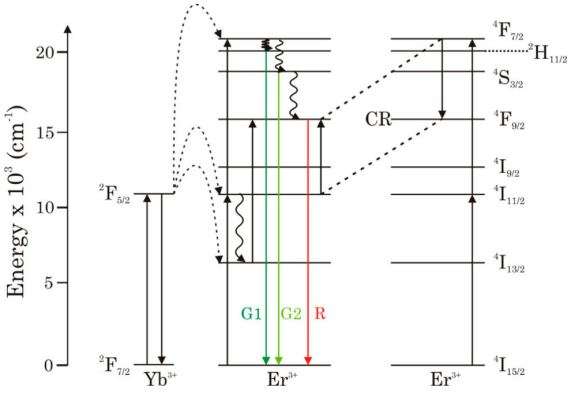

[a]The full lines pointing upwards represent energy absorption, the dotted lines represent energy transfer, the waved lines represent nonradiative relaxation processes, and the colored full lines pointing downwards represent the visible emission. The cross-relaxation between different excited Er^{3+} ions is represented by "CR".

crystal lattice induced by the addition of Gd^{3+} ions: (i) change from α- to β-phase of the nanoparticle lattice and (ii) variation of the energy gap between Stark levels of Yb^{3+} ($^2F_{5/2}$) and Er^{3+} ($^4I_{11/2}$), respectively, subsequently leading to a more effective upconversion. Variations in the relative position of the Stark levels of lanthanides in different host lattice are well-known.[37,39] For higher Gd^{3+} contents (x > 15) as a third parameter the particle size affecting the luminescence yield of the nanoparticles comes into play. Smaller nanoparticles exhibit a higher surface to volume ratio (SA/Vol), leading to a relative higher concentration of dopands ions located at the surface nearby region or on surface. Thus, the observed upconversion luminescence is quenched by enhancement of nonradiative relaxations processes in the surface region.

At room temperature no change in the Yb^{3+}-related absorption is found. Here, the splitting of the involved Stark levels of the $^2F_{7/2}$ state is small, and thermal equilibration is reached at room temperature masking any possible influence of the Gd^{3+} content. Here, high-resolution ultralow-temperature experiments are required to get a deeper insight (vide infra).

In Figure 4 typical luminescence decay kinetics of the $UCNP_x$ for the green (λ_{em} = 545 nm, G2) and red (λ_{em} = 660 nm, R) emission are shown. From the raw data it is evident that the underlying decay kinetics are complex because erbium ions located in the bulk phase of the particles and on the surface are influenced by their environment to a different extent (e.g., quenching by water molecules). Hence, a biexponential decay law was chosen for the data analysis (see eq 2).

Moreover, in the analysis it was assumed that due to the decreasing size of the $UCNP_x$ with increasing Gd^{3+} content only the relative fraction of bulk-to-surface luminescence is changing. Consequently, the experimental data were evaluated in a global analysis with two common decay times τ_1 and τ_2 only leaving the coefficients B_1 and B_2 as individual fit parameters. The relative fractions α_1 and α_2 were calculated according to eq 3 (see Table 2). From Figure 4 and Table 2 it is evident that above a certain Gd^{3+} content the luminescence kinetics distinctly changed. $UCNP_x$ with x = 0−30 showed a

DOI: 10.1021/jp5103548
J. Phys. Chem. C 2015, 119, 3363−3373

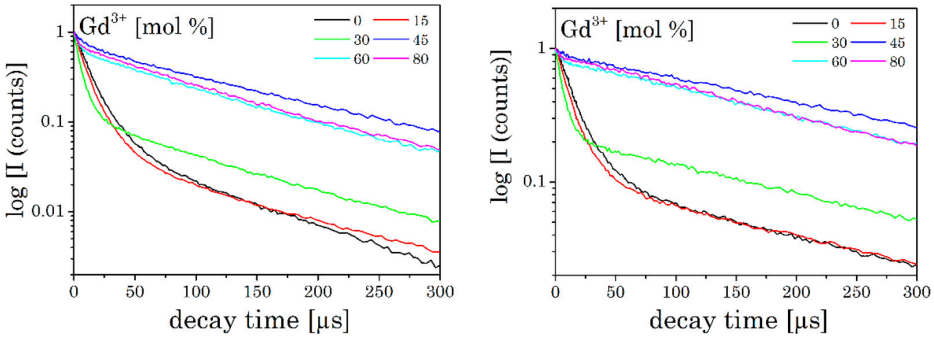

Figure 4. Luminescence decay kinetics of $UCNP_x$ for the green emission G2 (λ_{em} = 545 nm, left) and the red emission R (λ_{em} = 660 nm, right) (λ_{ex} = 976 nm, initial delay δt = 500 ns).

Table 2. Luminescence Decay Parameters of $UCNP_x$

	sample	$UCNP_0$	$UCNP_{15}$	$UCNP_{30}$	$UCNP_{45}$	$UCNP_{60}$	$UCNP_{80}$
G2				fraction (in %)			
	α_1 (τ_1 = 10 μs)	58	63	42	4	5	4
	α_2 (τ_2 = 113 μs)	42	37	58	96	95	96
R				fraction (in %)			
	α_1 (τ_1 = 11 μs)	30	30	30	2	3	3
	α_2 (τ_2 = 209 μs)	70	70	70	98	97	97

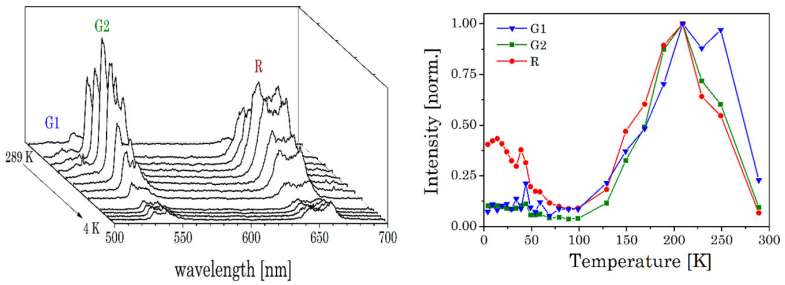

Figure 5. Left: temperature-dependent upconversion emission of $UCNP_{80}$ (λ_{ex} = 976 nm). Inset or Right: temperature-dependent upconversion emission (integrated intensities and normalized) of $UCNP_x$ nanoparticles (80 mol % Gd^{3+}).

larger contribution from a short luminescence decay with a corresponding luminescence decay time τ_1 of about 10 μs. For $UCNP_x$ with x = 45−80 contributions from this short decay component were less than 5%. This was found for the decay kinetics of the G2 and R luminescence of erbium (see Table 2). For R luminescence, the second decay time $\tau_2 \sim 200$ μs was determined, which is distinctly longer than the time decay τ_2 of ~100 μs found for the corresponding emission decay of G2.

The observed short luminescence decay time τ_1 may be related to erbium ions located near the surface of the nanoparticles, while long luminescence decay time τ_2 could be attributed to erbium ions located in the bulk phase of the nanoparticles. In that case the short luminescence decay time τ_1 could be a consequence of an efficient quenching process due to water molecules interacting with the surface of the $UCNP_x$. It can be hypothesized that (i) with decreasing size of the nanoparticle the average number of water molecules possibly interacting with the surface of the nanoparticle is also decreasing, which would subsequently reduce the relative fraction of τ_1, or (ii) the quenching becomes extremely efficient ("quasi-static") and the major part of the surface-located erbium ions is completely quenched, leaving only a small portion to be present in the overall luminescence decay.

The τ_2 of the red emission R was found to be longer than τ_2 of the corresponding green emission G2, which is related to the differences in the rate constants of deactivation processes of the $^4S_{3/2}$ and $^4F_{9/2}$ level in erbium (see Scheme 1).

Low-Temperature Upconversion Luminescence Studies. In Figure 5 emission spectra as well as the integrated luminescence band intensities of $UCNP_{80}$ (λ_{ex} = 976 nm) for the temperature range of 4 K < T < 209 K are shown, which are representative for the observed temperature dependence of all $UCNP_x$ investigated. The following trends were observed for the different luminescence bands of Er^{3+}: (i) The luminescence intensity of the $^2H_{11/2} \rightarrow {}^4I_{15/2}$ transition (G1) gradually decreased with decreasing temperature and disappeared completely at temperatures below 120 K. (ii) In contrast to the G1 emission band, the intensity of the G2- and R-related emission bands initially increased with decreasing temperature. However, after passing T = 210 K, the emission intensity decreased again upon further lowering the temperature (see Figure 5). When temperature drops below 100 K, an additional increase in upconversion luminescence intensity was found for band R, whereas in the case of band G2 the intensity did not change significantly.

DOI: 10.1021/jp5103548
J. Phys. Chem. C 2015, 119, 3363−3373

The difference in the temperature dependence of the G1 and G2 emission bands is connected to the population pathways of the related energy levels $^2H_{11/2}$ and $^4S_{3/2}$, respectively. In Scheme 2 a detailed view of the respective Stark levels of $^2H_{11/2}$ and $^4S_{3/2}$ is shown. The Stark levels are calculated from the excitation and emission spectra of the UCNP$_x$ under investigation. The population of the green emitting levels G1 and G2 ($^2H_{11/2}$ and $^4S_{3/2}$) usually occurs by successive energy transfer processes from the excited $^2F_{5/2}$ state of Yb^{3+} ions to the Er^{3+} ions exciting it first to the $^4I_{11/2}$ state and in a second step to the $^4F_{7/2}$ excited state. Followed by a nonradiative relaxation process the Er^{3+} ion deactivates to the $^2H_{11/2}$ and—due to the moderate energy gap between $^2H_{11/2}$ and $^4S_{3/2}$ states (about 700 cm^{-1})—the Er^{3+} ions can relax fast to the $^4S_{3/2}$ state. Finally, the $^2H_{11/2}$ level is thermally repopulated via thermal agitation (see Scheme 2), resulting in the observed two Er^{3+} emission bands G1 and G2 as shown in Figure 3 (see also Scheme 1).[13,33,34,39]

Scheme 2. Close-Up of Energy Levels Related to G1 and G2 Emission in Erbium

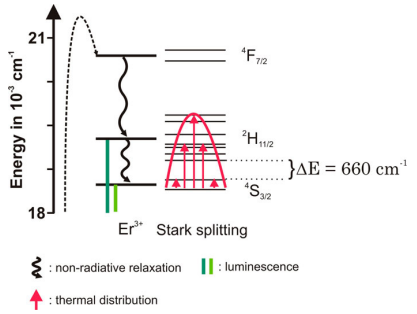

The thermal equilibration of the two levels is fast; hence, the observed intensity ration of G1 and G2 will be dependent on the temperature. Alternatively, the ions can relax nonradiative to the $^4F_{9/2}$ level leading to red emission (centered at 660 nm). Further, the $^4F_{9/2}$ level can be populated after nonradiative relaxation from the $^4I_{11/2}$ to $^4I_{13/2}$ level followed by an energy transfer from the sensitizer Yb^{3+} to the Er^{3+}, leading also to the red emission R. Typically cross-relaxation processes between two excited Er^{3+} ions can be neglected in the UCNP$_x$ investigated because of the low Er^{3+} content used.[35,40]

In Figure 6 the temperature-dependent upconversion luminescence intensities of UCNP$_x$ are compared. In general, a similar temperature dependence was found for all UCNP$_x$ investigated. Upon lowering the temperature, the intensities of the G2 and R bands increased and then dropped again after passing a certain temperature. However, the temperature of maximum luminescence intensity was found to be specific for the Gd^{3+} content of the UCNP$_x$.

For the temperature dependence of the R band it was found that for concentration of Gd^{3+} above 60 mol % luminescence intensity increased again at very low temperatures (see Figure 6). The observed differences of the temperature dependency are due to the different population mechanisms of band R and G1. Within the different cascades of energy transfers from the Yb^{3+} to the Er^{3+} and the nonradiative relaxation steps (see Scheme 1) phonon coupling is very important in order to bridge little energy difference between the sensitizer and the activator involved. From the XRD and Raman measurements (see Figures 1 and 2) a change in the host lattice properties (transition between α- and β-phase) with increasing Gd^{3+} content was concluded.

In a control experiment UCNP$_0$ was tempered at different temperatures to induce the phase transfer from α-phase to β-phase.[42,44] In Figure 7 (left) the corresponding XRD data are presented. Comparison with reference data and with Figure 1 shows that in the material a phase transfer from α-phase (300 °C) to β-phase (400 °C) and back to α-phase (700 °C) is induced due to different thermodynamic stabilities.[40] The corresponding integrated luminescence intensities of these three tempered materials are shown in Figure 7 (right) for the emission band G2. The maximum of upconversion luminescence shifts to higher temperatures with increasing amount of β-phase (sample tempered at 400 °C) and then back to lower temperatures because of the back transfer from β-phase to α-phase (sample tempered at 700 °C). This experiment underlines the importance of the host lattice for the temperature dependence of the luminescence properties of UCNP, and it further shows that with the adjustment of the Gd^{3+} content temperature sensitivity range of the UCNP can be tailored.

A similar temperature dependence has been reported by Zhang et al. for $NaYF_4$:Yb^{3+}:Er^{3+} nanoparticles.[14,41] They found that the temperature at which the maximum luminescence intensity was observed was dependent on the size of the nanoparticles. On the other hand, for bulk $NaYF_4$:Yb^{3+}:Er^{3+}

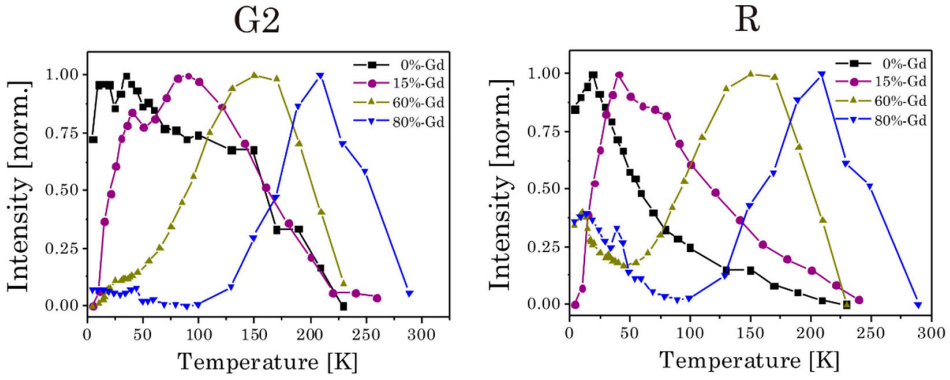

Figure 6. Normalized upconversion luminescence intensities of UCNP$_x$ as a function of temperature for G2 (left) and R (right) (τ_{ex} = 976 nm).

DOI: 10.1021/jp5103548
J. Phys. Chem. C 2015, 119, 3363−3373

The Journal of Physical Chemistry C Article

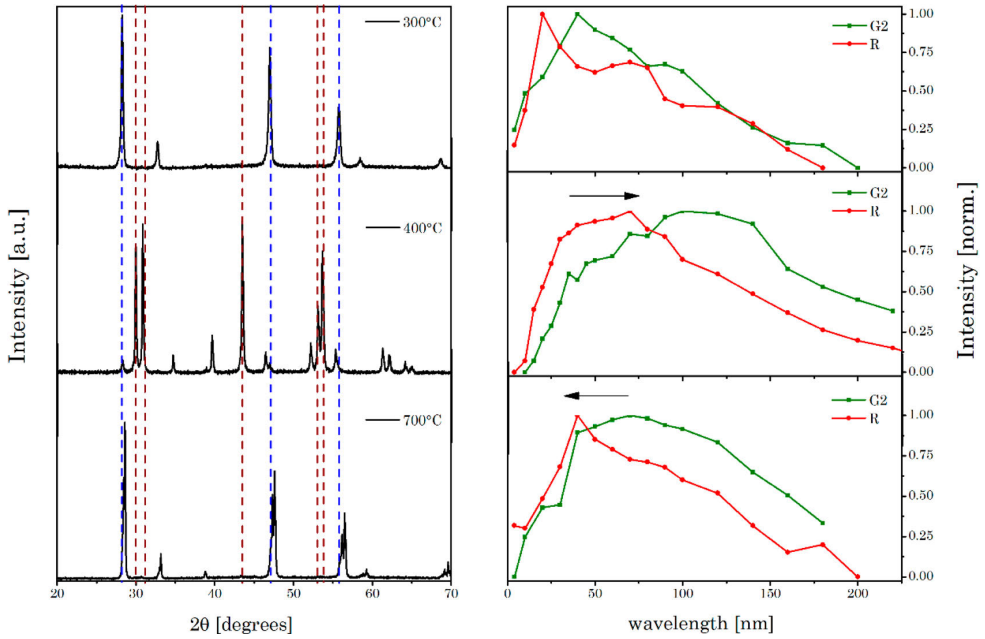

Figure 7. $UCNP_0$ at three different temperatures are shown. Left: X-ray diffraction patterns. The blue dotted lines represents the α-phase and the red one the β-phase. Right: normalized upconversion luminescence intensity of band G2 and R after different thermal treatments as a function of temperature.

powders a different temperature effect was observed. For bulk powders of Yb^{3+}:Er^{3+} codoped $NaYF_4$, barium−thorium fluoride, or chalcogenide glasses after an initial increase the luminescence intensity is reaching a plateau and stays constant when further lowering the temperature.[13,33] The difference in the temperature dependence of bulk materials and nanoparticles is related to the extent of electron−phonon coupling, which is stronger in nanoparticles.[13,18]

In Yb^{3+} the two lowest energy crystal field components of the $^2F_{5/2}$ multiplet are $^2F_{5/2}|0\rangle$ (~10 281 cm^{-1}) and $^2F_{5/2}|1\rangle$ (~10 242 cm^{-1}).[39] The temperature-dependent emission is determined by population as well as the excitation cross section of the $^2F_{5/2}|0\rangle$ and $^2F_{5/2}|1\rangle$ levels of Yb^{3+}, since both parameters are temperature dependent. For thermal equilibrium the Boltzmann coefficient N_1/N_0 = 0.84 at room temperature is very high, which is a consequence of the very low energy difference of 39 cm^{-1} between the two Stark levels.

In Figure 8 the excitation spectra of $UCNP_{15}$ at room temperature and at 80 K are shown. Because of thermal equilibration only one broad emission band at λ_{ex} = 976 nm is found at room temperature. However, at T = 80 K the broad emission is split into two emission bands, and the energy difference of 39 cm^{-1} fits very to the energy difference of the Stark levels $^2F_{5/2}|0\rangle$ and $^2F_{5/2}|1\rangle$ of Yb^{3+}. Figure 8 further shows that the intensity of the $^2F_{5/2}|0\rangle$-related peak is approximately 10 times higher compared to the $^2F_{5/2}|1\rangle$ related emission. Since the excitation spectra were constructed based on the Er^{3+} emission intensity under variation of the excitation wavelengths, the intensity distribution could be due to differences (i) in the transfer efficiency from Yb^{3+} to Er^{3+} and/or (ii) in the absorption cross section of the Yb^{3+} Stark levels involved. It is known that the excitation cross section of the $^2F_{5/2}|0\rangle$ Stark level is larger, but on the other hand with respect to energy matching between Yb^{3+} and Er^{3+} the transfer from the $^2F_{5/2}|1\rangle$

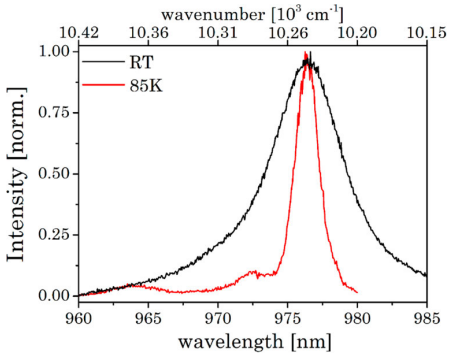

Figure 8. Excitation emission spectra of $UCNP_{15}$ at T = 295 K and T = 85 K (λ_{em} = 540 nm).

Stark level is more efficient. A nearly perfect resonance is given for level $^2F_{5/2}|1\rangle$ of Yb^{3+} and $^4I_{11/2}|0\rangle$ of Er^{3+}. For the overall process of generating upconversion luminescence thermal population of the $^2F_{5/2}|1\rangle$ Stark level is important. Consequently, the temperature-dependent luminescence is defined by the Boltzmann fraction in the $^2F_{5/2}|0\rangle$ state and the excitation cross section of Yb^{3+}, which is also temperature dependent. Therefore, the upconversion luminescence intensity I_i can be written as[13,33,46,47]

$$I_i = N_{i,\infty} \exp\left[-\frac{p_i \Delta E}{k_B T}\right][\sigma_{Yb}(T)]^{p_i} \quad (4)$$

$N_{i,\infty}$ is the population of the emission band in the high energy limit, and ΔE denotes the energy difference between the $^2F_{5/2}|0\rangle$ and $^2F_{5/2}|1\rangle$ states of Yb^{3+}. Further, k_B is the Boltzmann constant and p_i is the number of photons required for the excitation of band i. Finally $\sigma_{Yb}(T)$ describes the temperature

DOI: 10.1021/jp5103548
J. Phys. Chem. C 2015, 119, 3363−3373

dependence of the (Lorentzian) excitation cross section of Yb^{3+} and can be written as

$$\sigma_{Yb}(T) \propto \exp\left(-\frac{k_B T}{E_q}\right) \quad (5)$$

The fitting parameter E_q is an empirical quenching energy. This equation is restricted to resonant energy transfers from $^2F_{5/2}|1\rangle$ of Yb^{3+} to $^4I_{11/2}|0\rangle$ of Er^{3+}. Hence, no phonon-mediated energy-transfer step is considered in this approximation.

As an example in Figure 9 the analysis of the experimental data of $UCNP_{60}$ using eq 4 for the luminescence band G2 as a function of temperature is shown. The low-temperature regime was reasonable fit be eq 4. For higher temperatures, larger deviations between the model and the experimental data were found. This indicates that at low temperatures the influence of the Stark splitting, the energy match between activator and sensitizer, and the absorption cross section are the determining parameters in the upconversion process, but at higher temperature another factor has to be considered. Here, the electron−phonon coupling needs to be considered.

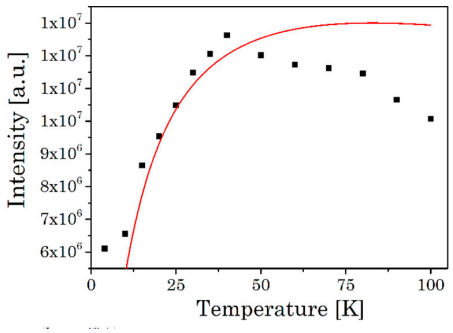

Figure 9. Integrated upconversion luminescence intensities (dots) of $UCNP_{60}$ for G2 as a function of temperature. The solid line represents the data analysis of the experimental data according to eq 4.

Temperature-Dependent Upconversion Luminescence for $T > 273$ K. Not only the Yb^{3+} and subsequent energy transfer related processes are temperature dependent, but also the population of different energy levels of Er^{3+} are influenced by the temperature (e.g., the $^2H_{11/2}$ and the $^4S_{3/2}$ level from which the G1 and G2 luminescence originates).[41]

For $T > 273$ K the correlation of the luminescence intensity ratio (R = G1/G2) and the temperature T can be described by an Arrhenius-type equation.[16,45]

$$R = \frac{I_{G1}}{I_{G2}} = A \exp\left(-\frac{\Delta E_{G1/G2}}{k_B T}\right) \quad (6)$$

R is the ratio of integrated luminescence intensity originating from bands G1 and G2 which are separated by the energy gap $\Delta E_{G1/G2}$, k_B is the Boltzmann constant, T is the temperature, and A is a constant which depends on the spontaneous emission rate and the energies of the emitting states in the host material.

For the higher temperature range ($T > 273$ K) the data were evaluated according to eq 6. From Figure 10 (left) it can be seen that R is changing with temperature because the relative intensity of the G1-related luminescence is increasing. This is a consequence of the thermally induced redistribution in population between the energy levels $^2H_{11/2}$ and $^4S_{3/2}$ (see Scheme 1). Especially for higher temperatures ($T > 273$ K) a distinct change with temperature was found, which is connected to the fact that the energy gap $\Delta E_{G1/G2}$ is on the order of a few hundred wavenumbers depending on the host lattice.

For $UCNP_0$ an energy gap $\Delta E_{G1/G2} = 812 \pm 8$ cm^{-1} was determined, which correlates very well with the data of Carnall et al., who studied the energy level assignments for Er^{3+} in several host lattices.[39,49] Figure 10 (right) shows the calculated energy gaps $\Delta E_{G1/G2}$ of the $UCNP_x$. A distinct impact of the Gd^{3+} concentration on the $\Delta E_{G1/G2}$ in the different $UCNP_x$ was found. $\Delta E_{G1/G2}$ decreases with increasing Gd^{3+} concentration and finally reached a minimum value of 680 cm^{-1} for Gd^{3+} concentration of 45 mol %. Higher concentration of Gd^{3+} ions showed no further decrease of $\Delta E_{G1/G2}$. These results further corroborate the results of the XRD and luminescence decay time measurements, in which the strong influence of the Gd^{3+} on the host lattice and subsequently on the luminescence properties was observed, too (vide supra). Because of the Gd^{3+} ions, the Stark splitting of the $^4S_{3/2}$ level is increased, resulting in a smaller energy gap $\Delta E_{G1/G2}$ because the lowest Stark level of $^2H_{11/2}$ and the highest Stark level of $^4S_{3/2}$ moved closer together. Associated with the decreasing$\Delta E_{G1/G2}$ is an enhanced population of the energy level $^2H_{11/2}$ due to thermal equilibration (Boltzmann distribution), leading to an increasing luminescence intensity of G1 relative to G2. A selection of the upconversion emission ratios of band G1 and G2 in

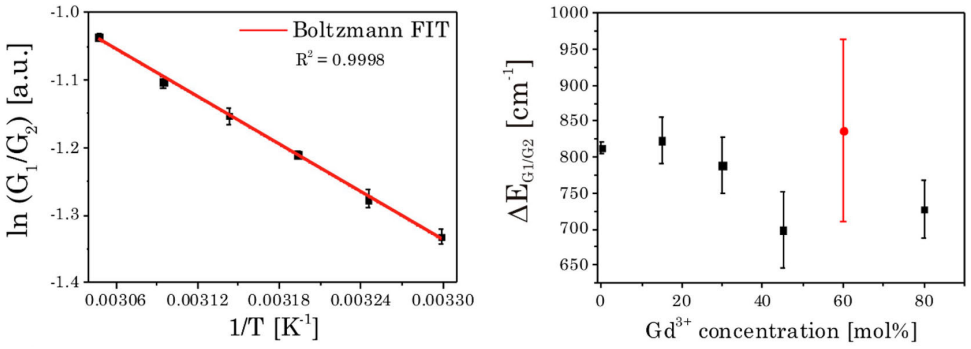

Figure 10. Left: analysis of $UCNP_0$ sample data temperature dependence of the logarithm of the integrated emission intensity ratio of bands G1 and G2. Right: energy gap $\Delta E_{G1/G2}$ as a function of Gd^{3+} concentration.

DOI: 10.1021/jp5103548
J. Phys. Chem. C 2015, 119, 3363−3373

dependence of Gd^{3+} concentration is shown in Table 3. The increasing ratio $R_{G1/G2}$ with the gradually increasing amount of

Table 3. Ratio $R_{G1/G2}$ of the Upconversion Luminescence of G1 and G2 for Different $UCNP_x$ at Different Temperatures

temperature [K]	$UCNP_0$	$UCNP_{30}$	$UCNP_{80}$
120			0.09
160	0.07	0.12	0.14
209	0.11	0.17	0.22
303	0.26	0.27	0.37
313	0.30	0.31	0.38
323	0.33	0.35	0.46
328	0.35	0.37	0.49

Gd^{3+} in the host lattice is caused by the decreasing energy gap $\Delta E_{G1/G2}$ showing a very good correlation to the initial results.

Based on eq 6, the absolute S_a and relative sensor sensitivity S_r can be obtained.[49−52]

$$S_a \sim \left|\frac{\partial R}{\partial T}\right| \sim R\frac{\Delta E_{G1/G2}}{kT^2} \tag{7}$$

$$S_r \sim 100\%\left|\frac{1}{R}\frac{\partial R}{\partial T}\right| \sim 100\%\frac{\Delta E_{G1/G2}}{kT^2} \tag{8}$$

The temperature-sensitive calculated values of S_a and S_r are shown in Figure 11. The maximum value of S_r of 1.35% K^{-1}

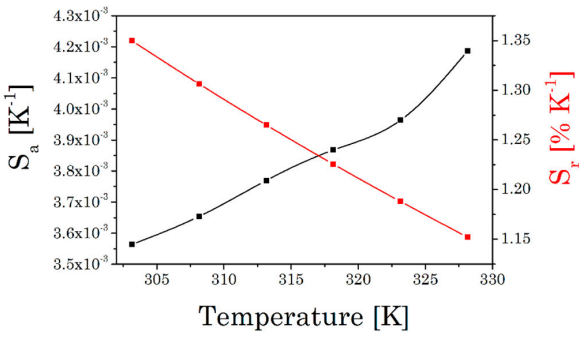

Figure 11. Absolute (black line) and relative (red line) sensitivity of the temperature sensor based on R of the upconversion luminescence of UCNPs.

was found at 303 K, which is slidely higher (among the highest S_r which can be found in the literature) to typical values of $NaYF_4$:Yb^{3+}:Er^{3+} or other new host lattices of upconverters like $GdVO_4$:Yb^{3+}:Er^{3+}.[49] The temperature resolution of ∼0.37 K was obtained from $\delta R/S_a$, where δR is the standard deviation of the residuals in the polynomial interpolation of the experimental data points (temperature vs $R = I_{G1}/I_{G2}$).

CONCLUSION

The upconversion luminescence properties of citrate-stabilized nanoparticles (UCNP) based on a $NaYF_4$ host matrix, which was doped with Yb^{3+} and Er^{3+} as sensitizer and activator, respectively, were studied. In order to tailor the UCNP properties, different amounts of Gd^{3+} were codoped. The luminescence properties UCNP were characterized, and the temperature dependence of different luminescence parameters (spectral intensity distribution, decay kinetics) was analyzed for the temperature range of 4 K < T < 328 K. In complementary measurements using XRD, TEM, and DLS the distinct alteration of fundamental properties such as particle size and crystal phase depending on the Gd^{3+} content was found. With increasing Gd^{3+} content the particle size obtained decreased from 274 to 46 nm for the highest Gd^{3+} content tested. Here, the Gd^{3+} ions increase the effective surface charge which is a key factor for the crystal growth rate. In addition, also the type of crystal phase was shifted from the cubic α-phase to the hexagonal β-phase. Both decreasing particle size and crystal phase change were reflected in the upconversion luminescence properties of the particles. The overall luminescence intensity first increased with increasing Gd^{3+} concentration due to the change of the host lattice to the β-phase, which is known to improve the luminescence. On the other hand, the volume to surface ratio was also changed, and the higher relative surface area lead to an enhanced luminescence quenching due to interactions (e.g., with solvent molecules like water) at the particle surface. This effect became dominant for high Gd^{3+} concentrations. This was also supported by the luminescence decay kinetics. Not only the overall luminescence intensity was dependent on the degree of Gd^{3+} doping but also the spectral distribution which gives a unique opportunity for multiparameter sensing or labeling applications. Here, the particles, which are identical with respect to their fundamental chemical reactivities (e.g., surface functionalization), may be used as multicolor labels which can be identified by their emission pattern. The interplay between intensity as well as spectral distribution and the Gd^{3+} content was further investigated by recording the temperature dependence of different photophysical parameters. Especially the application of high-resolution luminescence spectroscopy at ultralow temperature in combination with narrow banded excitation proved to be a valuable tool to shed light on the different population processes involved for the sensitizer (Yb^{3+}) and activator (Er^{3+}). The temperature profile of the luminescence intensity as well as the intensity distribution (e.g., ratio of the green and red emission) was strongly depending on the Gd^{3+} content. The intensity ration of the different Er^{3+} luminescence bands can be envisioned to be used as a nanothermometer, e.g., to measure the temperature spatially resolved in tissues.

ASSOCIATED CONTENT

Supporting Information

TEM image of UCNP $NaYF_4$:Yb/Er (18/2 mol %) with a Gd^{3+} dopand concentration of 45 mol %; upconversion luminescence spectra of $NaYF_4$:Yb/Er (18/2 mol %) with various Gd^{3+} dopand concentration and various temperatures; excitation spectra and results of ICP-OES studies of the as-prepared UCNP at various Gd^{3+} dopand concentration. This material is available free of charge via the Internet at http://pubs.acs.org.

AUTHOR INFORMATION

Corresponding Author

*E-mail Kumke@uni-potsdam.de (M.U.K.).

Notes

The authors declare no competing financial interest.

ACKNOWLEDGMENTS

We are thankful to Dr. C. Günter and Dr. C. Prietzel (work group of Prof. J. Kötz), who performed the structural studies (XRD and TEM studies) of the samples. We further thank Prof.

DOI: 10.1021/jp5103548
J. Phys. Chem. C 2015, 119, 3363−3373

The Journal of Physical Chemistry C Article

E. Rühl for fruitful discussions as well as Dr. J. Traeger and Prof. H.-J. Holdt, who performed the ICP-OES analysis for us.

REFERENCES

(1) Kuningas, K.; Ukonaho, T.; Päkkilä, H.; Rantanen, T.; Rosenberg, J.; Lövgren, T.; Soukka, T. Upconversion Fluorescence Resonance Energy Transfer in a Homogeneous Immunoassay for Estradiol. *Anal. Chem.* **2006**, *78*, 4690−4696.

(2) Soukka, T.; Rantanen, T.; Kuningas, K. Photon Upconversion in Homogeneous Fluorescence-based Bioanalytical Assays. *Ann. N. Y. Acad. Sci.* **2008**, *1130*, 188−200.

(3) Chen, N.-T.; Cheng, S.-H.; Liu, C.-P.; Souris, J. S.; Chen, C.-T.; Mou, C.-Y.; Lo, L.-W. Recent Advances in Nanoparticle-Based Förster Resonance Energy Transfer for Biosensing, Molecular Imaging and Drug Release Profiling. *Int. J. Mol. Sci.* **2012**, *13*, 16598−16623.

(4) Lee, D.-E.; Koo, H.; Sun, I.-C.; Ryu, J. H.; Kim, K.; Kwon, I. C. Multifunctional Nanoparticles for Multimodal Imaging and Theragnosis. *Chem. Soc. Rev.* **2012**, *41*, 2656−2672.

(5) Liu, Y.; Tu, D.; Zhu, H.; Chen, X. Lanthanide-Doped Luminescent Nanoprobes: Controlled Synthesis, Optical Spectroscopy, and Bioapplications. *Chem. Soc. Rev.* **2013**, *42*, 6924−6958.

(6) Min, Y.; Li, J.; Liu, F.; Padmanabhan, P.; Yeow, E. K. L.; Xing, B. Recent Advance of Biological Molecular Imaging Based on Lanthanide-Doped Upconversion-Luminescent Nanomaterials. *Nano Mater.* **2014**, *4*, 129−154.

(7) Sun, L.-D.; Wang, Y.-F.; Yan, C.-H. Paradigms and Challenges for Bioapplication of Rare Earth Upconversion Luminescent Nanoparticles: Small Size and Tunable Emission/Excitation Spectra. *Acc. Chem. Res.* **2014**, *47*, 1001−1009.

(8) Gorris, H. H.; Wolfbeis, O. S. Photonen aufkonvertierende Nanopartikel zur optischen Codierung und zum Multiplexing von Zellen, Biomolekülen und Mikrosphären. *Angew. Chem.* **2013**, *125*, 3668−3686.

(9) Zhou, J.; Liu, Z.; Li, F. Upconversion Nanophosphors for Small-Animal Imaging. *Chem. Soc. Rev.* **2012**, *41*, 1323−1349.

(10) Wang, F.; Han, Y.; Lim, C. S.; Lu, Y.; Wang, J.; Xu, J.; Chen, H.; Zhang, C.; Hong, M.; Liu, X. Simultaneous Phase and Size Control of Upconversion Nanocrystals through Lanthanide Doping. *Nature* **2010**, *463*, 1061−1065.

(11) Shan, J.; Uddi, M.; Yao, N.; Ju, Y. Anomalous Raman Scattering of Colloidal Yb3^{+},Er^{3+} Codoped $NaYF_4$ Nanophosphors and Dynamic Probing of the Upconversion Luminescence. *Adv. Funct. Mater.* **2010**, *20*, 3530−3537.

(12) Shan, J.; Kong, W.; Wei, R.; Yao, N.; Ju, Y. An Investigation of the Thermal Sensitivity and Stability of the β-$NaYF_4$:Yb,Er Upconversion Nanophosphors. *J. Appl. Phys.* **2010**, *107*, 054901.

(13) Wu, K.; Cui, J.; Kong, X.; Wang, Y. Temperature Dependent Upconversion Luminescence of Yb/Er Codoped $NaYF_4$ Nanocrystals. *J. Appl. Phys.* **2011**, *110*, -.

(14) Yu, W.; Xu, W.; Song, H.; Zhang, S. Temperature-Dependent Upconversion Luminescence and Dynamics of $NaYF_4$:Yb^{3+}/Er^{3+} Nanocrystals: Influence of Particle Size and Crystalline Phase. *Dalton Trans.* **2014**, *43*, 6139−6147.

(15) Li, X.; Wang, R.; Zhang, F.; Zhao, D. Engineering Homogeneous Doping in Single Nanoparticle To Enhance Upconversion Efficiency. *Nano Lett.* **2014**, *14*, 3634−3639.

(16) Fischer, L. H.; Harms, G. S.; Wolfbeis, O. S. Upconverting Nanoparticles for Nanoscale Thermometry. *Angew. Chem., Int. Ed.* **2011**, *50*, 4546−4551.

(17) Wang, X.; Kong, X.; Yu, Y.; Sun, Y.; Zhang, H. Effect of Annealing on Upconversion Luminescence of ZnO:Er^{3+} Nanocrystals and High Thermal Sensitivity. *J. Phys. Chem. C* **2007**, *111*, 15119−15124.

(18) Lei, Y.; Song, H.; Yang, L.; Yu, L.; Liu, Z.; Pan, G.; Bai, X.; Fan, L. Upconversion Luminescence, Intensity Saturation Effect, and Thermal Effect in Gd_2O_3:Er$_3$,Yb^{3+} Nanowires. *J. Chem. Phys.* **2005**, *123*, -.

(19) Wang, Y.; Tu, L.; Zhao, J.; Sun, Y.; Kong, X.; Zhang, H. Upconversion Luminescence of $NaYF_4$:Yb3^{+}, Er^{3+}-$NaYF_4$ Core/Shell Nanoparticles: Excitation Power Density and Surface Dependence. *J. Phys. Chem. C* **2009**, *113*, 7164−7169.

(20) Pires, A.; Heer, S.; Güdel, H.; Serra, O. Er, Yb Doped Yttrium Based Nanosized Phosphors: Particle Size, as Host Lattice and Doping Ion Concentration Effects on Upconversion Efficiency. *J. Fluoresc.* **2006**, *16*, 461−468.

(21) van der Ziel, J. P.; Ostermayer, F. W.; Van Uitert, L. G. Infrared Excitation of Visible Luminescence in $Y_{1-x}Er_xF_3$ via Resonant Energy Transfer. *Phys. Rev. B* **1970**, *2*, 4432−4441.

(22) Silver, J.; Martinez-Rubio, M. I.; Ireland, T. G.; Fern, G. R.; Withnall, R. Yttrium Oxide Upconverting Phosphors. 3. Upconversion Luminescent Emission from Europium-Doped Yttrium Oxide under 632.8 nm Light Excitation. *J. Phys. Chem. B* **2001**, *105*, 9107−9112.

(23) Yu, W.; Xu, W.; Song, H.; Zhang, S. Temperature-Dependent Upconversion Luminescence and Dynamics of $NaYF_4$:Yb^{3+}/Er^{3+} Nanocrystals: Influence of Particle Size and Crystalline Phase. *Dalton Trans.* **2014**, *43*, 6139−6147.

(24) Dyck, N. C.; van Veggel, F. C. J. M.; Demopoulos, G. P. Size-Dependent Maximization of Upconversion Efficiency of Citrate-Stabilized β-Phase $NaYF_4$:Yb^{3+},Er^{3+} Crystals via Annealing. *ACS Appl. Mater. Interfaces* **2013**, *5*, 11661−11667.

(25) Sudarsan, V.; Sivakumar, S.; van Veggel, F. C. J. M.; Raudsepp, M. General and Convenient Method for Making Highly Luminescent Sol-Gel Derived Silica and Alumina Films by Using LaF_3 Nanoparticles Doped with Lanthanide Ions (Er^{3+}, Nd^{3+}, and Ho^{3+}). *Chem. Mater.* **2005**, *17*, 4736−4742.

(26) Jiang, T.; Liu, Y.; Liu, S.; Liu, N.; Qin, W. Upconversion Emission Enhancement of Gd^{3+} Ions Induced by Surface Plasmon Field in Au@$NaYF_4$ Nanostructures Codoped with Gd^{3+}/Yb^{3+}/Tm^{3+} Ions. *J. Colloid Interface Sci.* **2012**, *377*, 81−87.

(27) Wang, L.; Xue, X.; Chen, H.; Zhao, D.; Qin, W. Unusual Radiative Transitions of Eu^{3+} Ions in Yb/Er/Eu Tri-doped $NaYF_4$ Nanocrystals under Infrared Excitation. *Chem. Phys. Lett.* **2010**, *485*, 183−186.

(28) Song, Y.; Tian, Q.; Zou, R.; Chen, Z.; Yang, J.; Hu, J. Phase and Luminescent Intensity Control of Hydrophilic Rare-Earth up-Converting Nanophosphors Prepared by One-Pot Solvothermal Synthesis. *J. Alloys Compd.* **2011**, *509*, 6539−6544.

(29) Wilhelm, S.; Hirsch, T.; Patterson, W. M.; Scheucher, E.; Mayr, T.; Wolfbeis, O. S. Multicolor Upconversion Nanoparticles for Protein Conjugation. *Theranostics* **2013**, *3*, 239−248.

(30) Suyver, J.; Grimm, J.; van Veen, M.; Biner, D.; Krämer, K.; Güdel, H. Upconversion Spectroscopy and Properties of $NaYF_4$ Doped with Er^{3+}, Tm^{3+} and/or Yb^{3+}. *J. Lumin.* **2006**, *117*, 1−12.

(31) Banski, M.; Podhorodecki, A.; Misiewicz, J.; Afzaal, M.; Abdelhady, A. L.; O'Brien, P. Selective excitation of Eu^{3+} in the Core of Small β-$NaGdF_4$ Nanocrystals. *J. Mater. Chem. C* **2013**, *1*, 801−807.

(32) Wang, F.; Deng, R.; Wang, J.; Wang, Q.; Han, Y.; Zhu, H.; Chen, X.; Liu, X. Tuning Upconversion through Energy Migration in Core-Shell Nanoparticles. *Nat. Mater.* **2011**, *10*, 968−973.

(33) Suyver, J.; Grimm, J.; Krämer, K.; Güdel, H. Highly Efficient Near-Infrared to Visible Up-Conversion Process. *J. Lumin.* **2005**, *114*, 53−59.

(34) Vetrone, F.; Boyer, J. C.; Capobianco, J. A.; Speghini, A.; Bettinelli, M. Effect of Yb^{3+} Codoping on the Upconversion Emission in Nanocrystalline Y_2O_3:Er^{3+}. *J. Phys. Chem. B* **2003**, *107*, 1107−1112.

(35) Shalav, A.; Richards, B. S.; Krämer, K.; Güdel, H. Improvements If an Up-conversion $NaYF_4$:Er^{3+} Phosphor/Silicon Solar Cell System for an Enhanced Response in the Near-Infrared. *IEEE* **2005**, 114−117.

(36) Bünzli, J.-C. G.; Eliseeva, S. V. Lanthanide Luminescence for Functional Materials and Bio-sciences. *Chem. Soc. Rev.* **2010**, *39*, 189−227.

(37) Van Dijk, J. M. F.; Schuurmans, M. F. H. On the Nonradiative and Radiative Decay Rates and a Modified Exponential Energy Gap Law for 4f-4f Transitions in Rare-Earth Ions. *J. Chem. Phys.* **1983**, *78*, 5317−5323.

DOI: 10.1021/jp5103548
J. Phys. Chem. C 2015, 119, 3363−3373

(38) Han, S.; Deng, R.; Xie, X.; Liu, X. Enhancing Luminescence in Lanthanide-Doped Upconversion Nanoparticles. *Angew. Chem., Int. Ed.* **2014**, *53*, 11702−11715.
(39) Carnall, W. T.; Fields, P. R.; Wybourne, B. G. Spectral Intensities of the Trivalent Lanthanides and Actinides in Solution. I. Pr^{3+}, Nd^{3+}, Er^{3+}, Tm^{3+}, and Yb^{3+}. *J. Chem. Phys.* **1965**, *42*, 3797−3806.
(40) Li, X.; Zhang, F.; Zhao, D. Lab on Upconversion Nanoparticles: Optical Properties and Applications Engineering via Designed Nanostructure. *Chem. Soc. Rev.* **2014**, in press.
(41) Shalav, A.; Richards, B. S. Enhancing the Near-Infrared Spectral Response of Silicon Optoelectronic Devices via Up-Conversion. *IEEE* **2007**, *54*, 2679−2684.
(42) Yi, G.; Lu, H.; Zhao, S.; Ge, Y.; Yang, W.; Chen, D.; Guo, L.-H. Synthesis, Characterization, and Biological Application of Size-Controlled Nanocrystalline $NaYF_4$:Yb,Er Infrared-to-Visible Up-Conversion Phosphors. *Nano Lett.* **2004**, *4*, 2191−2196.
(43) Thoma, R. E.; Insley, H.; Hebert, G. M. The Sodium Fluoride-Lanthanide Trifluoride Systems. *Inorg. Chem.* **1966**, *5*, 1222−1229.
(44) Li, D.; Shao, Q.; Dong, Y.; Jiang, J. Anomalous Temperature-Dependent Upconversion Luminescence of Small-Sized $NaYF_4$:Yb^{3+}:Er^{3+}. *J. Phys. Chem. C* **2014**, *118*, 22807−22813.
(45) Xu, C. T.; Zhan, Q.; Liu, H.; Somesfalean, G.; Qian, J.; He, S.; Andersson-Engels, S. Upconverting Nanoparticles for Pre-clinical Diffuse Optical Imaging, Microscopy and Sensing: Current Trends and Future Challenges. *Laser Photonics Rev.* **2013**, *7*, 663−697.
(46) Hernderson, B.; Imbusch, G. F. *Optical Spectroscopy of Inorganic Solids*; Clarendon Press: Oxford, 1989.
(47) Lawrence, T. A.; Murra, K. A.; May, P. S. Temperature Dependence of Rate Constants for Tb^{3+}(5D3) Cross Relaxation in Symmetric Tb^{3+} Pairs in Tb-Doped $CsCdBr_3$, $CsMgBr_3$, $CsMgCl_3$. *J. Phys. Chem. B* **2003**, *107*, 4002−4011.
(48) Wang, L.; Yan, R.; Huo, Z.; Wang, L.; Zeng, J.; Bao, J.; Wang, X.; Peng, Q.; Li, Y. Fluorescence Resonant Energy Transfer Biosensor Based on Upconversion-Luminescent Nanoparticles. *Angew. Chem., Int. Ed.* **2005**, *44*, 6054−6057.
(49) Gavrilovic, T.; Jovanovic, D.; Lojpur, V.; Dramicanin, M. Multifunctional Eu^{3+}- and Er^{3+}/Yb^{3+}-Doped $GdVO_4$ Nanoparticles Synthesized by Reverse Micelle Method. *Sci. Rep.* **2014**, *4*, 4209.
(50) Tian, Y.; Tian, B.; Cui, C. 'e.; Huang, P.; Wang, L.; Chen, B. Excellent Optical Thermometry Based on Single-Color Fluorescence in Spherical $NaEuF_4$ Phosphor. *Opt. Lett.* **2014**, *39*, 4164−4167.
(51) Brites, C. Thermoetry at the Nanoscale. *Nanoscale* **2012**, *4*, 4799−4829.
(52) Debasu, M. All-in-One Optical Heater-Thermometer Nanoplatform Operative from 300 to 2000 K Based on Er^{3+} Emission and Blackbody Radiation. *Adv. Mater.* **2013**, *25*, 3254−3258.

DOI: 10.1021/jp5103548
J. Phys. Chem. C 2015, 119, 3363−3373

2.3 Fundamental Research and Challenges of an UC-based Nanothermometer

"Upconversion $NaYF_4$:Yb:Er nanoparticles co-doped with $Gd^{3+}$and Nd^{3+} for thermometry on the nanoscale"

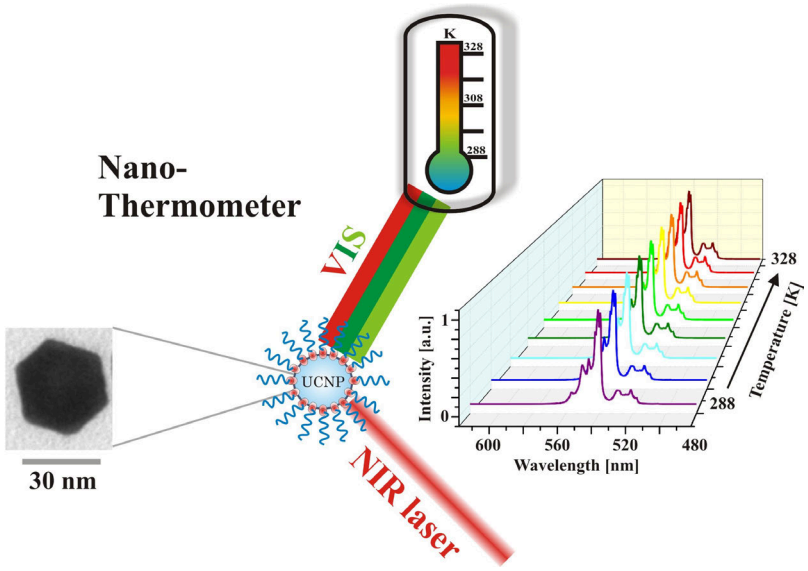

RSC Adv., **2015**, *5*, 67149-67156.

Thesis pages: 42–49

Author Contribution to the manuscript:

I performed the complete synthesis (including further surface modification) of all nanoparticles as well as parts of the structural characterization (DLS and Raman investigations). I performed the steady-state and laser power/ temperature dependent measurements. I completely analyzed and interpreted the photophysical-/ structural analytical data and prepared the spectra published. I wrote the manuscript, in close corporation with Michael Kumke.

RSC Advances

PAPER

View Article Online
View Journal | View Issue

CrossMark click for updates

Cite this: *RSC Adv.*, 2015, **5**, 67149

Upconversion $NaYF_4$:Yb:Er nanoparticles co-doped with Gd^{3+} and Nd^{3+} for thermometry on the nanoscale†

D. T. Klier‡ and M. U. Kumke‡

Received 16th June 2015
Accepted 30th July 2015

DOI: 10.1039/c5ra11502g

www.rsc.org/advances

In the present work, the upconversion luminescence properties of oleic acid capped $NaYF_4$:Gd^{3+}:Yb^{3+}:Er^{3+} upconversion nanoparticles (UCNP) with pure β crystal phase and Nd^{3+} ions as an additional sensitizer were studied in the temperature range of 288 K < *T* < 328 K. The results of this study showed that the complex interplay of different mechanisms and effects, causing the special temperature behavior of the UCNP can be developed into thermometry on the nanoscale, *e.g.* to be applied in biological systems on a cellular level. The performance was improved by the use of Nd^{3+} as an additional dopant utilizing the cascade sensitization mechanism in tri-doped UCNP.

1. Introduction

Temperature is a fundamental parameter of key importance in many different fields of science and technology. Respective sensors are widely used in on a daily basis in climate and marine research as well as in chemistry, biology, metrology, and medicine.[1–3] It is estimated that the share of temperature sensors amounts to as much as 75–80% of the world's sensor market.[4] Indeed, current technological demands like microfluidics or nano medicine have reached a point at which a spatial resolution on the submicron scale is needed.[5] For example the mapping of the temperature in living cells, *i.e.* cancer cells compared to normal tissue have a higher temperature due to the increased metabolic activity, which strongly improves the perception of their pathology and physiology and in turn can help to optimize diagnosis and therapeutic approaches, *e.g.*, hydrothermal treatment or photodynamic therapy. In particular a thermometer capable of subdegree temperature resolution as well as integration on a cellular level could provide a powerful new tool in many areas of biochemical and biophysical research.[5,6] Many promising approaches for local temperature sensing are being explored at present such as Raman spectroscopy,[6] scanning probe microscopy[6] and luminescent based measurements using organic dyes,[7,8] nanomaterials[9–11] such as quantum dots (QD) or proteins.[8] Many of these already existing methods suffer on several drawbacks such as low sensitivity, low reproducibility or systematic errors due to fluctuations in the luminescence rate or local chemical environment.[10]

Our approach to nanoscale thermometry uses luminescence upconversion nanoparticles (UCNP), which are suitable for investigation in different biological matrices. The UCNP are excited with light in the near infrared range (NIR), where interferences from background fluorescence can be neglected.[12] In the chosen excitation wavelength range between 795 nm < λ_{ex} < 976 nm many biological matrices are nearly transparent.[13] Consequently, the penetration depth in this spectral range is very high for a human skin or in blood (see Fig. 1) and a high sensitivity in sensing applications without additional sample preparations can be established.[13] One of the first promising approaches for upconversion nanoparticle based thermometry

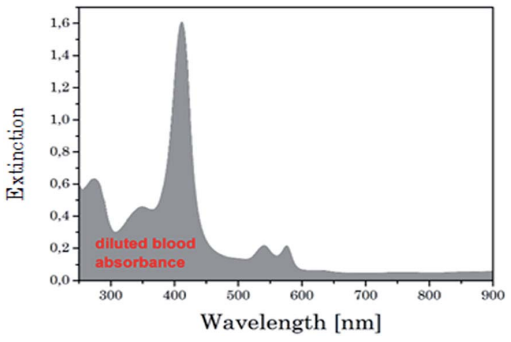

Fig. 1 Absorption spectra of diluted blood.

University of Potsdam, Department of Chemistry (Physical Chemistry), Karl-Liebknecht-Str. 24-25, 14476 Potsdam, Germany. E-mail: kumke@uni-potsdam.de

† Electronic supplementary information (ESI) available: DLS analysis of $UCNP_{Nd,OA}$ $NaYF_4$:Yb/Er (17/3 mol%) with a Nd^{3+} dopant concentration of 2 mol% and UCNP. Excitation emission matrices of $UCNP_{Nd}$ are shown. Power dependence of the Er^{3+} transitions G1, G2 and R of oleic acid capped UCNP at different excitation wavelength are shown as well as the temperature dependence of the upconversion luminescence of $UCNP_{Nd}$ dissolved in water at different irradiation wavelength and thermostat temperature over time. See DOI: 10.1039/c5ra11502g

‡ These authors equally contributed to this study.

View Article Online
RSC Advances Paper

on nanoscale was developed by Zink *et al.*[14] They used a dual core (made of UCNP and smaller superparamagnetic nanocrystal) mesoporous silica nano-particle that acted as nanothermometer as well as nanoheater. An in-depth investigation of the potential of UCNP as nanothermometer was carried out by Wolfbeis *et al.* using different lanthanide combination and capping agents.[15] Here, the best results were found for $NaYF_4$:Yb^{3+}:Er^{3+} core/shell nanoparticles. Moreover, UCNP can be developed into multimodal probes, *e.g.*, with additives like gadolinium (Gd^{3+}) ions UCNP can be used for magnet resonance imaging or with the appropriate functionalization for optical imaging or assay applications.[16–18] Apart from the excitation at $\lambda_{ex} = 976$ nm Han *et al.* report on UCNP with additional Nd^{3+} doping which could be excited at $\lambda_{ex} = 800$ nm. This type of UCNP showed a better biocompatibility due to lower impact on biological tissues and a higher penetrability for the excitation light.[19]

In the present work, the potential of oleic acid-capped $NaYF_4$:Gd^{3+}:Yb^{3+}:Er^{3+} upconversion nanoparticles (UCNP) for thermometry on nanometer scales was studied in the temperature range of 288 K < T < 328 K. Both, the overall luminescence intensity and the ratio of luminescence bands were found to be highly sensitive on temperature. For the temperature determination the intensity ratio of the luminescence signal in the green Er^{3+} luminescence bands ($^2H_{11/2} \rightarrow {}^4I_{15/2}$ (G1) and $^4S_{3/2} \rightarrow {}^4I_{15/2}$ (G2)) was used. The relative sensitivity (S_r) with 1.49% K^{-1} of the UCNP under investigation is one of the highest S_r value which found in literature for $NaYF_4$:Yb^{3+}:Er^{3+} type nanoparticles or other host lattices like $GdVO_4$:Yb^{3+}:Er^{3+} or $Na_2Y_2B_2O_7$:Yb^{3+}:Tm^{3+}.[20,21]

The overlapping of the excitation light at $\lambda_{ex} = 976$ nm with the absorption of water (see Fig. 2), which may induce heating damage in cells and tissues, is a drawback *e.g.*, for nanoparticle-based imaging or for deep tissue imaging (this experiments require high excitation energy and long-term excitation). To overcome this limitation, Nd^{3+} was used as additional lanthanide. Nd^{3+} has an absorption maximum around $\lambda = 800$ nm, which can be used for the initial excitation of the UCNP. At this excitation wavelength the intrinsic water absorption is one order of magnitude lower compared to $\lambda_{ex} = 976$ nm resulting in less heating of the sample by the laser irradiation (see Fig. 2). Subsequently a better biocompatibility and higher penetration depth in aqueous systems can be envisaged. Colloidal tri-doped (Yb^{3+}, Er^{3+} and Gd^{3+} ions) UCNPs with Nd^{3+} were successfully generated and optimized for maximum upconversion efficiency with an excitation wavelength of $\lambda_{ex} = 800$ nm.

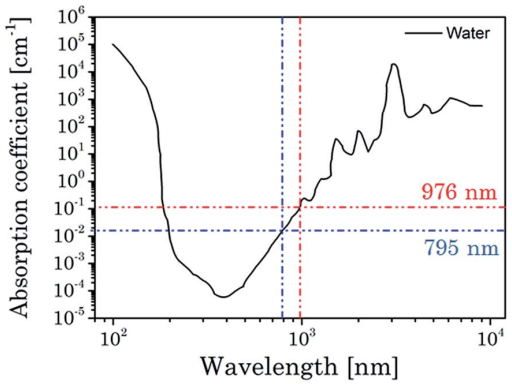

Fig. 2 Absorption coefficient of water in a spectral range of 100 to 10 000 nm. Values for typically excitation of Yb^{3+} ions at 976 nm and Nd^{3+} ions are high lighted.[11]

2. Experimental

2.1 Materials

All rare earth chloride hydrates $RECl_3 \cdot xH_2O$ (RE: Y, Yb, Gd, Nd and Er, 99.9%) were purchased from Sigma Aldrich and Alfa Aesar. Ammonium fluoride (NaF, 99.99%), ethanol (absolute) and chloroform (99.8%) were purchased from Sigma Aldrich. Sodium hydroxide (NaCl, 99%) was purchased from Carl Roth and oleic acid (90%) from Alfa Aesar. 2-Aminoethyl dihydrogen phosphate (AEP) (98%) and octadecen (91%) were obtained from Merck. Argon (Ar, 5.0) was received from Praxair and was dried with sicapent. All further chemical reagents used in experiments were directly used without any further purification. For the experiments double distilled water was used.

2.2 Synthesis of $NaYF_4$:Yb^{3+}:Gd^{3+}:Er^{3+} (UCNP) and UCNP:Nd^{3+} ($UCNP_{Nd}$)

The UCNP were synthesized according to a previously reported procedure in which a thermal decomposition method with oleic acid as a capping agent was used.[22,23] The synthesis was designed to keep a constant overall amount of lattice ions (Y^{3+}, Yb^{3+}, Er^{3+}, Nd^{3+}, and Gd^{3+}) in the different samples to study the effect of neodymium. The concentration of the lanthanides (Ln) Er^{3+} and Yb^{3+} was constant for all samples whereas parts of the Y^{3+} ions were replaced by Nd^{3+} ions. $GdCl_3$ hexahydrate (0.61 mmol), $ErCl_3$ (0.06 mmol), $YbCl_3$ (0.34 mmol), $NdCl_3$ (0.02 mmol) and YCl_3 (0.99 mmol) were dissolved under Ar atmosphere in a mixture of oleic acid (13.4 g) and octadecen (35 mL) under stirring. The solution was evacuated (1 mbar) for 45 minutes until evolution of gas had stopped. The reaction mixture was heated to 140 °C under Ar atmosphere until a yellowish clear solution occurs. After the solution had been cooled to 45 °C, ammonium fluoride (300 mg) and sodium hydroxide (150 mg) was added to the reaction mixture under stirring until a clear solution was formed. The solution was heated to 310 °C for 90 minutes using a heating mantle. A discoloration (yellow/brown) of the reaction mixture as well as a white precipitation occurs. When the reaction mixture reached room temperature, the nanoparticles were separated *via* centrifugation (6000 rpm for 25 min) and further purified by several redispersion and centrifugation steps in ethanol. The obtained white powder was dissolved in cyclohexane and filtrated using a 0.2 μm PTFE syringe filter. The as-synthesized UCNPs disperse readily in non polar solvents such as cyclohexane, forming a clear colloidal solution. The oleic acid capped UCNP stored at room temperature were colloidal stable for several months.

View Article Online
Paper RSC Advances

2.3 Synthesis of water soluble AEP-capped UCNP

In a typically ligand exchange reaction 150 mg AEP was diluted in solvents mixture of ethanol and ultrapure water (4 mL/6 mL) and 20 mg UCNP dispersed in 5 mL chloroform were added slowly drop wise.[24] The reaction mixture was stirred for 48 h at room temperature, whereas the UCNP moved obviously from the chloroform to the watery phase. After the phase separation the watery phase was centrifuged at 6000 rpm for 25 minutes and the obtained modified UCNP were redispersed in ultrapure water. The AEP-modified UCNP were stored under exclusion of light and different temperature between −10 and 20 °C to get information of the long-term colloidal stability.

2.4 Structural characterization

The size and morphology of as-prepared UCNPs were observed on a JEM 1011 transmission electron microscope (Jeol Ltd, Tokyo, Japan) (TEM) using a wolfram hairpin cathode, an accelerating voltage of 80 kV and a molybdenum panel. The measurements were recorded using a side-mounted Olympus Mega View G2 (Olympus Germany GmbH, Hamburg, Germany). Particle size characterizations were also carried out with dynamic light scattering (DLS) by using a ZETASIZER Nano ZS (Malvern Instruments Ltd, Herrenberg, Germany) as well. As light source a He–Ne laser at $\lambda = 633$ nm was used.

X-ray powder diffraction patterns were obtained using a D5005 (Siemens AG, Munich, Germany) in a range of 3–70°/2θ with divergence aperture, scattering ray aperture and graphite monochromatized Cu Kα radiation (λ = 0.15406 nm). The scanning step was 0.02°/2θ with a counting time of 4 s per step. The nanocrystalline domain sizes were calculated using the Debye–Scherrer equation (eqn (1)):

$$D = \frac{0.89\ \lambda}{B\ \cos(\theta)} \quad (1)$$

D is the domain size to be determined, λ is the wavelength of the X-ray, B is the FWHM of the diffraction peak of interest and θ is the angle of the corresponding diffraction peak.

2.5 Room temperature steady state luminescence spectra

Room temperature (ν = 23 °C) steady state luminescence spectra were obtained using a wavelength tunable pulsed Nd:YAG/OPO laser system (laser: Quanta Ray, Spectra-Physics, Mountain View, CA, USA; OPO: GWU-Lasertechnik Vertriebsges. mbH, Erftstadt, Germany) operating at 10 Hz as excitation light source (at 26 mJ/130 mW) and recorded using an intensified CCD-camera (iStar DH720-18V-73, Andor Technology, Belfast, Great Britain) coupled to a spectrograph (Shamrock SR 303i, Andor Technology, Belfast, Great Britain) equipped with a 600 L mm^{-1} grating blazed at 500 nm.

2.6 Upconversion luminescence measurements at various temperature (288 to 328 K)

In order to study the upconversion luminescence properties at various temperature the experimental set up mentioned above was extended by a water-cooled Peltier element-based temperature adjustable sample holder (temperature controller GR2012 itron 32, JUMO GmbH & Co, Fulda, Germany). In order to ensure the temperature stability the samples were temperated for 15 minutes at the certain temperature. As an additional control a conventional temperature sensor (Testo 945, Testo AG, Lenzkirch, Germany) was used to monitor the temperature of UCNP containing solution under investigation. For all spectroscopic measurements quartz cuvettes sealed with Parafilm® were used.

2.7 Power dependency of upconversion luminescence at room temperature

The intensity of upconversion emission was measured as function of excitation power at $\lambda_{ex} = 976$ nm (further details on equipment *vide supra*). The attenuation of excitation light was achieved by the use of neutral density filters (optical density (OD) 0.1–1.0). The upconversion emission intensity I_{UC} strongly depends on the excitation power I_P (see eqn (2)):[21]

$$I_{UC} \propto (I_P)^n \quad (2)$$

here n is the number of photons required to populate the emitting state of the lanthanides. The power dependence of the Er^{3+} transitions $^2H_{11/2} \rightarrow {}^4I_{15/2}$ (G1), $^4S_{3/2} \rightarrow {}^4I_{15/2}$ (G2) and $^4F_{9/2} \rightarrow {}^4I_{15/2}$ (R) is shown in ESI Fig. 1† using a log I_P − log I_{UC} plot, in which n was calculated from the slope.

3. Results and discussion

3.1 Structural investigations

The particle size and morphology of UCNP and $UCNP_{Nd}$ were studied using TEM, XRD and DLS, respectively. The TEM images of the different UCNP showed that the particles were hexagonal in shape (Fig. 3).[25] In order to determine the average particle size from TEM images approximately 200 particles were included in the statistical analysis (see Table 1).

In addition, DLS and XRD was used as a complementary method for particle size determination. The results of the DLS, TEM and XRD measurements are also shown in Table 1 (see ESI

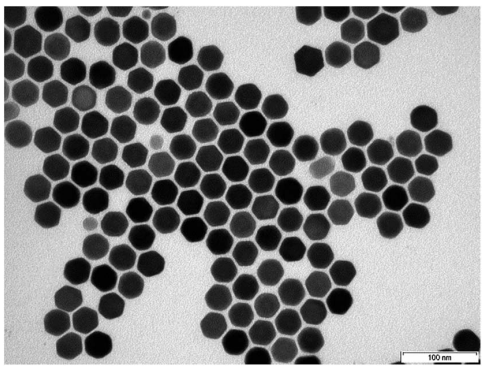

Fig. 3 TEM image of $NaYF_4$:Yb^{3+}:Er^{3+}:Nd^{3+} doped upconversion nanoparticles.

Table 1 Results (full width at halt maximum (FWHM) and particle diameter) of the DLS-, TEM- and XRD analysis of several UCNP synthesis with the same composition and additionally Nd^{3+} doping (n.d.: not determined)

Sample	UCNP	$UCNP_{Nd}$	$UCNP_{Nd,AEP}$
Particle diameter-DLS (nm)	30.2 ± 0.2	29.7 ± 0.1	81.1 ± 0.3
Particle diameter-TEM (nm)	n.d.	34.5 ± 0.1	n.d.
Particle diameter-XRD (nm)	33.9 ± 3.1	32.7 ± 4.2	n.d.
FWHM-DLS	3.3 ± 0.1	3.1 ± 0.1	19.3 ± 0.8
FWHM-TEM	n.d.	1.8 ± 0.3	n.d.

Fig. 2 and 3†). Corroborating the results of the TEM images, DLS and XRD showed as well no particle size alteration upon addition of Nd^{3+}, which was expected due to the very similar atomic radius of the different lanthanides used. Furthermore, it can be assumed that the UCNP/$UCNP_{Nd}$ are highly crystalline, due to the similar particle diameter obtained from TEM/XRD and the fact that only crystalline parts can be observed in XRD. The AEP capped $UCNP_{Nd}$ are 2.7 times larger than the oleic acid capped UCNP, which could be due to the different ligand on the surface resulting in an increase of the hydrodynamic radius or the possible formation of small aggregates. In comparison to the TEM investigations the particle size obtained from the DLS measurements are nearly similar. The deviations in particles size of TEM in comparison to the DLS are due to the fact that calculation algorithm for DLS is optimized for spherical particles whereas variations in shape leads to a change in the scattering behaviour and finally to an inaccuracy in the calculated particle diameter.

3.2 Upconversion luminescence spectroscopy studies

In Fig. 4 the luminescence spectra of the UCNP and $UCNP_{Nd}$ are shown. The optimal excitation wavelengths chosen for the samples under investigation are based on matrices of excitation emission spectra, shown in ESI Fig. 4.† The spectra were recorded in cyclohexane with $\lambda_{ex} = 976$ nm and are the result of energy upconversion processes between Yb^{3+} and Er^{3+} ions (see Scheme 1).[26] The three most intense emission bands can be observed in the green spectral region centered at $\lambda_{em} = 525$ nm ($^2H_{11/2} \rightarrow {}^4I_{15/2}$ transition, G1), 545 nm ($^4S_{3/2} \rightarrow {}^4I_{15/2}$ transition, G2), and in the red spectral region centered at $\lambda_{em} = 660$ nm ($^4F_{9/2} \rightarrow {}^4I_{15/2}$ transition, R).[27–32] The observed fine structure (Stark splitting) is induced by the crystal field splitting due to small differences in the coordination environment.[29,32,33] The Nd^{3+} containing $UCNP_{Nd}$ can be excited at $\lambda_{ex} = 976$ nm and additionally at $\lambda_{ex} = 795$ nm. For the excitation at $\lambda_{ex} = 795$ nm the mechanism of the upconversion processes is extended by an initial energy transfer step between Nd^{3+} and Yb^{3+}. First the Nd^{3+} ions are excited from the $^4I_{9/2}$ to the $^4F_{5/2}$ energy level, followed by a non-radiative relaxation step to $^4F_{3/2}$ level. Originating from this energy level the energy transfer to the $^2F_{5/2}$ level of the Yb^{3+} ions can take place. In such cases the Yb^{3+} acts like a "relay" between the sensitizer Nd^{3+} and the activator Er^{3+}.[1,34–39] The subsequent energy transfer steps and relaxation processes from the Yb^{3+} to the Er^{3+} are identical to the regular UCNP. The cross-relaxation between different excited Er^{3+} ions can be neglected in both cases due to the low Er^{3+} ion concentration used.[31,40] The Gd^{3+} ion doping was chosen to enhance the absolute upconversion luminescence intensity, due to the favoured formation of the β-phase.[41] Since the $^6P_{7/2}$ level, which represents the next electronic state above the ground state of Gd^{3+}, its emission is found in the ultra violet spectral region and is therefore much higher in energy than the relevant excited state levels of Er^{3+}, Nd^{3+}, and Yb^{3+}, respectively. Consequently, a Gd^{3+}-related luminescence quenching by energy transfer of these ions can be ruled out. The upconversion emission spectra ($\lambda_{ex} = 976$ nm) shown in Fig. 3 (right) reveal no significant differences between the UCNP and $UCNP_{Nd}$ investigated, except the G1, G2/R ratio, which is slightly increased. The additional doping of the host lattice with Nd^{3+} ions has no significant impact on the upconversion emission spectra. Also no

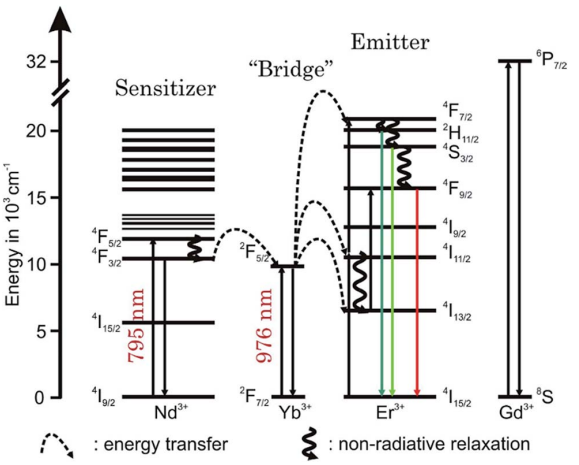

Scheme 1 Schematic energy level diagram of the upconversion mechanism of a Yb^{3+} and Er^{3+} dopant ion system following an excitation at $\lambda_{ex} = 976$ nm. Furthermore, the upconversion mechanism of a Nd^{3+}, Yb^{3+} and Er^{3+} dopant ion system following an excitation at $\lambda_{ex} = 795$ nm is shown as well. The full lines pointing upwards represent energy absorption, the dotted lines represent energy transfer, the waved lines represents non radiative relaxation processes and the colored full lines pointing downwards represents the visible emission.

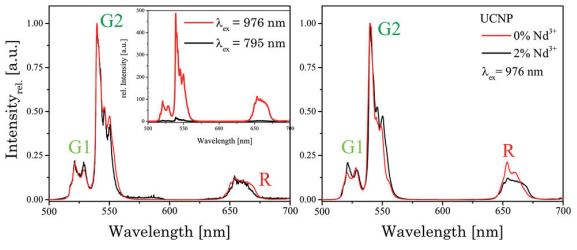

Fig. 4 [Left]: normalized upconversion luminescence spectra of $UCNP_{Nd}$ (in cyclohexane) at $\lambda_{ex} = 976$ nm and 795 nm, respectively. [Inset]: comparison of upconversion emission of $UCNP_{Nd}$ excited at different λ_{ex}. [Right]: typical upconversion emission of UCNP and $UNCP_{Nd}$ excited at $\lambda_{ex} = 976$ nm.

significant differences in the shape or fine structure of the upconversion emission spectra can be seen for different excitation wavelength, due to the fact that the Nd^{3+} ion doping only influence the population of the emitting energy level of Yb^{3+}.

On the other hand the absolute upconversion luminescence intensity is much lower (1/10 intensity) for the excitation at 795 nm (see Fig. 4 inset). The lower upconversion intensity at $\lambda_{ex} = 795$ nm is related to several additional energy transfer steps between Nd^{3+} ions and Yb^{3+} ions as well as relaxation steps of excited Nd^{3+} ions itself. The possibility for non-radiative deactivation channels is increased, subsequently leading to a less effective upconversion.

In Fig. 5 normalized upconversion emission spectra of $UCNP_{Nd}$ with different capping agents at $\lambda_{ex} = 795$ nm as well as 976 nm are shown. The ratio of the emission bands G1, G2 to R is decreased when the nanoparticles are capped with AEP. The change in the G1, G2 to R ratio could be connected to the new chemical environment at the surface of the nanoparticles with different phonon coupling processes influencing the luminescence upconversion. Due to fact that the probability for the non-radiative transition $^4I_{11/2}$ to $^4I_{13/2}$ of Er^{3+} ions is increased, the population efficiency for the energy level R is increased too, whereas of the population of G1 and G2 is decreased, because it is populated by different upconversion mechanisms. The excitation wavelength has no impact on the spectral intensity distribution including the position of the emission bands or emission band ratio as in the case of oleic acid capped UCNP in cyclohexane (see Fig. 4 above).

3.3 Temperature dependent upconversion luminescence

In ESI Fig. 5† emission spectra of UCNP in cyclohexane ($\lambda_{ex} = 976$ nm) for the temperature range of 288 K < T < 328 K are shown, which are representative for the observed temperature dependence of all UCNP and $UCNP_{Nd}$ investigated.

The following trends were observed for the different luminescence bands of Er^{3+}: (i) the luminescence intensity of the $^2H_{11/2} \rightarrow {}^4I_{15/2}$ transition (G1) gradually increased with increasing temperature and (ii) in contrast to the G1 emission band, the intensity of the G2- and R-related emission bands initially decreased slightly with increasing temperature. The difference in the temperature dependence of the G1 and G2 emission bands is connected to the population pathways of the related energy levels $^2H_{11/2}$ and $^4S_{3/2}$, respectively. In Scheme 2 a detail view of the respective Stark levels of $^2H_{11/2}$ and $^4S_{3/2}$ is shown. The Stark levels are calculated from the excitation and emission spectra of the UCNP under investigation. The population of the green emitting levels G1 and G2 ($^2H_{11/2}$ and $^4S_{3/2}$) usually occurs by successive energy transfer processes from the excited $^2F_{5/2}$ state of Yb^{3+} ions to the Er^{3+} ions exciting it first to the $^4I_{11/2}$ state and in a second step to the $^4F_{7/2}$ excited state. Followed by a non-radiative relaxation process the Er^{3+} ion deactivates to the $^2H_{11/2}$ and – due to the moderate energy gap between $^2H_{11/2}$ and $^4S_{3/2}$ states (about 700 cm^{-1}) – the Er^{3+} ions can relax fast to the $^4S_{3/2}$ state. Finally, the $^2H_{11/2}$ level is repopulated *via* thermal agitation (see Scheme 2) resulting in the observed two Er^{3+}-emission bands G1 and G2 as shown in Fig. 5 (see also Scheme 1).[28–30,42,43]

The thermal equilibration of the two levels is fast, hence the observed intensity ratio of G1 and G2 will be dependent on the temperature.

3.4 UCNP for nanoscale thermometry

For $T > 273$ K the correlation of the luminescence intensity ratio ($Z = I_{G1}/I_{G2}$) and the temperature T can be described by an Arrhenius type equation.[34,35,44]

$$Z = \frac{I_{G1}}{I_{G2}} = A \exp\left(-\frac{\Delta E_{G1/G2}}{k_B T}\right) \quad (3)$$

Z is the ratio of integrated luminescence intensity originating from band G1 and G2 which are separated by the energy gap $\Delta E_{G1/G2}$, k_B is the Boltzmann constant, T is the temperature and A is a constant which depends on the spontaneous emission rate and devolution of the energy levels of the emitting states in the host material. From Fig. 6 (left) it can be seen that Z is changing with temperature, because the relative intensity of the G1-related luminescence is increasing. This is a consequence of

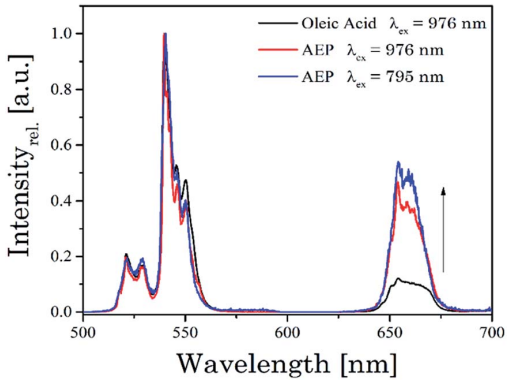

Fig. 5 Normalized upconversion emission spectra of $UCNP_{Nd}$ stabilized with the capping agents oleic acid and AEP. The excitation wavelength λ_{ex} was also varied.

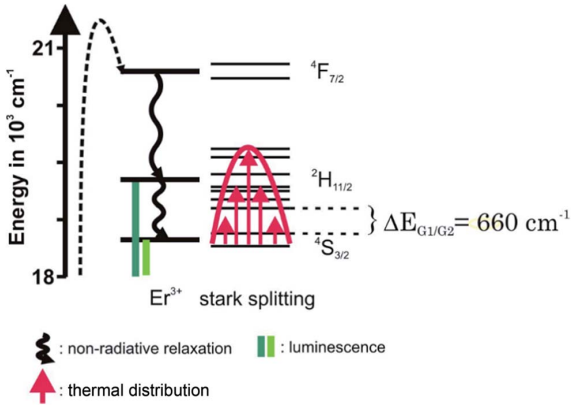

Scheme 2 Close-up of energy levels related to G1 and G2 emission in erbium.

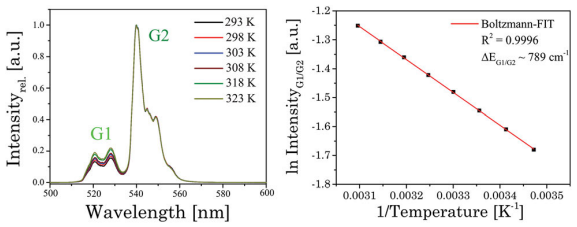

Fig. 6 [Left]: normalized upconversion emission spectra of UCNP at different temperatures. [Right]: analysis of the integrated emission intensity ratio of band G1 and G2 according to eqn (3).

the thermally induced re-distribution in population between the energy levels $^2H_{11/2}$ and $^4S_{3/2}$ (see Scheme 2). Especially for higher temperatures (T > 273 K) a distinct change with temperature was found, which is connected to the fact that the energy gap $\Delta E_{G1/G2}$ is in the order of 600–800 cm^{-1} depending on the host lattice. For UCNP an energy gap $\Delta E_{G1/G2} = 789 \pm 9$ cm^{-1} was determined, which correlates very well with the data of Carnall *et al.* who studied the energy level assignments for Er^{3+} in several host lattices.[42] Based on eqn (3) the absolute sensitivity S_a and relative sensitivity S_r can be obtained.[1,45–48]

$$S_a \sim \left|\frac{\partial Z}{\partial T}\right| \sim Z\,\frac{\Delta E_{G1/G2}}{kT^2} \quad (4)$$

$$S_r \sim 100\%\left|\frac{1}{Z}\frac{\partial Z}{\partial T}\right| \sim 100\%\,\frac{\Delta E_{G1/G2}}{kT^2} \quad (5)$$

The temperature sensitive calculated value of S_a and S_r are shown in Fig. 7. The maximum value of S_r of 1.37% K^{-1} was found at 288 K which is in the range typically found for $NaYF_4$:Yb^{3+}:Er^{3+} or other new host lattices of upconverters like $GdVO_4$:Yb^{3+}:Er^{3+}.[16] The temperature resolution of ~0.4 K was obtained from $\delta R/S_a$ where δR is the standard deviation of the residuals in the polynomial interpolation of the experimental data points (temperature *vs.* $Z = I_{G1}/I_{G2}$). In Table 2 the absolute

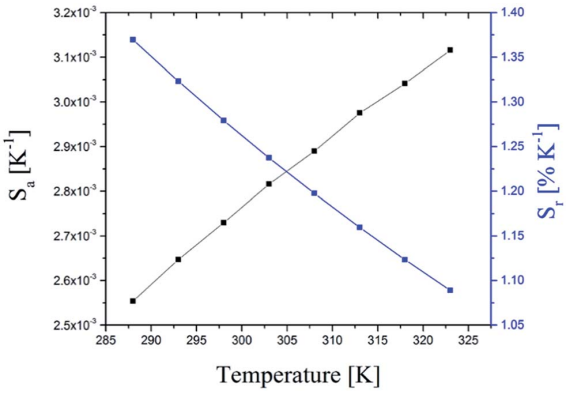

Fig. 7 Absolute (black line) and relative (blue line) sensitivity of the temperature sensor based on Z ($Z = I_{G1}/I_{G2}$) of the upconversion luminescence of UCNPs.

Table 2 Absolute S_a and relative sensitivity S_r of $UCNP_{OA}$ and $UCNP_{AEP}$ at 288 K

Sample	UCNP	UCNP
Capping agent	Oleic acid	AEP
Solvent	Cyclohexane	Water
S_a 10^{-3} [K^{-1}]	2.6	3.0
S_r [% K^{-1}]	1.37	1.38

and relative sensitivity of oleic acid capped UCNP and AEP capped UCNP are shown. It is obvious that the type of ligand and the surrounding medium (cyclohexane and water) has no significant impact on S_a and S_r.

3.5 $UCNP_{Nd}$ as optical probes for thermometry

A big challenge for measurements in "real" biological system are the different optical properties of biological tissues like skin, muscles, connective tissue or vertebral column which only enables a sharp window (700–1000 nm) for optical measurements (see Fig. 8). Based on the water and tissue transmission, which are shown in Fig. 2 and 8, wavelengths around $\lambda_{ex} \sim 800$ nm are more suitable for UCNP based thermometry measurements in contrast to the typical used excitation wavelength of $\lambda_{ex} = 976$ nm, at which also a heating effect by the excitation laser due to water absorption is induced and which is distinctly reduced at $\lambda_{ex} \sim 800$ nm.[13] For UCNP related thermometry the excitation wavelength can be shifted to $\lambda_{ex} \sim 800$ nm upon co-doping with Nd^{3+} (*vide supra*).

The influence of the excitation wavelength on the temperature within the observation volume and near surrounding was monitored using a resistance thermometer in an optical cuvette during the irradiation of the sample with light at $\lambda_{ex} = 795$ nm and 976 nm, respectively (see Fig. 9 and ESI Fig. 6†). It was found that the temperature after irradiation at $\lambda_{ex} = 795$ nm is nearly constant whereas for $\lambda_{ex} = 976$ nm (excitation power ~ 170 mW at both wavelength) an increase in temperature of about $\Delta T \sim$

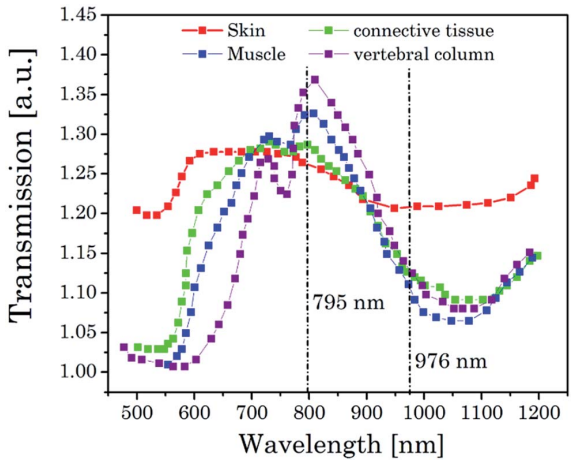

Fig. 8 Transmission spectra of different biological tissue in a spectral range of 500–1200 nm.[13]

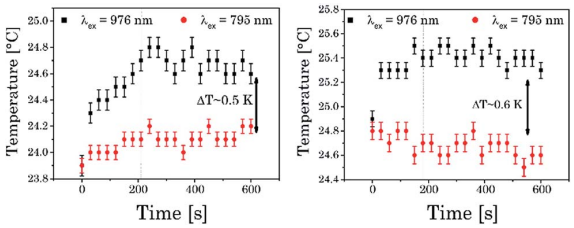

Fig. 9 [Left]: temperature dependence of pure water on the excitation wavelength. [Right]: temperature dependence of $UCNP_{Nd}$ dissolved in water at different at different λ_{ex}.

Table 3 Absolute S_a and relative sensitivity S_r (at 288 K) of $UCNP_{Nd}$. In different solvents excited at 976 nm and 795 nm

λ_{ex} [nm]	976		795	
Solvents	Cyclohexane	Water	Cyclohexane	Water
S_a 10^{-3} [K^{-1}]	2.7	2.9	2.9	3.0
S_r [% K^{-1}]	1.44	1.41	1.31	1.30

0.6 K was found in both cases (pure water and water containing $UCNP_{Nd}$). The maximum ΔT was reached at ~200 seconds of irradiation with $\lambda_{ex} = 976$ nm (since a conventional thermometer was used to measure the temperature change in the nearby bulk phase, the temperature increase at the laser spot is larger).

For biological systems such an increase could induce cellular damage or could significantly influence protein-related processes.[6] On the other hand an excitation wavelength of $\lambda_{ex} = 795$ nm, which is used in the case of $UCNP_{Nd}$, did not show a comparable heating effect in the sample and therefore offers a promising alternative for investigations of biological systems (using UCNP for sensing purposes as well as nano-thermometer). As already shown for UCNP (Fig. 6 and 7) the absolute and relative sensitivity of $UCNP_{Nd}$ with different ligands and different excitation wavelength (λ_{ex}) were calculated based on luminescent spectra at different temperatures (see Table 3). The absolute sensitivity is unaffected by the λ_{ex} applied in the measurement and by the solvent. For the relative sensitivity the same was found when comparing the different solvents (for $\lambda_{ex} = 795$ nm S_r was slightly smaller than for $\lambda_{ex} = 976$ nm). The obtained values for S_r are in good agreement with literature data reported for other host materials.[20]

4. Conclusions

The upconversion luminescence properties of oleic acid and AEP stabilized nanoparticles (UCNP) based on a $NaYF_4$ host matrix, which was doped with Yb^{3+} (UCNP) and Yb^{3+}:Nd^{3+} ($UCNP_{Nd}$) as sensitizer and Er^{3+} as activator, respectively, were studied. The focus of this work was the surface modification with AEP to obtain water soluble nanoparticles as well as to investigate possible thermometry applications based on the temperature sensitivity of the upconversion luminescence. The temperature dependence of different luminescence parameters especially the spectral intensity distribution were analysed for the temperature range of 288 K < T < 328 K. Not only the overall luminescence intensity was dependent on the type of capping agent but also the spectral distribution which is effected as well by the phonon coupling possibilities at the surface of the nanoparticles. On the other hand Nd^{3+} ions as additional co-dopant had no effect on the spectral properties of the Er^{3+} related luminescence.

The possibility to excite the UCNP at $\lambda_{ex} = 795$ nm could be realized by the use of Nd^{3+} ions as new sensitizer with no further impact on the spectral distribution. The interplay between spectral distribution and the temperature dependence of photophysical parameters was further investigated. The intensity distribution (*e.g.*, ratio of the green emission G1 and G2) was strongly depending on the temperature and can be used in thermometry applications. In practical applications, efficient collection of fluorescence signal ensures a high signal to noise ratio (SNR) for improving the sensitivity and resolution of QD, fluorescent dyes or upconversion nanoparticle.[49,50] A variety of highly promising approaches of external optical coupling structures for enhancing the excitation and emission of the luminescence from QD or fluorescent dyes are being investigated using cascaded photonic crystal surfaces, which could also be a powerful tool for application based on upconversion nanoparticles.[49,50] Furthermore, the heating effect due to the irradiated excitation light in the observed sample volume was investigated. Whereas for $\lambda_{ex} = 795$ nm only minor increase of the sample temperature was found, the excitation at $\lambda_{ex} = 976$ nm lead to an increase up to 0.6 K which is rather high especially with regards to possible application in biological tissue. In addition to avoiding heating effects the performance of $UCNP_{Nd}$ are comparable to the regular UCNP with respect to absolute and relative sensitivity of temperature sensing. The intensity ratio of the different Er^{3+} luminescence bands in combination with an excitation wavelength of $\lambda_{ex} = 795$ nm can be envisioned to be used as a nanothermometer, *e.g.*, to measure the temperature spatially resolved in tissues with submicron resolution.

Acknowledgements

We are thankful to Dr C. Günter as well as Dr C. Prietzel and Prof. J. Koetz (University of Potsdam) who performed the structural studies (XRD and TEM measurements, respectively) of the samples.

References

1 X.-D. Wang, O. S. Wolfbeis and R. J. Meier, *Chem. Soc. Rev.*, 2013, **42**, 7834.
2 E. F. J. Ring, *Infrared Phys. Technol.*, 2007, **49**, 297–301.
3 J. B. Weaver, *Nat. Nanotechnol.*, 2010, **5**, 630–631.
4 P. R. N. Childs, R. Greenwood and C. A. Long, *Rev. Sci. Instrum.*, 2000, **71**, 2959–2978.
5 C. D. S. Brites, P. P. Lima, N. J. O. Silva, A. Millan, V. S. Amaral, F. Palacio and L. D. Carlos, *Nanoscale*, 2012, **4**, 4799–4829.

6 G. Kucsko, P. C. Maurer, N. Y. Yao, M. Kubo, H. J. Noh, P. K. Lo, H. Park and M. D. Lukin, *Nature*, 2013, **500**, 54–58.
7 K. Okabe, N. Inada, C. Gota, Y. Harada, T. Funatsu and S. Uchiyama, *Nature Commun.*, 2012, **3**, 705.
8 L. Donner, S. Thompson, M. Kreuzer, G. Baffou and R. Quidant, *Nano Lett.*, 2012, **12**, 2107–2111.
9 J. Yang, H. Yang and L. Lin, *ACS Nano*, 2011, **5**, 5067–5071.
10 F. Vetrone, *ACS Nano*, 2010, **4**, 3254–3258.
11 C. Brites, C. P. P. Lima, N. J. O. Silva, A. Millan, V. S. Amaral, F. Palacio and L. D. Carlos, *New J. Chem.*, 2011, **35**, 1177–1183.
12 G. Chen, H. Qiu, P. N. Prasad and X. Chen, *Chem. Rev.*, 2014, **114**, 5161–5214.
13 K. R. Byrnes, R. W. Waynant, I. K. Ilev, X. Wu, K. Smith, R. Heckert, H. Gerst and J. J. Anders, *Lasers Surg. Med.*, 2005, **36**, 171–185.
14 J. Dong and J. I. Zink, *ACS Nano*, 2014, **8**, 5199–5207.
15 A. Sedlmeier, D. E. Achatz, L. H. Fischer, H. H. Gorris and O. S. Wolfbeis, *Nanoscale*, 2012, **4**, 7090–7096.
16 C. Liu, Z. Gao, J. Zeng, Y. Hou, F. Fang, Y. Li, R. Qiao, L. Shen, H. Lei, W. Yang and M. Gao, *ACS Nano*, 2013, **7**, 7227–7240.
17 B. Sikora, K. Fronc, I. Kaminska, K. Koper, S. Szewczyk, B. Paterczyk, T. Wojciechowski, K. Sobczak, R. W. Minikayev, W. Paszkowicz, P. Stepien and D. Elbaum, *Nanotechnology*, 2013, **24**, 235702.
18 G. Shan, R. Weissleder and S. A. Hilderbrand, *Theranostics*, 2013, **3**, 267–274.
19 J. Shen, G. Chen, A.-M. Vu, W. Fan, O. S. Bilsel, C.-C. Chang and G. Han, *Adv. Opt. Mater.*, 2013, **1**, 644–650.
20 T. Gavrilovic, D. Jovanovic, V. Lojpur and M. Dramicanin, *Sci. Rep.*, 2014, **4**, 4209.
21 A. K. Soni, R. Dey and V. K. Rai, *RSC Adv.*, 2015, **5**, 34999–35009.
22 F. Shi and Y. Zhao, *J. Mater Chem. C.*, 2014, **2**, 2198–2203.
23 C. Liu, H. Wang, X. Zhang and D. Chen, *J. Mater. Chem.*, 2009, **19**, 489–496.
24 K. Liu, X. Liu, Q. Zeng, Y. Zhang, L. Tu, T. Liu, X. Kong, Y. Wang, F. Cao, S. A. G. Lambrechts, M. C. G. Aalders and H. Zhang, *ACS Nano*, 2012, **6**, 4054–4062.
25 B. Voß, J. Nordmann, A. Uhl, R. Komban and M. Haase, *Nanoscale*, 2013, **5**, 806–812.
26 F. Wang, R. Deng, J. Wang, Q. Wang, Y. Han, H. Zhu, X. Chen and X. Liu, *Nat. Mater.*, 2011, **10**, 968–973.
27 J. Shan, M. Uddi, N. Yao and Y. Ju, *Adv. Funct. Mater.*, 2010, **20**, 3530–3537.
28 K. Wu, J. Cui, X. Kong and Y. Wang, *J. Appl. Phys.*, 2011, 110.
29 J. Suyver, J. Grimm, K. Krämer and H. Güdel, *J. Lumin.*, 2005, **114**, 53–59.
30 F. Vetrone, J. C. Boyer, J. A. Capobianco, A. Speghini and J. Bettinelli, *J. Phys. Chem. B*, 2003, **107**, 1107–1112.
31 A. Shalav, B. S. Richards, K. Krämer and H. Güdel, *IEEE Photovoltaic Specialists Conference*, 2005, 114–117.
32 J.-C. G. Bünzli and S. V. Eliseeva, *Chem. Soc. Rev.*, 2010, **39**, 189–227.
33 J. M. F. van Dijk and M. F. H. Schuurmans, *J. Chem. Phys.*, 1983, **78**, 5317–5323.
34 Y. Guyot, H. Manaa, J. Y. Rivoire and R. Moncorgé, *Phys. Rev. B: Condens. Matter Mater. Phys.*, 1995, **51**, 784–799.
35 R. Balda, J. I. Pena, M. A. Arriandiaga and J. Fernández, *Opt. Express*, 2010, **18**, 13842–13850.
36 L. Lu, Q. Nie, T. Xu, S. Dai, X. Shen and X. Zhang, *J. Lumin.*, 2007, **126**, 677–681.
37 A. S. Gouveia-Neto, E. B. da Costa, P. V. dos Santos, L. A. Bueno and S. J. L. Ribeiro, *J. Appl. Phys.*, 2003, **94**, 5678.
38 D. Wawrzynczyk, A. Bednarkiewicz, M. Nyk, W. Strek and M. Somac, *Nanoscale*, 2012, **4**, 6959–6961.
39 L. C. Courrol, I. M. Ranieri, L. V. G. Tarelho, S. L. Baldochi, L. Gomes and N. D. V. Junior, *J. Appl. Phys.*, 2005, **98**, 113504.
40 R. B. Anderson, S. J. Smith, P. S. May and M. T. Berry, *J. Phys. Chem. Lett.*, 2014, **5**, 36–42.
41 D. T. Klier and M. U. Kumke, *J. Phys. Chem. C*, 2015, **119**, 3363–3373.
42 W. T. Carnall, P. R. Fields and B. G. Wybourne, *J. Chem. Phys.*, 1965, **42**, 3797–3806.
43 A. Shalav and B. S. Richards, *IEEE Transactions on Electron Devices*, 2007, **54**, 2679–2684.
44 L. H. Fischer, G. S. Harms and O. S. Wolfbeis, *Angew. Chem., Int. Ed.*, 2011, **50**, 4546–4551.
45 C. T. Xu, Q. Zhan, H. Liu, G. Somesfalean, J. Qian, S. He and S. Andersson-Engels, *Laser Photonics Rev.*, 2013, **7**, 663–697.
46 Y. Tian, B. Tian, C. Cui, P. Huang, L. Wang and B. Chen, *Opt. Lett.*, 2014, **39**, 4164–4167.
47 M. Debasu, *Adv. Mater.*, 2013, **25**, 3254–3258.
48 L. Hao and L. Y. Wang, *Chin. Sci. Bull.*, 2013, **58**, 4051–4056.
49 W. Chen, K. D. Long, H. Yu, Y. Tan, J. S. Choi, B. A. Harley and B. T. Cunningham, *Analyst*, 2014, **139**, 5954–5963.
50 Z.-H. Chen, Y. Wang, Y. Yang, N. Qiao, Y. Wang and Z. Yu, *Nanoscale*, 2014, **6**, 14708–14715.

3 Discussion

Upconversion Luminescence versus Crystal Phase Lattice

In a first set of experiments $NaYF_4$ was used as host lattice to examine the impact of lattice phase on the upconversion luminescence properties of Yb^{3+} and Er^{3+} systems. A hydrothermal type of synthesis was performed under mild conditions to generate the pure α-phase, which is one of the three possible crystal phases of $NaYF_4$. The pure β- and high temperature α-phase as well as mixture phases of different composition were achieved by annealing the pure α-phase at different temperatures 200 °C < T_{an} <700 °C. Hence, crystal phase parameters of the α- and high temperature α-phase were similar. The phase composition, particle size and morphology were studied in detail by using XRD, DLS and TEM/REM (shown in Figure 3.1). The favored intercalation of Yb^{3+} and Er^{3+} ions into the host lattice or lattice distortion was not expected, due to the nearly similar covalent radii of the lanthanides and Yttrium. ICP-OES investigations support this hypothesis (see Chapter 2.1/page 16). The absolute upconversion luminescence emission intensity as well as the spectral intensity distribution of the UCNP annealed at different temperature ($UCNP_{an}$) was altered depending on the crystal lattice. Especially the phase transition from α- to β-phase as well as the back transition to the α-phase was highly pronounced in the luminescence spectra in form of an abrupt high increase of luminescence intensity.

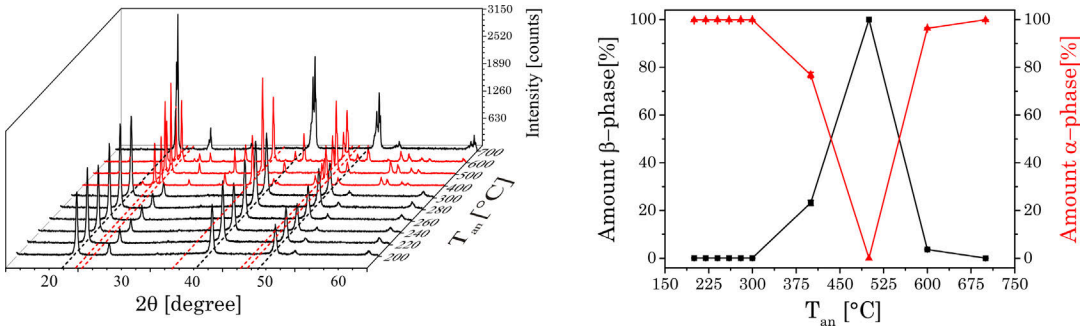

Figure 3.1: (left) X-ray diffraction patterns of $UCNP_{an}$ after annealing between 200 °C < T_{an} < 700 °C for 5 h. The black dotted lines correspond to the position of reflexes of the cubic phase whereas the red dotted lines correspond to the reflexes of the hexagonal phase. (right) Amount of α- and β-phase in correlation with temperature of the thermal treatment, calculated from the intensity of the different XRD reflexes of the crystal phases.

Depending on the luminescence emission band an increase of at least 6 times was observed. Also the integrated luminescence intensity ratios of G1/G2 and G2/R were well correlated with amount of β-phase, as shown in Figure 3.2. Only the G2/R ratio is

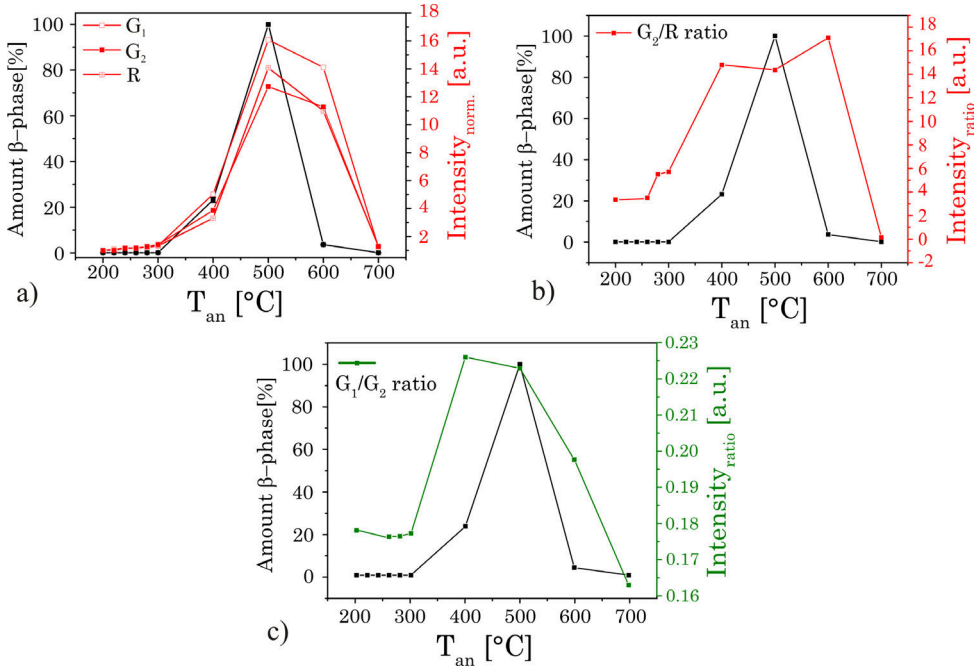

Figure 3.2: (a) Alteration in the (quasi) steady state intensity of different luminescence bands with annealing temperature T_{an}. The ratio G2/R (b) and G1/G2 (c) based on the integrated steady state luminescence intensity of these emission bands and the amount of hexagonal phase, both as a function of temperature T_{an}. The amount of β-phase was calculated based on XRD measurements.

significantly influenced by crystal phase, due to the different population mechanisms of the corresponding energy level, which will be discussed in detail (*vide infra*). The luminescence decay kinetics of G2 and R showed a complex time dependence with an initial rise in luminescence intensity and a bi-exponential like decay kinetic. This might result from contributions of Er^{3+} ions located in different chemical environments like surface *vs.* volume effects or amorphous domains. From the luminescence decay times for the emission bands G2 and R the correlation between the gradual phase transition from α- to β-phase and back to α- phase becomes obvious. Here, the change in the decay time (gradual increase for both decay components) is not that abrupt and can be seen at already minor amounts of β-phase in contrary to the results of the (quasi) stationary luminescence investigations. Nevertheless, the results are in very good agreement with the already presented spectroscopic data. This might indicate a beginning phase transition at lower T_{an} than predicted from the XRD calculations. This is also reflected by TRANES analysis, which was performed in order to pinpoint the influence of the

lattice on the luminescence upconversion (see Chapter 2.1/page 22). Here, in Figure

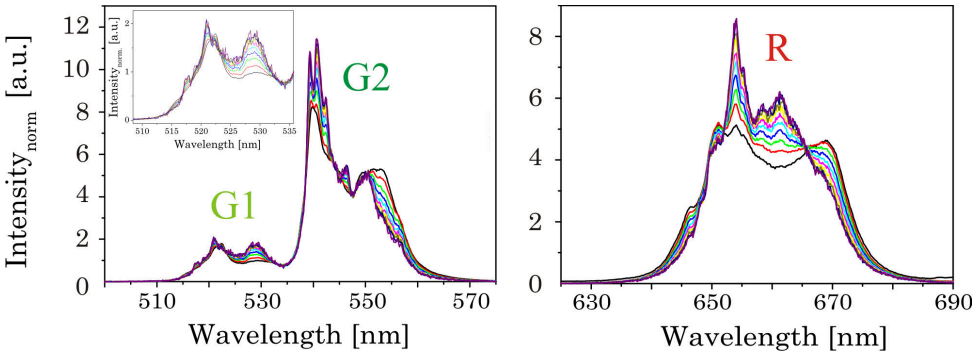

Figure 3.3: (left) TRANES of annealed $UCNP_{an}$ (300 °C) for G1 and G2 luminescence as well as (right) of R luminescence are shown (λ_{ex} = 976 nm). (left inset) Enlarged representation in G1-related TRANES showing the isoemissive points in detail. The delay after the laser pulse was varied between 0 ms and 2000 ms (displayed by the colors in 120 ms steps).

3.3 significant time-dependent variations in the spectral intensity distribution were revealed. Additionally, isoemissive points were found at λ_{em} = 516.8 nm, 521.8 nm and 532.2 nm for G1 as well as for R at λ_{em} = 651.0 nm and 665.8 nm, which can be attributed to Er^{3+} ions in a different chemical environment *e.g.*, located in α- and β-phase. The calculated relative amount of cubic and hexagonal phase based on a spectral decomposition of the recorded luminescence emission spectra at a delay time of 0 µs supported the results of the (quasi) steady state investigations. Where the phase transition from α- to β-phase occurs rapidly for 300 °C < T_{an} < 500 °C (similar to the XRD calculations, see Figure 3.1). For a delay time of 500 µs the calculated relative crystal phase fraction suggested itself a gradual transformation of cubic into hexagonal phase in a temperature range of 200 °C < T_{an} < 400/500 °C depending on the luminescence emission band (see Figure 3.4). The different results of the calculations depending on the delay time are caused by the longer rise kinetic of the luminescence intensity in hexagonal phase in comparison to the cubic phase. Here, the luminescence emission of Er^{3+} ions located in the hexagonal phase will be overshone by the luminescence emission of the Er^{3+} species located in the cubic phase. The same explanation is true for contrary results of the steady state and the decay kinetic measurements. Finally, TRANES analysis were shown to be a very sensitive tool for the determination of the lattice phase composition of UCNP. The sensitivity was found to be even higher as for standard analytical methods like XRD in the special case of UCNP. A change in the micro environment of the lanthanide entailed a distinct impact on the upconversion luminescence, whereas small crystallites will not be contribute to the overall XRD signal.

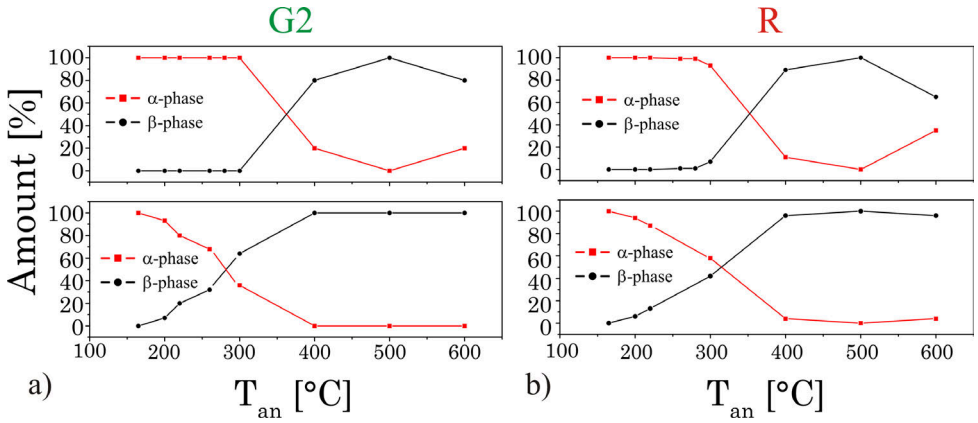

Figure 3.4: Variation of the amount of different crystal phases calculated from TRANES analysis at delay times after the laser pulse (top: 0 µs and bottom 500 µs) for the emission bands (left) G2 and (right) R.

Insight View into Upconversion Mechanism

The exact mechanism behind the structure/crystal lattice induced alteration in the photophysical properties of UCNP were the scope of this investigation. The crystal lattice will influence several parameters with direct and indirect effects on the lanthanides. First of all, the distances between the lanthanides in the host lattice could be varied, leading to an alteration of distance and efficiency of the energy migration. Furthermore, the relative position of the energy levels of the different lanthanides could be affected, resulting in changes in their inter- and intra-lanthanide energy transfer efficiencies. The similar effects could be induced by variations of the phonon energy or lattice vibrations. Temperature dependent measurements are a suitable technique to discover contributions of phonon coupling and/or thermal agitation based on a targeted deactivation of these processes. The luminescence spectra of the UCNP for the temperature range of 4 K $< T <$ 209 K (see Figure 3.5) provide a first clue about the upconversion cascade mechanism and if phonon coupling and/or thermal agitation could be expected: (i) The luminescence intensity of the G2 -and R-related emission bands initially increased with decreasing temperature until a maximum is reached at $T = 210$ K. Upon further lowering the temperature the emission intensity is decreased. (ii) The luminescence intensity of the G1-related emission band gradually decreased with decreasing temperature and finally disappeared completely at a certain temperature (see Chapter 2.2/page 32).
In Yb^{3+} the $^2F_{5/2}$ energy level consists of a multiplet of two energy crystal field components $^2F_{5/2}|0\rangle$ and $^2F_{5/2}|1\rangle$. Due to the very low energy difference of 39 cm^{-1} (calculated, see Chapter 2.2/page 34) between the two Stark levels, a very high Boltzmann coefficient (at RT) of $N_1/N_0 = 0.84$ was found in the thermal equilibrium. Furthermore, a better energy matching between the energy levels of Yb^{3+} and Er^{3+} is given for the $^2F_{5/2}|1\rangle$ resulting in a more efficient energy transfer between these lanthanide

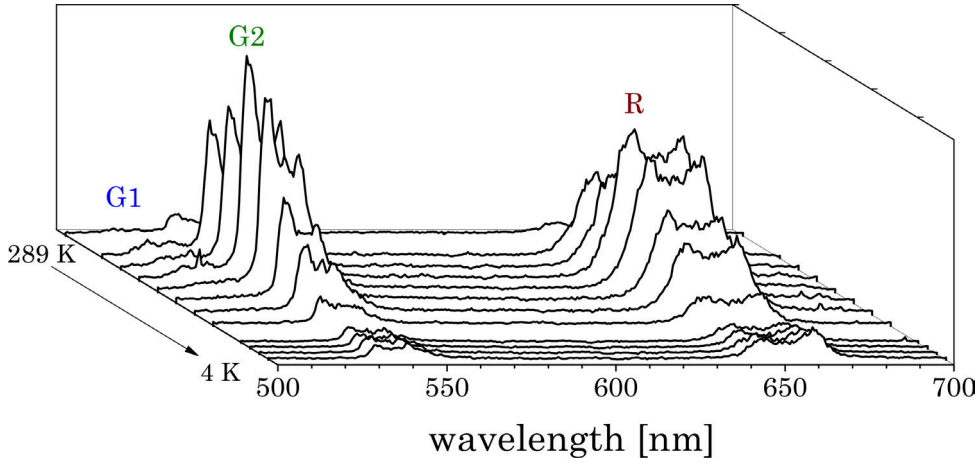

Figure 3.5: Upconversion luminescence emission spectra of Gd^{3+}-doped (80 mol%) UCNP at different temperatures 4 K $< T <$ 289 K (λ_{ex} = 976 nm).

ions. However, as the excitation cross section of the $^2F_{5/2}|1\rangle$ Stark level is much lower than for the $^2F_{5/2}|0\rangle$ level, the thermal population of $^2F_{5/2}|1\rangle$ is the determining factor for the overall process of generating upconversion luminescence.
The difference in the temperature dependence of the G1 and G2 emission bands is strongly connected to the population pathways of the related energy levels shown in Scheme 4 with the corresponding Stark levels calculated from the excitation and emission spectra of the UCNP. The population of the green emitting levels G1 and G2 ($^2H_{11/2}$ and $^4S_{3/2}$) usually occurs by successive energy transfer processes from the Stark level $^2F_{5/2}|1\rangle$ of Yb^{3+} ions to the Er^{3+} ions, exciting them first to the $^4I_{11/2}$ level and in a second step to the $^4F_{7/2}$ energy level.

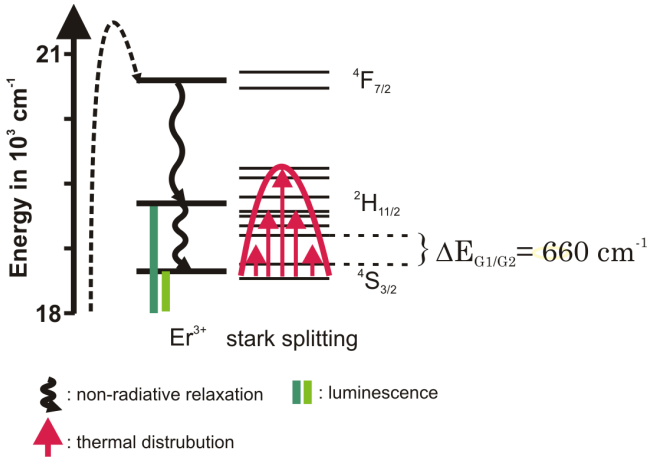

Scheme 4: Close-up of energy levels related to G1 and G2 emission in Erbium.

Followed by a non-radiative relaxation step the Er^{3+} ion deactivates to the $^2H_{11/2}$ and – due to the moderate energy gap between $^2H_{11/2}$ and $^4S_{3/2}$ states (about 660 cm^{-1}) – the Er^{3+} ions can relax fast to the $^4S_{3/2}$ state. Finally, the $^2H_{11/2}$ level is thermally repopulated via thermal agitation, which becomes more effective with increasing temperature. The correlation of the luminescence intensity ratio ($R = I_{G1}/I_{G2}$) and the temperature is given by an Arrhenius-type of equation, which further provided access to the energy gap between the energy levels $^2H_{11/2}$ and $^4S_{3/2}$. Additionally, a gradual decrease of the energy gap was induced by doping Gd^{3+} ions into the host lattice and further entailed the lattice structure of the UCNP under investigation (shown in Figure 3.6). Associated with the decreased energy gap an enhanced population of the energy level $^2H_{11/2}$ was found, due to the thermal equilibrium, leading to an increasing luminescence intensity G1 relative to G2. In summary all results underline the importance of thermal population processes for various steps in the upconversion mechanism for UCNPs with Er^{3+} as activator. Not only intra lanthanide processes responsible for the intensity distribution of the luminescence are affected, but also inter-lanthanide processes responsible for the initial step in the cascade upconversion mechanism and thus for the efficiency of the upconversion in general.

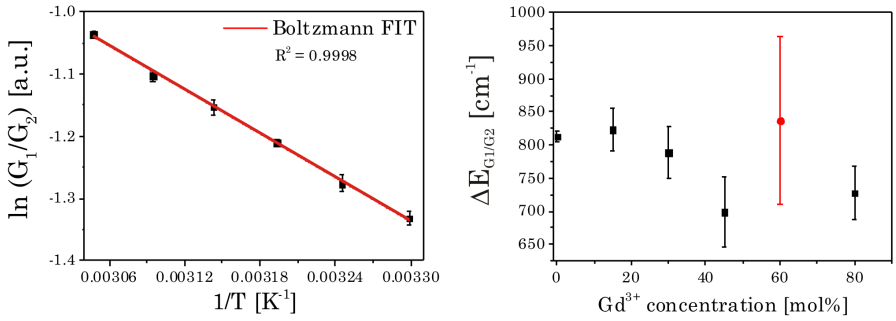

Figure 3.6: (left) Analysis of UCNP (without Gd^{3+} doping) temperature dependence of the logarithm of the integrated emission intensity ratio of bands G1 and G2. (right) Energy gap $\Delta E_{G1/G2}$ as a function of Gd^{3+} concentration.

Whereas only one single route for the population of the $^2H_{11/2}$ and $^4S_{3/2}$ energy levels was found, four possible population pathways for the energy level $^4F_{9/2}$ are possible: two 2-photon processes and two 3-photon processes. Here, the $^4I_{11/2}$ level of Er^{3+} is the starting point followed by successive energy transfer processes from the Stark level $^2F_{5/2}|1\rangle$ of Yb^{3+} to Er^{3+} ions. First, the $^4F_{7/2}$ level can be populated by a second energy transfer from an excited Yb^{3+} ion, followed by several non-radiative relaxation processes to the $^2H_{11/2}$ or $^4S_{3/2}$ and finally to the $^4F_{9/2}$ energy level (2-photon process A). Alternatively the $^4F_{9/2}$ level can be populated after non-radiative relaxation from the $^4I_{11/2}$ to the $^4I_{13/2}$ level followed by an energy transfer from the sensitizer Yb^{3+} to the Er^{3+}, leading also to the red emission R (2-photon process B). In a typical 3-photon process, the $^4F_{7/2}$ energy level of one Er^{3+} ion is populated by two energy

transfer steps from excited Yb^{3+} ions, whereas a second Er^{3+} ion is populated in the $^4I_{11/2}$ energy level via one energy transfer step from Yb^{3+}. In this special constellation, which is favored for high Er^{3+} ion concentration, a cross relaxation between the two excited Er^{3+} ions occurs, leading in a population of the $^4F_{9/2}$ energy level for both Er^{3+} ions (3-photon process A). In the 3-photon process B, the $^4S_{3/2}$ energy level of the Er^{3+} ion is populated by two energy transfer steps from excited Yb^{3+} ions. In the following, the $^4I_{13/2}$ level of Er^{3+} can be populated via an energy back-transfer (BET) from the $^4S_{3/2}$ level of Er^{3+} to neighboring Yb^{3+} ions. Finally, the population of the $^4F_{9/2}$ energy level is analog to the 3-photon process A by a subsequent energy transfer from excited Yb^{3+} ions to the $^4I_{13/2}$ level of Er^{3+}. As a result, the population of the $^2H_{11/2}$ and $^4S_{3/2}$ levels are in strong competition with the $^4F_{9/2}$ level.

In Figure 3.7 (left) normalized Raman spectra of the α- and β-phase of UCNP are

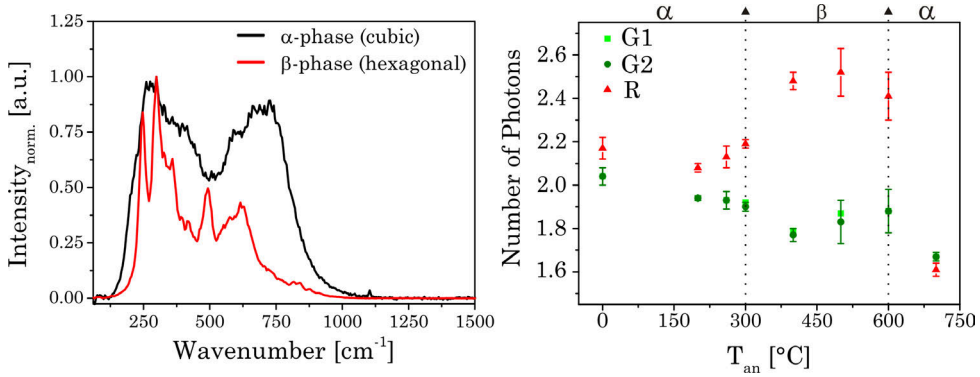

Figure 3.7: (left) Normalized Raman spectra of α- and β-phase UCNP. (right) Number in photons (n-values) determined for the emission bands G1, G2 and R for UCNP annealed at different T_{an}.

shown with significant differences in spectra distribution. Especially in the α-phase high-phonon vibrational bands $\nu > 700\text{cm}^{-1}$ are obvious, which are only weakly presented in β-phase. The high-phonon vibrational bands are based on combination vibrations as well as higher harmonic vibrations. Here, the decrease in these bands leads to less efficient 2-phonon processes A and B, as these are based on phonon coupled relaxation processes, for which energy gaps of nearly 3000 cm^{-1} has to be overcome. The probability for an efficient bridging of the energy gaps is much higher for a phonon coupling with only a few high energy vibrational bands compared to a phonon coupling supported process involving numerous low energy vibrational bands. As a result, the probability of populating the $^4F_{9/2}$ energy level is decreased and the $^2H_{11/2}$, $^4S_{3/2}$ levels are favored. The observed alterations in the Raman spectra are well correlated with the luminescence emission spectra. Here, a distinct increase in the ratio of the integrated luminescence intensity of G2/R is shown, also indicating for which phase a higher and more favored population of $^2H_{11/2}$, $^4S_{3/2}$ levels occurs (see Chapter 2.1/page 21).

Furthermore, laser power dependent luminescence measurements was performed. There-

from an easy access to the number of photons n required for the population of a certain energy level is given, as the UC luminescence intensity (I_{UC}) is proportional to the n-th power of excitation light intensity (I_{IR}) (see Equation 1).

$$I_{\mathrm{UC}} \sim I_{\mathrm{IR}}^{n} \tag{1}$$

n is the number of absorbed NIR photons per visible photon emitted and can be obtained from the slope of $\log_{10}(I_{\mathrm{UC}})$ versus $\log_{10}(I_{\mathrm{IR}})$ analysis. In Figure 3.7 (right) n was determined for the emission bands G1, G2, and R for UCNP annealed at different T_{an}. The n-value for the R band increased from $n \approx 2.1$ ($T_{\mathrm{an}} = 0$ °C) to $n \approx 2.5$ ($T_{\mathrm{an}} = 600$ °C). A distinct difference in the n-values is found for the α-phase ($T_{\mathrm{an}} = 0$ °C) and the β-phase ($T_{\mathrm{an}} = 400$ °C - 600 °C), but already at $T_{\mathrm{an}} < 400$ °C (representing a mixture of α-phase and low β-phase content) slight but steady changes in the n-values was observed. From this it can be concluded that the 2-photon processes A and B are most favored in the α-phase as population mechanism of the $^4\mathrm{F}_{9/2}$ energy level, whereas with increasing amount of β-phase the 3-photon processes A and B are becoming more important (see Figure 3.7 (right)). These results confirm the need of high-phonon vibrational bands for the population of $^4\mathrm{F}_{9/2}$ via a 2-photon process. In contrast, n-value for G1 and G2 is slightly, but steadily decreased with increasing annealing temperature from $n \approx 2$ ($T_{\mathrm{an}} = 0$ °C) to $n \approx 1.7$ ($T_{\mathrm{an}} = 700$ °C). For the green emission bands G1 and G2 theoretically $n = 2$ is expected and the observed decrease of n with increasing T_{an} points toward a kind of saturation effect. This saturation effect is attributed to the lower population efficiency of the $^4\mathrm{F}_{9/2}$ energy level, whereas the population probability of the energy levels resulting in the emission bands G1 and G2 is distinctly increased. Finally, the results shown point out that the upconversion mechanism is very complex, but can be well understood as a sum of closely related coupled single steps, which directly influences each other.

Upconversion Nanoparticle as Nanothermometer

Based on the excellent correlation of the integrated luminescence intensity ratio $I_{\mathrm{G1}}/I_{\mathrm{G2}}$ and the temperature, which can be described by an Arrhenius-type equation, the co-doped (Yb^{3+} and Er^{3+}) UCNPs were further modified for an application as nanothermometer (see Figure 3.8). To reach a higher penetration depth and higher signal to noise ratio in biological tissue, *e.g.*, skin or muscle, the co-doped UCNPs were additionally doped with Nd^{3+} ions to have access to a lower excitation wavelength of $\lambda_{\mathrm{ex}} = 795$ nm. Another drawback of the origin excitation wavelength of $\lambda_{\mathrm{ex}} = 976$ nm chosen so far is the distinct heating of the sample about $\Delta T \approx 0.6$ K, which was found in pure water and water containing UCNP, see Figure 3.9. Hence, at $\lambda_{\mathrm{ex}} = 795$ nm no change in temperature after irradiation (excitation power ≈ 170 mW, similar at both wavelength) was found. Here, it was shown that Yb^{3+} can act as a "relay" between the "new" sensitizer Nd^{3+} and the activator Er^{3+}, whereas the subsequent energy transfer steps and relaxation processes from Yb^{3+} to the Er^{3+} are identical to the co-doped UCNPs. On one hand no significant differences in the shape, fine structure and peak

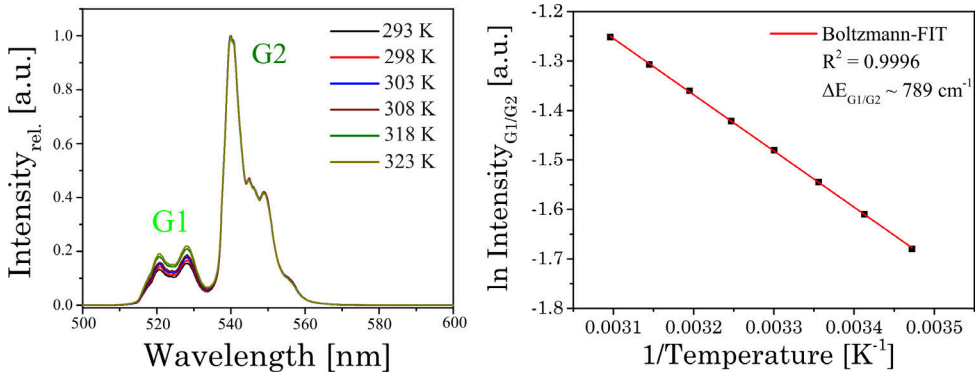

Figure 3.8: (left) Normalized upconversion emission spectra of co-doped UCNP excited at λ_{ex}= 976 nm at different temperature. (right) Analysis of the integrated luminescence intensity ratio I_{G1}/I_{G2}.

ratio in the upconversion emission spectra were found at both excitation wavelengths (λ_{ex}= 795 nm and λ_{ex}= 976 nm). On the other hand the absolute luminescence intensity is much lower (only 10 percent) for the excitation at λ_{ex}= 795 nm, although the extinction coefficient of Nd^{3+} at λ_{ex}= 795 nm is higher than for Yb^{3+} at λ_{ex}= 976 nm. The lower luminescence intensity resulting from excitation at λ_{ex}= 795 nm is a consequence of an efficient energy transfer from Er^{3+} to Nd^{3+} ions as well as an additional initial energy transfer from Nd^{3+} to Yb^{3+}, which offers the possibility for a higher number of non-radiative deactivation pathways (see Chapter 2.3/page 44).

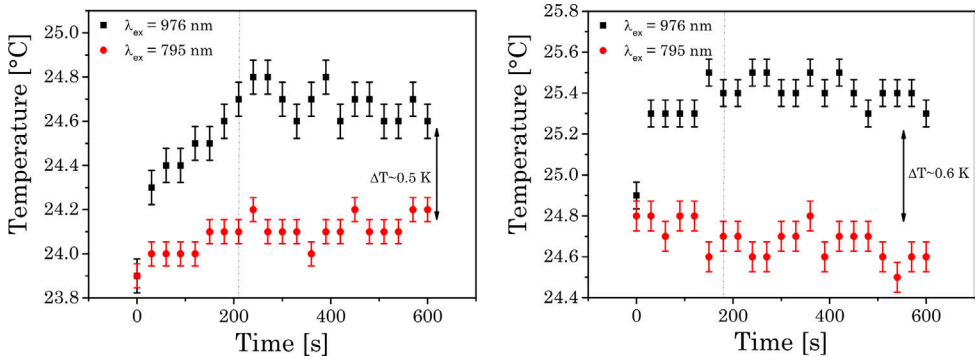

Figure 3.9: Temperature dependence of pure water (left) and tri-doped UCNP dissolved in water (right) depending on different excitation wavelength measured with a conventional thermometer.

The required water solubility of the tri-doped UCNPs was achieved using AEP as new capping agent. Here, the new chemical environment at the surface of the nanoparticles leads to a distinct decrease in G1/G2:R intensity ratio, based on different phonon coupling processes. The AEP functionalized UCNPs are colloidal stable

in watery solution for several month without any agglomeration or aggregation effects. Additionally, no alteration in the photophysical properties could be found. By comparing the absolute sensitivity S_a and relative sensitivity S_r of tri-doped UCNPs (at 288 K), almost no differences were found for S_a independent of the different solvents like cyclohexane and water, capping agent or excitation wavelength λ_{ex}= 795 nm and λ_{ex}= 976 nm. For S_r small differences were found depending on the excitation wavelength with typical values of $S_r = 1.44\%\ K^{-1} \pm 0.2\%\ K^{-1}$ for λ_{ex}= 976 nm and $S_r = 1.31\%\ K^{-1} \pm 0.2\%\ K^{-1}$ for λ_{ex}= 795 nm (see Chapter 2.3/page 46).

4 Summary and Conclusion

4.1 Summary

In the presented manuscripts the development and photophysical as well as structural characterization of three types of upconversion luminescent nano-probes with $NaYF_4$ as host lattice was described. All described UCNPs are using lanthanides as the luminescent center piece with Yb^{3+} ions as sensitizer and Er^{3+} ions as activator which was the simplest type of UCNP under investigation. In the two other types of UCNP additional lanthanides like Gd^{3+} and Nd^{3+} were added. The upconversion process itself is based on a very complex interplay of numerous different energy transfer steps and interactions between lanthanides linked via phonon coupling. The presented work unveils how parameters like temperature, ratio of lanthanides, crystal lattice and excitation power density influence the upconversion process and more important how to control the upconversion luminescence properties in a defined manner. A variable luminescence setup for multiparameter luminescence studies was built up and established as a suitable tool to gain detailed information on the spectroscopic parameters of interest and to derive structural information.
In the first part, the impact of the structural environment of the lanthanides on the upconversion luminescence properties was characterized by using $NaYF_4$ nanoparticles co-doped with Er^{3+} and Yb^{3+} in different ratios of α- and β-phase. It could be shown that variations in the crystal lattice phase subsequently induce an increase in the absolute upconversion luminescence intensity and an increasing $I_{G/R}$ ratio of the UCNP determined by steady-state and time-resolved measurements. Inter-lanthanide energy transfer in the host lattice was identified to be supported by different phonon energy coupling mechanisms as one of the key processes to design the spectroscopic properties of UCNPs. This was demonstrated by correlating Raman spectroscopy and steady-state measurements at various laser power densities. Analyzing the luminescence properties at different laser power densities enabled furthermore to understand how certain energy transfer routes are favored. It turned out that TRANES analysis proved to be a superior luminescence technique as sensitive tool, to monitor the phase transition of the host lattice, especially of resolving even small contributions of cubic and hexagonal phases, even by rather small proportions, where neither XRD nor Raman spectroscopy gave clear indication for a change in the lattice phase (see Chapter 2.1).
In the second part, the nanoparticle system $NaYF_4$ co-doped with Yb^{3+} and Er^{3+} was extended with a third lanthanide ion (Gd^{3+}) in order to further tailor the UCNP properties. By TEM, DLS and XRD measurements could be shown that a defined control of fundamental particle properties like crystal lattice phase and particle size

could be achieved by doping different amounts of Gd^{3+} into the lattice. A significant increase in the overall luminescence intensity was found for 15 mol % Gd^{3+}, while for the higher or lower concentration the luminescence intensity drops down due to the competing effects of crystal lattice change to the β-phase on the one hand, and alteration of particle volume to surface ratio change to a higher relative surface area on the other. This was also supported by the luminescence decay kinetics and steady-state measurements. A strong emphasis was layed on the temperature dependence (4 K to 330 K) of different luminescence parameters (spectral intensity distribution, luminescence decay kinetics) for a detailed understanding of intra-molecular deactivation (4 K to 250 K) and different population processes (288 K to 330 K) involved for the sensitizer (Yb^{3+}) and activator (Er^{3+}). Three major facts were discovered: i) within different cascades of energy transfer steps between Yb^{3+} and Er^{3+} electron-phonon coupling is very important in order to bridge energy gaps between activator and sensitizer. This was demonstrated by changing the crystal lattice by Gd^{3+} doping and tempering UCNP without any Gd^{3+}, where the same correlation of temperature and crystal lattice phase was found. ii) the $^2F_{5/2}$ energy level of Yb^{3+} was found to consist of two components (Stark levels) $^2F_{5/2}|0\rangle$ and $^2F_{5/2}|1\rangle$ with a very low energy gap of 39 cm^{-1}. The Stark level $^2F_{5/2}|0\rangle$ has a significant higher excitation cross section at $\lambda_{ex} = 976$ nm, whereas the energy transfer from $^2F_{5/2}|1\rangle$ level of Yb^{3+} to $^4I_{11/2}|0\rangle$ of Er^{3+} is much more efficient. For the overall upconversion luminescence the thermal population of the $^2F_{5/2}|1\rangle$ Stark level is crucial process. iii) the population of the $^2H_{11/2}$ level of Er^{3+} is mainly based on thermal repopulation from the $^4S_{3/2}$ level of Er^{3+} due to the relative moderate energy gap of 700 cm^{-1}. As a result, the luminescence intensity ratio of G1 and G2 will be dependent on the temperature, whereas the G1 band will vanish at temperatures below 160 K. The correlation of the luminescence intensity ratio and the temperature can be described by an Arrhenius-type equation (Section 2.2) and grants the access to the average energy gap of $^2H_{11/2}$ and $^4S_{3/2}$ level. This approach lays the foundation of further applications as a nanothermometer, *e.g.*, to measure the temperature spatially resolved in tissues (see Chapter 2.3).
In the final part the focus was placed on the surface modification of the UCNPs with AEP to obtain water soluble nanoparticles as well as to investigate possible thermometry applications based on the revealed (see Chapter 2.3) temperature sensitivity of the upconversion luminescence intensity distribution (*e.g.*, ratio of the green emission G1 and G2). Here, the results of the steady-state fluorescence measurements showed that overall luminescence intensity as well as the spectral distribution, which is effected by the phonon coupling possibilities at the surface of the nanoparticles, was dependent on the type of capping agent. In order to overcome the challenges for measurements in biological tissues, *e.g.*, higher penetration depth and decreasing heating effects, the nanoparticle system $NaYF_4$ co-doped with Yb^{3+}, Er^{3+} and Gd^{3+} was extended with a fourth lanthanide ion (Nd^{3+}) as new sensitizer, where Yb^{3+} ions acts now as a kind of "relay" lanthanide. This offers the possibility to excite the UCNP at $\lambda_{ex} = 795$ nm with no further impact on the spectral distribution. The influence of the excitation wavelength on the temperature within the observation volume and near surrounding was monitored. Among the two excitation wavelength, for $\lambda_{ex} = 795$ nm only a minor

increase of the sample temperature could be observed, whereas the excitation at λ_{ex} = 976 nm leads to an increase up to 0.6 K, which is rather high, especially with regard to possible application in biological tissue. Another benefit is the high performance with respect to absolute and relative sensitivity of temperature sensing of Nd^{3+}-doped UCNPs, which is comparable with the "regular" UCNPs excited at λ_{ex} = 976 nm.
Three synthesis methods depending on the attempt of the respective central spectroscopic questions could be successful realized. $NaYF_4$ based upconversion nanoparticles doped with several combination of lanthanides (Yb^{3+}, Er^{3+}, Gd^{3+} and Nd^{3+}) were synthesized successfully using a hydrothermal synthesis method under mild conditions as well as co-precipitation and high temperature co-precipitation techniques. To fulfill the high quality demand for further biomedical approaches the high temperature co-precipitation method was used as a promising candidate. All obtained nanoparticles were predominantly high crystalline, with a particle sizes between 30 nm and 275 nm depending on the type of synthesis and capping agent. Different fractions of the synthesized nanoparticles were annealed at different temperatures between 200 °C and 700 °C. Furthermore, surface modifications of the prepared UCNP were successfully performed under mild conditions using the ligand exchange procedure, whereas colloidal stable nanoparticles in organic solvents like toluene, chloroform or cyclohexane as well in water were obtained. Structural information was gathered by means of XRD, TEM, DLS, Raman spectroscopy and ICP-OES. The results were discussed in detail in relation to the findings from steady-state and time-resolved room temperature luminescence measurements (see Chapter 2.1 and 2.2).

4.2 Conclusion

The skilful combination of structural investigations and mechanistically elucidation of the upconversion luminescence mechanisms of nano-scaled $NaYF_4$ based UC-materials provide an appropriate contribution to bring UCNPs into biomedical application.
In terms of mechanistical elucidations of the upconversion process the understanding of the role of phonon modes was extended, based on a combined analysis of Raman and stationary luminescence (at various excitation power density) measurements. In comparison to the published literature, especially that high energy phonons play an important role for upconversion luminescence in α-phase $NaYF_4$ UCNP was unveiled. Overall, nearly every partial step of upconversion mechanism from the energy transfer between the lanthanides, like from Yb^{3+} to Er^{3+} ions, as well as the inter- and intra-lanthanide processes are determined by phonon coupling and/or thermal population, which can be declared as a key process. Furthermore, analyzing the impact of the excitation power density on upconversion luminescence could be figured out as an underrated tool not only for UC mechanism studies, but also for the awareness to deal with the careless handling of comparing scientific results of literature data in that field of research. Luminescence spectroscopy in general, and TRANES in particular, proved

to be a powerful tool to assess the structure. TRANES was employed to monitor the α- to β-phase transition as well as the back-transfer in detail. Even slight changes in the crystal phase of the sample can be monitored where established techniques like XRD (*e.g.*, Rietveld analysis) or high resolution TEM are only able to give a very rough overview of the phase transfer. It can be used as a great tool to monitor the phase composition of UCNPs *in situ* during synthesis with exceptional sensitivity.
The potential of UCNPs for biological applications is high, whereas the "standard" UCNP design has to be attuned according to the special conditions in the biological matrix. The first step into this direction was done by using Nd^{3+} ions as a new sensitizer ion in tri-doped $NaYF_4$ UCNPs. This approach showed a better biocompatibility due to a lower impact on biological tissue and higher penetrability for the excitation light, whereas the absolute and relative temperature sensitivity is comparable to the origin of the "standard" UCNP excited at λ_{ex}= 976 nm.

4.3 Outlook and Vision

The versatility and the excitation in the optical window of biological tissue make lanthanide based UCNPs to an exciting material class for biomedical application. The research on that topic has to be extended to a toolbox (first promising research efforts by Chan *et. al*[79]) with the scope of mass production, suitable surface modification strategies and improvement of the nanoparticle design, *e.g.*, core/shell nanoparticles. In terms of mass production in "kg scale" or optimizing the synthesis in general terms a lot of challenges like lowering the synthesis temperatures or reaction time as well as new types of capping has to be done for a real commercial approach. Nowadays the synthesis with oleic acid and octadecene at high temperature above 300 °C for at least 60 minutes has been the most common technique for several years, with no alternative in sight.[43,80,81] TRANES could be considered as new suitable monitoring technique, in form of an internal element of quality assurance for the development of new types of synthesis.
The main challenge up to today is a simple and cheap way of surface modification. Two types of surface modification categories of oleic acid capped nanoparticles are commonly used.[80] Ligand exchange methods using tetra-fluoroborate (BF_4^-), trisodium citrate, poly(acrylic acid sodium salt) (PAA), poly(ethylene-oxide)-10-OH with a terminal phosphate ester (PEG-PA) or layer-by-layer coating with poly(sodium 4-styrenesulfonate) (PSS) and poly(allylamine hydrochloride) (PAH) on an initial citrate layer as well as the addition of an amphiphilic layer like poly(isobutylene-alt-maleic anhydride) (PMA) modified with dodecylamine, PEG-PMA or PEGylated phospholipids belong to the standard techniques and enable the transfer into polar or hydrophilic media. These surface ligands are mainly bound by electrostatic interactions and suffered from the similar effect that the number of surface groups or binding sites can vary depending on the concentration in the surrounding media. During that process the surface ligands of the nanoparticles could be unattached. As a result, the evidence of target molecules or quantitative analysis of substances as well as the colloidal

stability of the nanoparticles itself would mainly depend on the surrounding media of the nanoparticle, where the detection takes place. A breakthrough in this field could be an encapsulation technique using the amphiphilic cross-linkable diblock co-polymers poly(isoprene)-b-poly(ethylene glycol) in combination with poly(isoprene)-diethylentriamine, which was already shown in the case of quantum dots.[82,83] Due to the covalent attachment of the functional groups or molecules via radical crosslinking of the hydrophobic PI-layer with the dibloc co-polymer provides excellent long term stability as biological probes.
Additionally, new types of nanoparticle design in form of core/shell nanoparticles with single or multi shell architecture[46,47,84,85] are now accessible. Depending on the shell material, several types of core/shell system are possible. The most interesting ones are the amorphous shell, e.g., silica shell, where drugs could be intercalated and the upconversion luminescence would be enhanced by means of surface passivation.[80,86] Furthermore, an active shell with intentionally added dopants combines the benefit of a suppressed surface-quenching effect with an increased capacity for high-level doping. They can offer attractive optical properties not accessible by other types of core/shell structures.[43,48,87] For the special case of an upconversion based nanothermometer the research should be focused on an $NaYF_4$ based active shell with Yb^{3+} and Nd^{3+} ions, whereas the core made of $NaYF_4$ should be doped with Yb^{3+} and Er^{3+} ions. The energy transfer between core and shell would be realized by the highly efficient energy transfer between Yb^{3+} ions over a distance of several nanometers.[78] The spatial separation of Er^{3+} and Nd^{3+} ions would prevent the possible energy transfer between these lanthanides leading to an increased upconversion luminescence of Er^{3+} and an improved signal to noise ratio.[22,88,89]

5 Appendix

- All citations for the material not published in a peer-reviewed journal (chapters 1, 3, 4.2 and 4.3) can be found in the bibliography.

- Supporting Information for the unpublished material. Other supporting information can be downloaded from the Journal homepages free of charge.

Bibliography

[1] C. Liu, Z. Gao, J. Zeng, Y. Hou, F. Fang, Y. Li, R. Qiao, and L. Shen, "Magnetic / Upconversion Fluorescent Dual-Modal Molecular Probes for Imaging Tiny Tumors in Vivo," *ACS Nano*, vol. 7, no. 8, pp. 7227–7240, 2013.

[2] Wissenschaftlicher Beirat der Bundesregierung Globale Umweltveränderungen, *Welt im Wandel: Energiewende zur Nachhaltigkeit*. 2003.

[3] BMBF, "Aktionsplan individualisierte Medizin," p. 15, 2013.

[4] X. Liu, R. Deng, Y. Zhang, Y. Wang, H. Chang, L. Huang, and X. Liu, "Probing the nature of upconversion nanocrystals: instrumentation matters," *Chem. Soc. Rev.*, vol. 44, no. 6, pp. 1479–1508, 2015.

[5] D. Yang, P. Ma, Z. Hou, Z. Cheng, C. Li, and J. Lin, "Current advances in lanthanide ion Ln^{3+}-based upconversion nanomaterials for drug delivery.," *Chem. Soc. Rev.*, vol. 44, pp. 1416–1448, 2014.

[6] W. Zheng, P. Huang, D. Tu, E. Ma, H. Zhu, and X. Chen, "Lanthanide-doped upconversion nano-bioprobes: electronic structures, optical properties, and biodetection.," *Chem. Soc. Rev.*, vol. 44, no. 6, pp. 1379–1415, 2014.

[7] H. Dong, L.-D. Sun, and C.-H. Yan, "Energy transfer in lanthanide upconversion studies for extended optical applications," *Chem. Soc. Rev.*, vol. 44, no. 6, pp. 1608–1634, 2015.

[8] M. Liu, Y. Lu, Z. Xie, and G. Chow, "Enhancing near-infrared solar cell response using upconverting transparentceramics," *Sol. Energy Mater. Sol. Cells*, vol. 95, no. 2, pp. 800–803, 2011.

[9] F. Lahoz, C. Pérez-Rodríguez, S. Hernández, I. Martín, V. Lavín, and U. Rodríguez-Mendoza, "Upconversion mechanisms in rare-earth doped glasses to improve the efficiency of silicon solar cells," *Sol. Energy Mater. Sol. Cells*, vol. 95, no. 7, pp. 1671–1677, 2011.

[10] J. de Wild, a. Meijerink, J. K. Rath, W. G. J. H. M. van Sark, and R. E. I. Schropp, "Upconverter solar cells: materials and applications," *Energy Environ. Sci.*, vol. 4, no. 12, p. 4835, 2011.

[11] S. Fischer, *Upconversion of Sub-Band-Gap Photons for Silicon Solar Cells*. Phd thesis, University of Freiburg, 2014.

[12] C. M. Johnson and G. J. Conibeer, "Limiting efficiency of generalized realistic c-Si solar cells coupled to ideal up-converters," *J. Appl. Phys.*, vol. 112, no. 10, p. 103108, 2012.

[13] X. Huang, S. Han, W. Huang, and X. Liu, "Enhancing solar cell efficiency: the search for luminescent materials as spectral converters," *Chem. Soc. Rev.*, vol. 42, no. 1, pp. 173–201, 2013.

[14] W. Lin, "Introduction: Nanoparticles in Medicine," *Chem. Rev.*, vol. 115, no. 19, pp. 10407–10409, 2015.

[15] G. Chen, J. Shen, T. Y. Ohulchanskyy, N. J. Patel, A. Kutikov, Z. Li, and C. E. T. Al, "Nanoparticles with efficient upconversion for high-contrast deep tissue bioimaging," *ACS Nano*, vol. 6, no. 9, pp. 8280–8287, 2012.

[16] B. Hötzer, I. L. Medintz, and N. Hildebrandt, "Fluorescence in nanobiotechnology: Sophisticated fluorophores for novel applications," *Small*, vol. 8, no. 15, pp. 2297–2326, 2012.

[17] Y. Dai, H. Xiao, J. Liu, Q. Yuan, P. Ma, D. Yang, C. Li, Z. Cheng, Z. Hou, P. Yang, and J. Lin, "In vivo multimodality imaging and cancer therapy by near-infrared light-triggered trans -platinum pro-drug-conjugated upconverison nanoparticles," *J. Am. Chem. Soc.*, vol. 135, no. 50, pp. 18920–18929, 2013.

[18] J. Yao, M. Yang, and Y. Duan, "Chemistry, biology, and medicine of fluorescent nanomaterials and related systems: New insights into biosensing, bioimaging, genomics, diagnostics, and therapy," *Chem. Rev.*, vol. 114, no. 12, pp. 6130–6178, 2014.

[19] L. Prodi, E. Rampazzo, F. Rastrelli, A. Speghini, and N. Zaccheroni, "Imaging agents based on lanthanide doped nanoparticles," *Chem. Soc. Rev.*, vol. 44, pp. 4922–4952, 2015.

[20] M.-K. Tsang, G. Bai, and J. Hao, "Stimuli responsive upconversion luminescence nanomaterials and films for various applications.," *Chem. Soc. Rev.*, vol. 44, pp. 1585–1607, 2015.

[21] Y. Wang, K. Liu, X. Liu, T. Gregorkiewicz, X. Kong, M. C. G. Aalders, W. J. Buma, and H. Zhang, "Critical shell thickness of core/shell upconversion luminescence," *Biomed. Eng. (NY).*, vol. 2, pp. 2083–2088, 2011.

[22] F. Ai, Q. Ju, X. Zhang, X. Chen, F. Wang, and G. Zhu, "A core-shell-shell nanoplatform upconverting near-infrared light at 808 nm for luminescence imaging and photodynamic therapy of cancer," *Sci Rep*, vol. 5, p. 10785, 2015.

[23] Q. Q. Dou, A. Rengaramchandran, S. T. Selvan, R. Paulmurugan, and Y. Zhang, "Core-shell upconversion nanoparticle-semiconductor heterostructures for photodynamic therapy," *Sci. Rep.*, vol. 5, p. 8252, 2015.

[24] H. Dong, S. R. Du, X. Y. Zheng, G. M. Lyu, L. D. Sun, L. D. Li, P. Z. Zhang, C. Zhang, and C. H. Yan, "Lanthanide nanoparticles: From design toward bioimaging and therapy," *Chem. Rev.*, vol. 115, no. 19, pp. 10725–10815, 2015.

[25] N. M. Idris, M. K. G. Jayakumar, A. Bansal, and Y. Zhang, "Upconversion nanoparticles as versatile light nanotransducers for photoactivation applications.," *Chem. Soc. Rev.*, vol. 44, pp. 1449–1478, 2014.

[26] G. Chen, I. Roy, C. Yang, and P. N. Prasad, "Nanochemistry and nanomedicine for nanoparticle-based diagnostics and therapy," *Chem. Rev.*, vol. 116, no. 5, pp. 2826–2885, 2016.

[27] G. Chen, H. Qiu, P. N. Prasad, and X. Chen, "Upconversion nanoparticles: Design, nanochemistry, and applications in Theranostics," *Chem. Rev.*, vol. 114, no. 10, pp. 5161–5214, 2014.

[28] L. Mattsson, K. D. Wegner, N. Hildebrandt, and T. Soukka, "Upconverting nanoparticle to quantum dot FRET for homogeneous double-nano biosensors," *RSC Adv.*, vol. 5, no. 18, pp. 13270–13277, 2015.

[29] N. Bloembergen, "Solid state infrared quantum counters," *Phys. Rev. Let.*, vol. 2, no. 3, pp. 84–85, 1959.

[30] F. Auzel, "Upconversion and anti-Stokes processes with f and d ions in solids," *Chem. Rev.*, vol. 104, no. 1, pp. 139–173, 2004.

[31] E. Chicklis and L. Esterowitz, "Competitive excitation mechanisms for the blue fluorescence in CdF_2:1% Er^{3+}," *Phys. Rev. Let.*, vol. 21, no. 16, pp. 1149–1151, 1968.

[32] M. R. Brown, "Experiments on Er^{3+} in SrF_2. III. Coupled-Ion Effects," *J. Chem. Phys.*, vol. 51, no. 8, pp. 3321–3327, 1969.

[33] L. Esterowitz, A. Schnitzler, J. Noonan, and J. Bahler, "Rare earth infrared quantum counter," *Appl. Opt.*, vol. 7, pp. 2053–2070, 1968.

[34] F. Auzel, "Compteur quantique par transfer d'energie entre deux ions de terres rares dans un tungstate mixte et dans un verre," *Compt. Rend. Acad. Sci.*, vol. 262B, pp. 1016–1019, 1966.

[35] V. U. Ovsyankin, P. P. Feofilov, and Z. Eksperim, "Cooperative sensitization of luminescence in crystals activated with rare earth ions," *Sov. Phys. JETP Lett.*, vol. 4, pp. 317–318, 1966.

[36] J. F. Suyver, a. Aebischer, S. García-Revilla, P. Gerner, and H. U. Güdel, "Anomalous power dependence of sensitized upconversion luminescence," *Phys. Rev. B - Condens. Matter Mater. Phys.*, vol. 71, no. 12, pp. 1–9, 2005.

[37] J. F. Suyver, J. Grimm, K. W. Krämer, and H. U. Güdel, "Highly efficient near-infraredto visible up-conversion process in $NaYF_4$:Er^{3+}, Yb^{3+}," *J. Lumin.*, vol. 114, p. 53, 2005.

[38] J. F. Suyver, J. Grimm, M. K. van Veen, D. Biner, K. W. Krämer, and H. U. Güdel, "Upconversion spectroscopy and properties of $NaYF_4$ doped with Er^{3+}, Tm^{3+} and/or Yb^{3+}," *J. Lumin.*, vol. 117, pp. 1–12, Mar. 2006.

[39] J. Park, K. An, Y. Hwang, J.-G. Park, H.-J. Noh, J.-Y. Kim, J.-H. Park, N.-M. Hwang, and T. Hyeon, "Ultra-large-scale syntheses of monodisperse nanocrystals," *Nat. Mater.*, vol. 3, no. 12, pp. 891–895, 2004.

[40] X. Wang, J. Zhuang, Q. Peng, and Y. Li, "A general strategy for nanocrystal synthesis," *Nature*, vol. 437, no. 7055, pp. 121–124, 2005.

[41] H.-x. Mai, Y.-w. Zhang, R. Si, Z.-g. Yan, L.-d. Sun, L.-p. You, and C.-h. Yan, "High-Quality Sodium Rare-Earth Fluoride Nanocrystals : Controlled Synthesis and Optical Properties," *J. Am. Chem. Soc.*, vol. 128, no. 19, pp. 6426–6436, 2006.

[42] H.-x. Mai, Y.-w. Zhang, L.-d. Sun, and C.-h. Yan, "Highly Efficient Multicolor Up-Conversion Emissions and Their Mechanisms of Monodisperse $NaYF_4$:Yb, Er Core and Core/Shell-Structured Nanocrystals," *Society*, pp. 13721–13729, 2007.

[43] R. Naccache, Q. Yu, and J. A. Capobianco, "The Fluoride host: Nucleation, growth, and upconversion of lanthanide-doped nanoparticles," *Adv. Opt. Mater.*, vol. 3, no. 4, pp. 482–509, 2015.

[44] K. Koempe, H. Borchert, J. Storz, A. Lobo, S. Adam, T. Möller, and M. Haase, "Green-Emitting $CePO_4$:Tb/$LaPO_4$ Core-Shell Nanoparticles with 70 /Ed., vol. 42, no. 44, pp. 5513–5516, 2003.

[45] J. W. Stouwdam and F. C. J. M. van Veggel, "Improvement in the Luminescence Properties and Processability of LaF_3/Ln and $LaPO_4$/Ln Nanoparticles by Surface Modification," *Langmuir*, vol. 20, no. 26, pp. 11763–11771, 2004.

[46] N. J. J. Johnson, A. Korinek, C. Dong, and F. C. J. M. V. Veggel, "Self-focusing by Ostwald Ripening : A Strategy for Layer-by-Layer Epitaxial Growth on Upconverting Nanocrystals," *J. Am. Chem. Soc.*, vol. 134, no. 27, pp. 11068–11071, 2012.

[47] X. Li, D. Shen, J. Yang, C. Yao, R. Che, F. Zhang, and D. Zhao, "Successive layer-by-layer strategy for multi-shell epitaxial growth: Shell thickness and doping position dependence in upconverting optical properties," *Chem. Mater.*, vol. 25, no. 1, pp. 106–112, 2013.

[48] H. Qiu, C. Yang, W. Shao, J. Damasco, X. Wang, H. Å gren, P. Prasad, and G. Chen, "Enhanced Upconversion Luminescence in Yb^{3+}/Tm^{3+}-Codoped Fluoride Active Core/Active Shell/Inert Shell Nanoparticles through Directed Energy Migration," *Nanomaterials*, vol. 4, no. 1, pp. 55–68, 2014.

[49] N. Hildebrandt, K. D. Wegner, and W. R. Algar, "Luminescent terbium complexes: Superior Förster resonance energy transfer donors for flexible and sensitive multiplexed biosensing," *Coord. Chem. Rev.*, vol. 273-274, pp. 125–138, 2014.

[50] S. Lindén, M. K. Singh, K. D. Wegner, M. Regairaz, F. Dautry, F. Treussart, and N. Hildebrandt, "Terbium-based time-gated Förster resonance energy transfer imaging for evaluating protein-protein interactions on cell membranes.," *Dalt. Trans.*, vol. 44, no. 11, pp. 4994–5003, 2015.

[51] M. Sy, A. Nonat, N. Hildebrandt, and L. J. Charbonnière, "Lanthanide-based luminescence biolabelling.," *Chem. Commun. (Camb).*, vol. 52, no. 29, pp. 5069–5208, 2016.

[52] T. Soukka, K. Kuningas, T. Rantanen, V. Haaslahti, and T. Lövgren, "Photochemical characterization of up-converting inorganic lanthanide phosphors as potential labels," *J. Fluoresc.*, vol. 15, no. 4, pp. 513–528, 2005.

[53] A. Aebischer, M. Hostettler, J. Hauser, K. Krämer, T. Weber, H. U. Güdel, and H. B. Bürgi, "Structural and spectroscopic characterization of active sites in a family of light-emitting sodium lanthanide tetrafluorides," *Angew. Chemie - Int. Ed.*, vol. 45, no. 17, pp. 2802–2806, 2006.

[54] F. Wang, Y. Han, C. S. Lim, Y. Lu, J. Wang, J. Xu, H. Chen, C. Zhang, M. Hong, and X. Liu, "Simultaneous phase and size control of upconversion nanocrystals through lanthanide doping.," *Nature*, vol. 463, no. 7284, pp. 1061–1065, 2010.

[55] Q. Dou and Y. Zhang, "Tuning of the structure and emission spectra of upconversion nanocrystals by alkali ion doping," *Langmuir*, vol. 27, no. 21, pp. 13236–13241, 2011.

[56] W. Yu, W. Xu, H. Song, and S. Zhang, "Temperature-dependent upconversion luminescence and dynamics of NaYF4:Yb^{3+}/Er^{3+} nanocrystals: influence of particle size and crystalline phase.," *Dalt. Trans.*, vol. 43, no. 16, pp. 6139–6147, 2014.

[57] F. Shi and Y. Zhao, "Sub-10 nm and monodisperse β-$NaYF_4$:Yb,Tm,Gd nanocrystals with intense ultraviolet upconversion luminescence," *J. Mater. Chem. C*, vol. 2, no. 12, pp. 2198–2203, 2014.

[58] F. van De Rijke, H. Zijlmans, S. Li, T. Vail, A. K. Raap, R. S. Niedbala, and H. J. Tanke, "Up-converting phosphor reporters for nucleic acid microarrays.," *Nat. Biotechnol.*, vol. 19, no. 3, pp. 273–276, 2001.

[59] J. A. Capobianco, F. Vetrone, J. C. Boyer, A. Speghini, and M. Bettinelli, "Enhancement of Red Emission ($^4F_{9/2} \rightarrow {}^4I_{15/2}$) via Upconversion in Bulk and Nanocrystalline Cubic Y_2O_3:Er^{3+}," *J. Phys. Chem. B*, vol. 106, no. 3, pp. 1181–1187, 2002.

[60] S. Heer, O. Lehmann, M. Haase, and H. U. Güdel, "Blue, green, and red upconversion emission from lanthanide-doped $LuPO_4$ and $YbPO_4$ nanocrystals in a transparent colloidal solution," *Angew. Chemie - Int. Ed.*, vol. 42, no. 27, pp. 3179–3182, 2003.

[61] S. Heer, K. Kömpe, H. U. Güdel, and M. Haase, "Highly efficient multicolour upconversion emission in transparent colloids of lanthanide-doped $NaYF_4$ nanocrystals," *Adv. Mater.*, vol. 16, no. 23-24, pp. 2102–2105, 2004.

[62] L. Tu, X. Liu, F. Wu, and H. Zhang, "Excitation energy migration dynamics in upconversion nanomaterials," *Chem. Soc. Rev.*, vol. 44, pp. 1331–1345, 2015.

[63] B. Voss and M. Haase, "Intrinsic Focusing of the Particle Size Distribution in Colloids Containing Nanocrystals of Two Different Crystal Phases," *ACS Nano*, no. 12, pp. 11242–11254, 2013.

[64] R. Thoma, H. Insley, and G. Hebert, "The sodium fluoride-lanthanide trifluoride systems," *Inorg. Chem.*, vol. 1005, pp. 1222–1229, 1966.

[65] J. Wang, H. Song, W. Xu, B. Dong, S. Xu, B. Chen, W. Yu, and S. Zhang, "Phase transition, size control and color tuning of $NaREF_4$:Yb^{3+}, Er^{3+} (RE = Y, Lu) nanocrystals.," *Nanoscale*, vol. 5, no. 8, pp. 3412–20, 2013.

[66] E. Harju, I. Hyppänen, J. Hölsä, J. Kankare, M. Lahtinen, M. Lastusaari, L. Pihlgren, and T. Soukka, "Polymorphism of $NaYF_4$:Yb^{3+},Er^{3+} Up-Conversion Luminescence Materials," *Z. Krist. Proc.*, vol. 1, pp. 381–387, 2011.

[67] C. Renero-Lecuna, R. Martín-Rodríguez, R. Valiente, J. González, F. Rodríguez, K. W. Krämer, and H. U. Güdel, "Origin of the high upconversion green luminescence efficiency in β-NaYF4:2/no. 15, pp. 3442–3448, 2011.

[68] J. H. Burns, "Crystal structure of hexagonal sodium neodymium fluoride and related compounds," *Inorg. Chem.*, vol. 4, no. 6, pp. 881–886, 1965.

[69] D. Tu, Y. Liu, H. Zhu, R. Li, L. Liu, and X. Chen, "Breakdown of crystallographic site symmetry in lanthanide-doped $NaYF_4$ crystals," *Angew. Chemie - Int. Ed.*, vol. 52, no. 4, pp. 1128–1133, 2013.

[70] K. W. Krämer, D. Biner, G. Frei, H. U. Güdel, M. P. Hehlen, and S. R. Lüthi, "Hexagonal Sodium Yttrium Fluoride Based Green and Blue Emitting Upconversion Phosphors," *Chem. Mater.*, vol. 16, no. 7, pp. 1244–1251, 2004.

[71] B. M. Walsh, "Judd-Ofelt theory: principles and practices," *Adv. Spectrosc. Lasers Sens.*, pp. 403–433, 2006.

[72] S. V. Eliseeva and J.-C. G. Bünzli, "Lanthanide luminescence for functional materials and bio-sciences.," *Chem. Soc. Rev.*, vol. 39, no. 1, pp. 189–227, 2010.

[73] G. Liu, "Advances in the theoretical understanding of photon upconversion in rare-earth activated nanophosphors," *Chem. Soc. Rev.*, vol. 44, pp. 1635–1652, 2014.

[74] G. S. Ofelt, "Intensities of crystal spectra of rare-earth ions," *J. Chem. Phys.*, vol. 37, no. 1962, pp. 511–520, 1962.

[75] G. Liu, R. Hull, J. Parisi, R. M. Osgood, H. Warlimont, and B. Jacquier, *Spectroscopic Properties of Rare Earths in Optical Materials*, vol. 83. Springer Berlin / Heidelberg, 2005.

[76] F. Auzel, "Multiphonon-assisted anti-Stokes and Stokes fluorescence of triply ionized rare-earth ions," *Phys. Rev. B*, vol. 13, no. 7, pp. 2809–2817, 1976.

[77] X. Zhou and P. a. Tanner, "Electronic Spectra and Crystal Field Analysis of Er^{3+} in Cs_2 $NaErF_6$," *Society*, no. November, pp. 683–687, 2007.

[78] J. Wang, R. Deng, M. a. MacDonald, B. Chen, J. Yuan, F. Wang, D. Chi, T. S. A. Hor, P. Zhang, G. Liu, Y. Han, and X. Liu, "Enhancing multiphoton upconversion through energy clustering at sublattice level," *Nat. Mater.*, vol. 13, no. 2, pp. 157–162, 2014.

[79] E. M. Chan, "Combinatorial approaches for developing upconverting nanomaterials: high-throughput screening, modeling, and applications," *Chem. Soc. Rev.*, vol. 44, pp. 1653–1679, 2015.

[80] S. Wilhelm, M. Kaiser, C. Würth, J. Heiland, C. Carrillo-Carrion, V. Muhr, O. S. Wolfbeis, W. J. Parak, U. Resch-Genger, and T. Hirsch, "Water dispersible upconverting nanoparticles: effects of surface modification on their luminescence and colloidal stability," *Nanoscale*, vol. 7, no. 4, pp. 1403–1410, 2015.

[81] I. Recalde, N. Estebanez, L. Francés-Soriano, M. Liras, M. González-Béjar, and J. Pérez-Prieto, "Upconversion nanoparticles with a strong acid-resistant capping," *Nanoscale*, vol. 8, pp. 7588–7594, 2016.

[82] C. Schmidtke, H. Lange, H. Tran, J. Ostermann, H. Kloust, N. G. Bastús, J. P. Merkl, C. Thomsen, and H. Weller, "Radical initiated reactions on biocompatible CdSe-based quantum dots: Ligand cross-linking, crystal annealing, and fluorescence enhancement," *J. Phys. Chem. C*, vol. 117, no. 16, pp. 8570–8578, 2013.

[83] C. Schmidtke, E. Pöselt, J. Ostermann, A. Pietsch, H. Kloust, H. Tran, T. Schotten, N. G. Bastús, R. Eggers, and H. Weller, "Amphiphilic, cross-linkable diblock copolymers for multifunctionalized nanoparticles as biological probes," *Nanoscale*, vol. 5, no. 16, pp. 7433–7444, 2013.

[84] F. Wang, T. Sun, R. Ma, X. Qiao, and X. Fan, "Shielding Upconversion by Surface Coating: A Study of Emission Enhancement Factor.," *ChemPhysChem*, vol. 17, pp. 766–770, 2015.

[85] Y. Wang, R. Deng, X. Xie, L. Huang, and X. Liu, "Nonlinear spectral and lifetime management in upconversion nanoparticles by controlling energy distribution," *Nanoscale*, pp. 6666–6673, 2016.

[86] B. Liu, C. Li, D. Yang, Z. Hou, P. Ma, Z. Cheng, H. Lian, S. Huang, and J. Lin, "Upconversion-Luminescent Core/Mesoporous-Silica-Shell-Structured β-$NaYF_4$:Yb^{3+},Er^{3+}@SiO_2@mSiO_2 Composite Na," *Eur. J. Inorg. Chem.*, vol. 2014, no. 11, pp. 1906–1913, 2014.

[87] S. Han, R. Deng, X. Xie, and X. Liu, "Enhancing Luminescence in Lanthanide-Doped Upconversion Nanoparticles," *Angew. Chemie - Int. Ed.*, vol. 53, no. 44, pp. 11702–11715, 2014.

[88] J. Shen, G. Chen, A. M. Vu, W. Fan, O. S. Bilsel, C. C. Chang, and G. Han, "Engineering the upconversion nanoparticle excitation wavelength: Cascade sensitization of tri-doped upconversion colloidal nanoparticles at 800 nm," *Adv. Opt. Mater.*, vol. 1, no. 9, pp. 644–650, 2013.

[89] B. Liu, Y. Chen, C. Li, F. He, Z. Hou, S. Huang, H. Zhu, X. Chen, and J. Lin, "Poly(Acrylic Acid) Modification of Nd^{3+}-Sensitized Upconversion Nanophosphors for Highly Efficient UCL Imaging and pH-Responsive Drug Delivery," *Adv. Funct. Mater.*, vol. 25, no. 29, pp. 4717–4729, 2015.

6 Supporting Information

6.1 Analysing the effect of the crystal structure on upconversion luminescence in Yb^{3+}, Er^{3+}-co-doped $NaYF_4$ nanomaterials

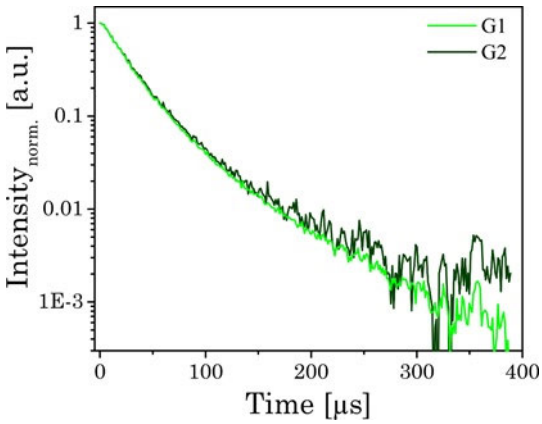

SI Fig. 1: Normalized upconversion luminescence decay kinetics of the Er^3+ emission bands G1 and G2 of $UCNP_{AS}$.

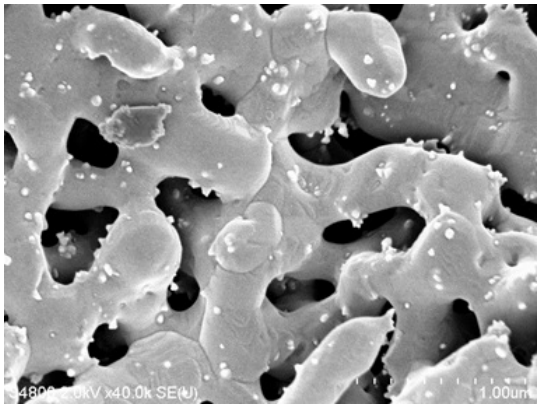

SI Fig. 2: SEM-image of annealed $UCNP_{400}$ with micro domains, which is representative for all $UCNP_x$ with x > 400°C.

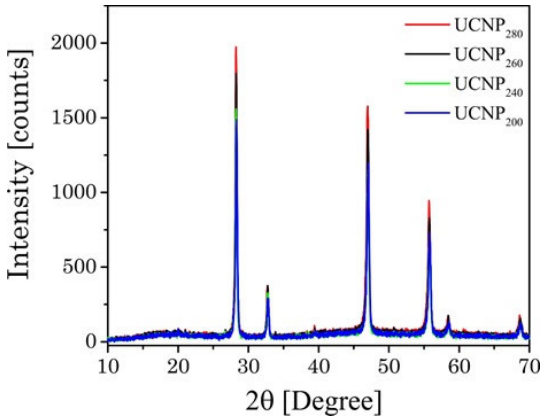

SI Fig. 3: X-ray diffraction patterns of $UCNP_x$ after annealing between 200°C < T_{an} < 280°C for 5h.

SI Tab. 1: Crystallite size of $UCNP_x$ nanoparticles after different thermal treatment calculated with Debye-Scherrer from typical $\alpha-$phase XRD pattern.

$UCNP_x$	Miller Index			
	111	200	220	311
T_{an}[°C]	Crystallite size[nm]			
200	36.8	38.2	27.7	26.2
220	38.7	39.7	28.9	26.1
240	38.9	43.1	29.0	26.3
280	39.6	39.9	28.6	25.8
300	39.6	39.6	29.2	25.5
700	47.7	48.6	34.1	25.2

SI Tab. 2: Crystallite size of $UCNP_x$ nanoparticles after different thermal treatment calculated with Debye-Scherrer from typical $\beta-$phase XRD pattern.

$UCNP_x$	Miller Index				
	100	110	101	201	300
T_{an}[°C]	Crystallite size[nm]				
400	64.4	59.8	58.2	46.4	41.3
500	95.1	75.4	73.6	58.1	53.4
600	105.3	78.7	69.6	53.6	53.0

6.2 Upconversion Luminescence Properties of $NaYF_4$:Yb:Er Nanoparticles Co-doped with Gd^{3+}

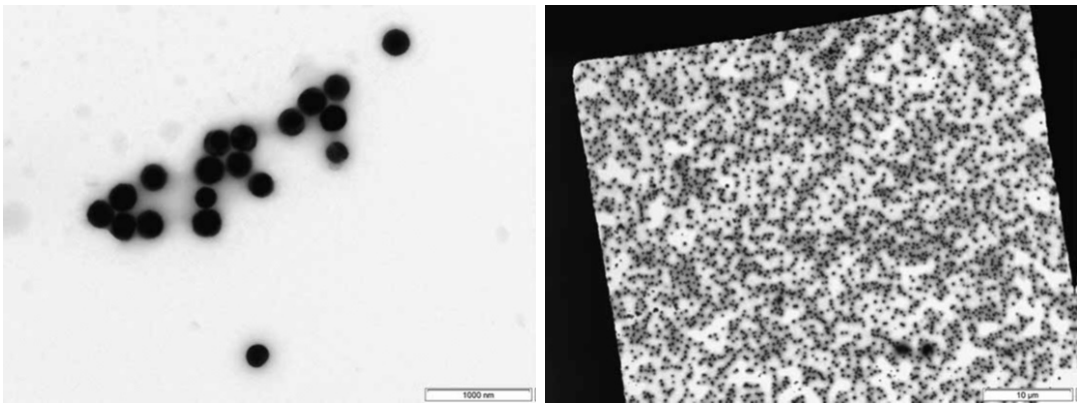

(a) (b)

SI Fig. 1: a) TEM-image of $NaYF_4$:Yb/Er (18/2 mol%) without any Gd^{3+} ions. b) Overview TEM-image of $NaYF_4$:Yb/Er (18/2 mol%) without any Gd^{3+} ions.

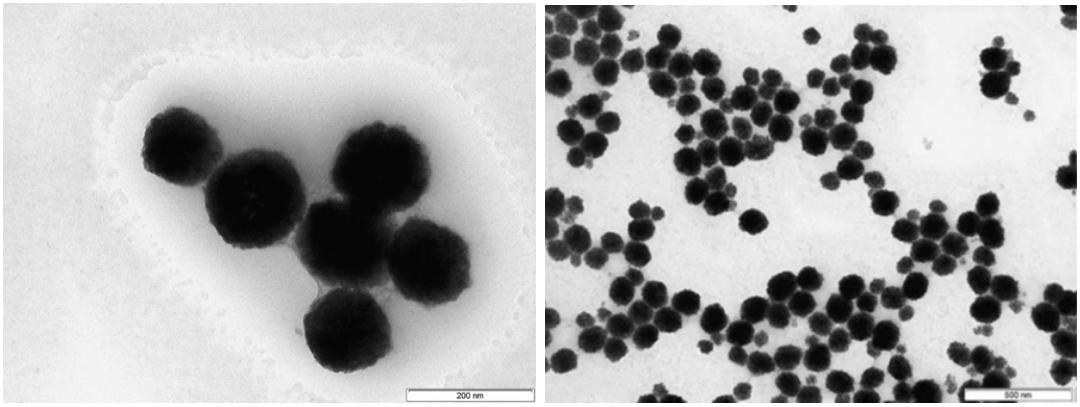

(a) (b)

SI Fig. 2: a) TEM-image of $NaYF_4$: Yb/Er (18/2 mol %) with a Gd^{3+} dopand concentration of 15 mol%. b) TEM-image of $NaYF_4$:Yb/Er (18/2 mol%) with a Gd^{3+} dopand concentration of 30 mol%.

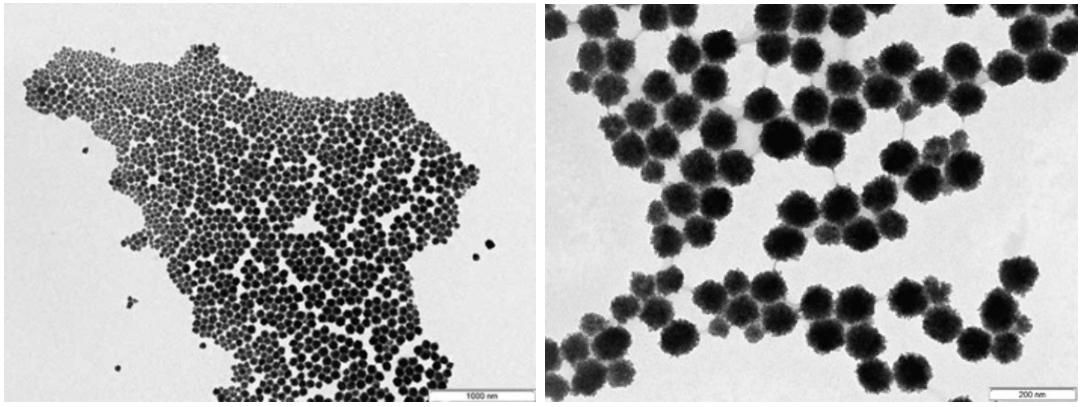

(a) (b)

SI Fig. 3: a) TEM-image of $NaYF_4$: Yb/Er (18/2 mol %) with a Gd^{3+} dopand concentration of 45 mol%. b) TEM-image of $NaYF_4$:Yb/Er (18/2 mol %) with a Gd^{3+} dopand concentration of 45 mol%.

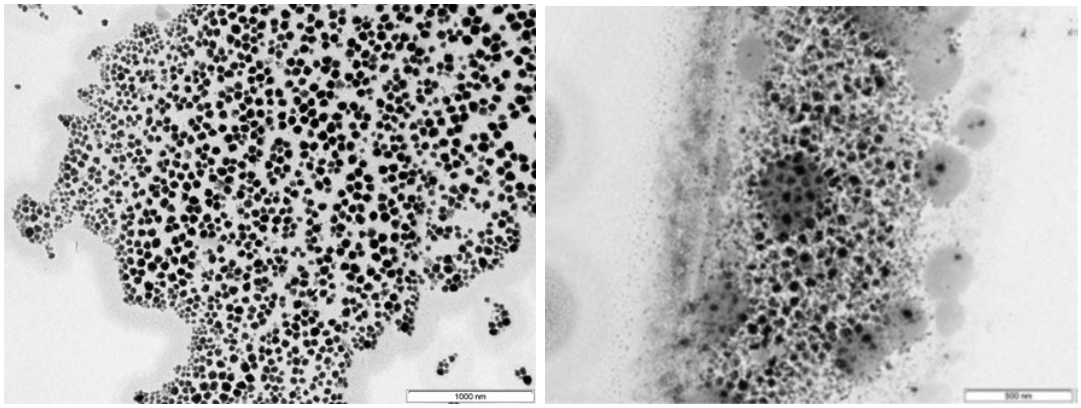

(a) (b)

SI Fig. 4: a) TEM-image of $NaYF_4$: Yb/Er (18/2 mol %) with a Gd^{3+} dopand concentration of 60 mol%. b) TEM-image of $NaYF_4$:Yb/Er (18/2 mol%) with a Gd^{3+} dopand concentration of 80 mol%.

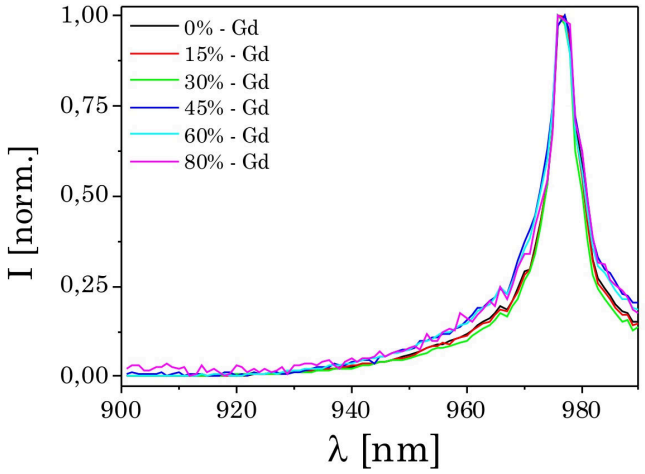

SI Fig. 5: Normalized upconversion (multi photon) excitation spectra (λ_{em}= 545 nm) of different $UCNP_x$ are shown. In all cases the emission maximum is found at an excitation wavelength of λ_{ex} = 976 nm corresponding to the $^2F_{5/2} \rightarrow ^2F_{7/2}$ transition of Yb^{3+} ions.[31,32,36]

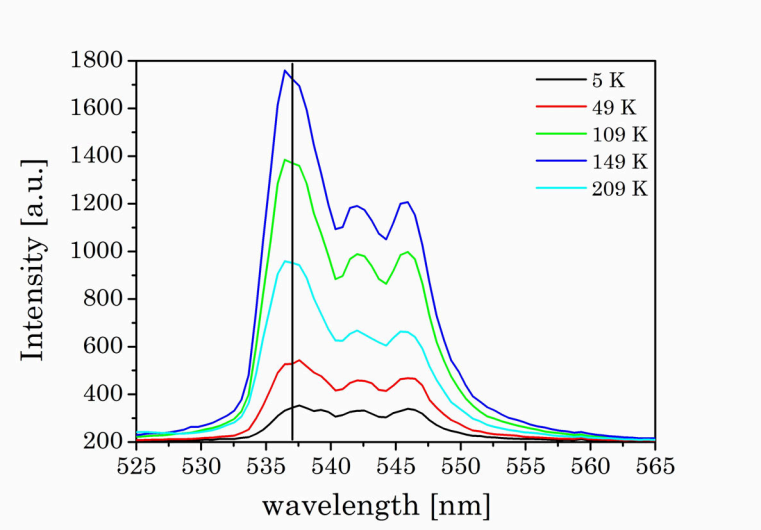

SI Fig. 6: Temperature dependent upconversion emission of $UCNP_x$ nanoparticles (x = 80 mol% Gd^{3+}) of peak G2. It can be seen that the peak position is constant with decreasing temperature, which is in contrast to the results of Silver et al.[13,22]

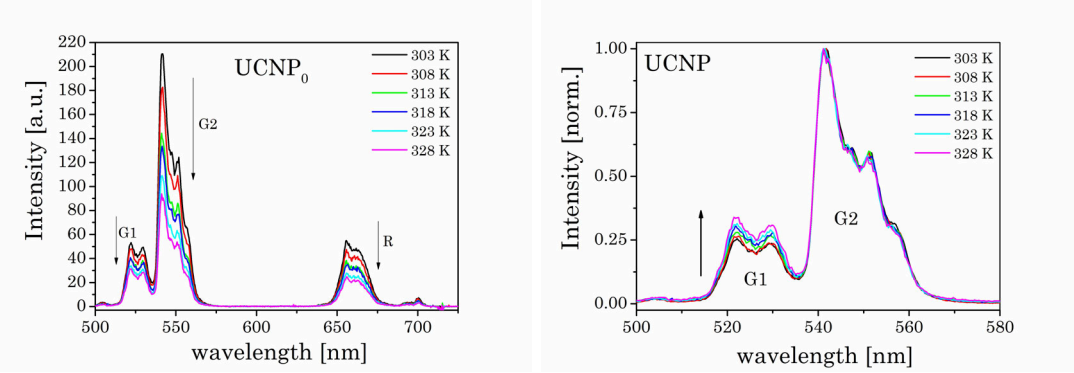

(a) (b)

SI Fig. 7: a) Luminescence spectra of $UCNP_0$ at different temperatures from T = 303 K to 328 K ($\lambda_{ex} = 976$ nm). It was found that the upconversion luminescence of the emitting bands decreased with increasing temperature. b) Normalized upconversion luminescence spectra of $UCNP_0$ at different temperatures.

ICP-OES: The elemental composition of the as-prepared UCNP was determined using ICP-OES (Optima 8300 DV, Perkin Elmer, waltham, united states). 5 mg of the as-prepared UCNP were dissolved 3 mL HNO_3 (65 %, suprapur) and filled up to 5 mL using de-ionized water. The single element standard and the test sample (mixture of single element standards) were prepared with the same acid matrix.

SI Tab. 1: Calculated amount of lanthanides (Yb^{3+}, Er^{3+}, Gd^{3+}) and Y^{3+} of the as-prepared UCNP. Due to the fact that the relative amount of Yb^{3+} and Er^{3+} should be the same for all samples under investigation, the average value are shown with the corresponding standard derivation.

Sample	$UCNP_0$	$UCNP_{15}$	$UCNP_{30}$	$UCNP_{45}$	$UCNP_{60}$	$UCNP_{80}$
avg. Yb^{3+} [mol %]			15.5 ± 3.0			
avg. Er^{3+} [mol %]			1.9 ± 0.2			
Y^{3+}[mol %]	79.9	65.4	50.2	39.0	14.6	0.2
Gd^{3+}[mol %]	0	14.6	29.9	51.3	65.4	82.7

The calculated values of the relative ratio of lanthanides obvious (see SI.Tab.1) show that the expected trend of increasing Gd^{3+} amount by decreasing amount of Y^{3+} could be proved, whereas the ratio of Yb^{3+} and Er^{3+} remains nearly constant. This result underlined that no favored incorporation of the used lanthanides into the crystal lattice existed due to their very similar atomic radius.

6.3 Upconversion $NaYF_4$:Yb:Er nanoparticles co-doped with $Gd^{3+}$and Nd^{3+} for thermometry on the nanoscale

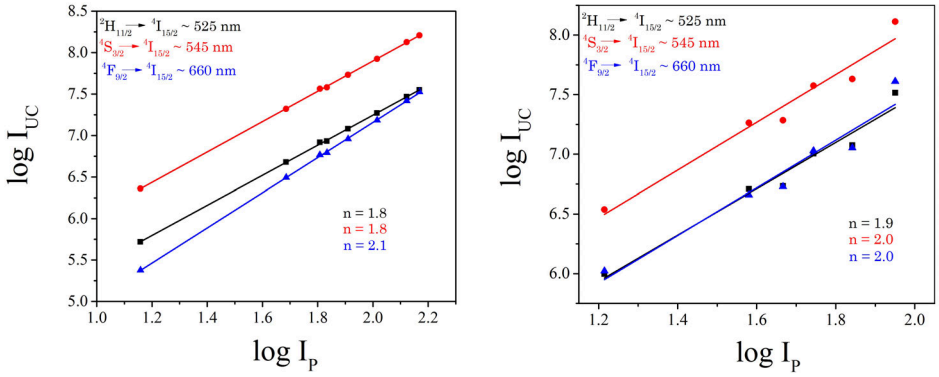

SI Fig. 1: Power dependence (Log I_{UC} – Log I_P plot) of the Er^{3+} transitions G1, G2 and R of oleic acid capped UCNP using different excitation wavelength (left: λ_{ex} = 976 nm; right: λ_{ex} = 795 nm).

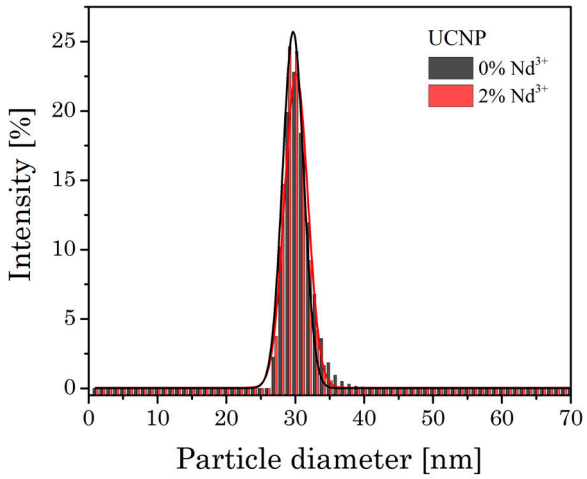

SI Fig. 2: DLS analysis of UCNP and $UCNP_{Nd}$ fitted using a Gaussian function.

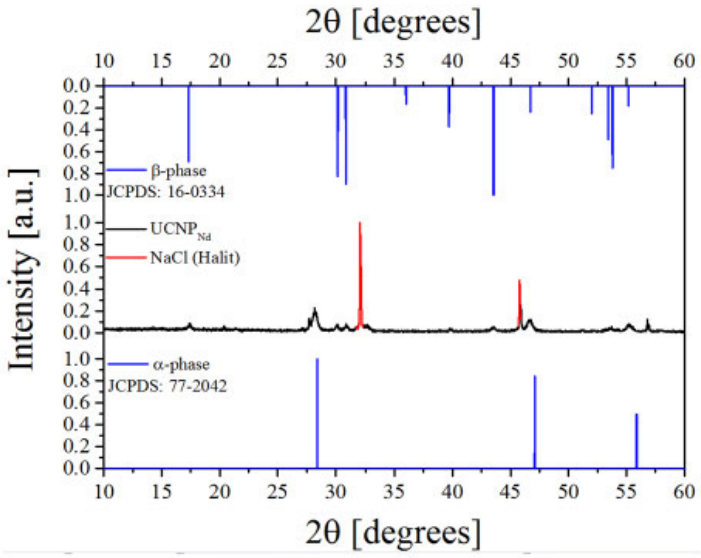

SI Fig. 3: Diffractogram of UCNP$_{Nd}$ with the reference data of $\alpha-NaYF_4$ (JCPDS:77-2042) and $\beta - NaYF_4$ (JCPDS:16-0334) [39].

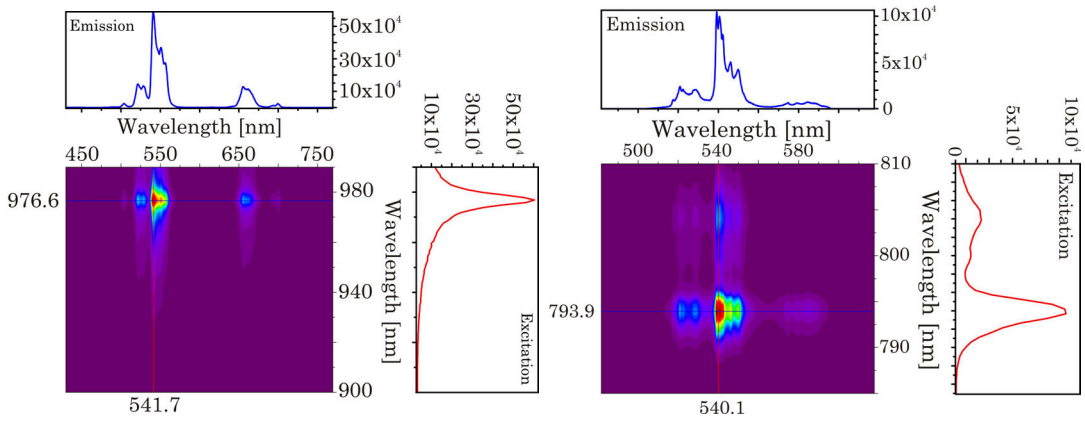

SI Fig. 4: Excitation emission spectra (total luminescence spectra) of UCNP and UCNP$_{Nd}$.

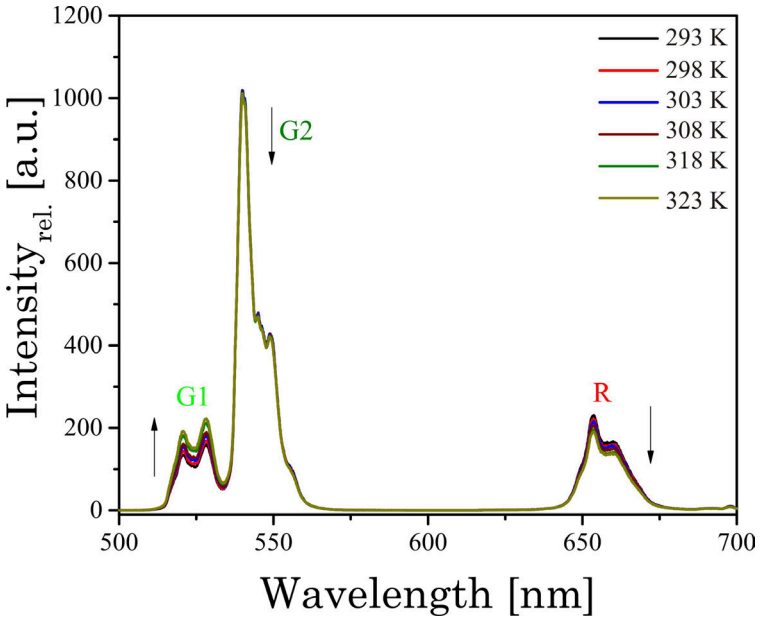

SI Fig. 5: Upconversion emission spectra of UCNP excited at $\lambda_{ex} = 976$ nm at temperatures between 293 K and 323 K are shown.

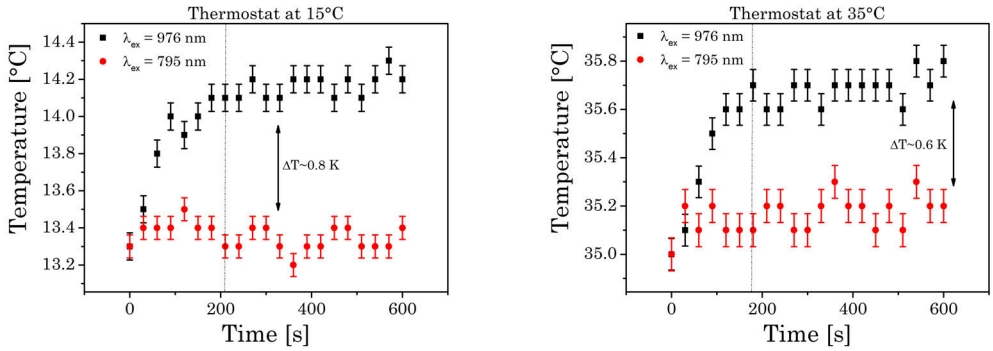

SI Fig. 6: Temperature dependence of UCNP_{Nd} dissolved in water at different irradiation wavelength and thermostat temperature over time

Acknowledgment

First of all, I would like to thank my supervisor Prof. Dr. Michael U. Kumke for giving me the scientific freedom to pursue and to realize my own scientific attempts in the Lab. He enabled me to be part of diversified and challenging scientific projects with extraordinary collaborators, to grow with each task and challenge, and taking on more and more responsibility along the way. I always appreciated his encouragement, support, constructive criticism and giving me the feeling of being a valued scientist.

I want to thank Prof. Dr. Hans-Gerd Löhmannsröben for giving me the great opportunity to work in his group, from being a student scientific assistant to finishing my PhD. Excellent technical equipment, a friendly atmosphere with many colleagues of different scientific background created unique working conditions.

Furthermore, my colleagues from the University of Potsdam, especially my office mates Katlen Brennenstuhl and Uschi Eisold for a familiar lovely atmosphere and for introducing me into the world of coffee. And of course Sean McGee for countless synthesis on surface modified UCNPs, Philipp-A. Primus, Sascha Eidner and Roman Flehr for teaching me in terms of building up laser- and spectroscopic systems and more important how the keep them running. Finally, I want to thank Dr. Karolina Bedorf and Julia Wolter for the personal support and for becoming good friends in my live.

My twin in the physical chemistry group and long-time companion during the studies and special person Sören Draffehn, many things would be different now without him.

My family and friends contributed by keeping my life in balance and helping me unfailingly to focus on the things that really matter.

- thank you!

Declaration

Hiermit versichere ich, dass ich die hier vorgelegte Dissertation selbstständig verfasst und keine anderen als die angegebenen Quellen und Hilfsmittel verwendet habe.

Ich versichere, dass diese Arbeit noch nicht an anderer Stelle zur Erlangung des Doktorgrades eingereicht worden ist.

Berlin, Juni 2016

(Dennis Tobias Klier)